

ORDERED MESOPOROUS OXIDES OF ZINC, INDIUM AND TIN:

SYNTHESIS BY STRUCTURE REPLICATION,
CHARACTERIZATION AND GAS SENSING

Dissertation zur Erlangung des Grades

„Doktor der Naturwissenschaften“

- Dr. rer. nat. -

des Fachbereichs 08
Biologie und Chemie der
Justus-Liebig-Universität Gießen

vorgelegt von

Thomas Waitz

ORDERED MESOPOROUS OXIDES OF ZINC, INDIUM AND TIN:

SYNTHESIS BY STRUCTURE REPLICATION,
CHARACTERIZATION AND GAS SENSING

Dissertation zur Erlangung des Grades

„Doktor der Naturwissenschaften“

- Dr. rer. nat. -

des Fachbereichs 08
Biologie und Chemie der
Justus-Liebig-Universität Gießen

vorgelegt von

Thomas Waitz

Die vorliegende Arbeit entstand in der Zeit von Mai 2005 bis November 2009 am Institut für Anorganische und Analytische Chemie der Justus-Liebig-Universität Gießen in der Arbeitsgruppe von Prof. Dr. Michael Tiemann.

Erstgutachter: Prof. Dr. Michael Tiemann
Zweitgutachter: Prof. Dr. Bernd Smarsly

Für meine Eltern

Content

Versicherung	i
Abkürzungsverzeichnis	ii
 Part I – FUNDAMENTALS	 1
1. Introduction	2
1.1 Introduction to porous materials	2
1.2 Synthesis strategies for ordered mesoporous metal oxides	5
1.2.1 Endotemplating	5
1.2.2 Nanocasting	6
1.2.2.1 Mesoporous silica phases as hard templates	8
1.2.2.2 Mesoporous carbon phases as hard templates	10
1.2.3 Synthesis details using hard templates	12
 2. Aim of this work	 15
 Part II – Experimental	 17
3. Experimental	18
3.1 Synthesis procedures	18
3.2 Characterization Methods	18
3.2.1 Powder X-ray diffraction (P-XRD)	18
3.2.2 Nitrogen physisorption	18
3.2.3 Thermogravimetry coupled with mass spectrometry (TG-MS)	22
3.2.4 Transmission electron microscopy (TEM)	22
3.2.5 Scanning electron microscopy (SEM)	22
3.2.6 Raman measurements	23
3.2.7 Photoluminescence measurements (PL)	23
3.3 Gas sensing	23

Part III – Results and Discussion	29
4. Synthesis and characterization of mesoporous zinc(II) oxide	30
4.1 Zinc oxide	30
4.2 Synthesis and characterization of mesoporous templates	30
4.2.1 Synthesis and characterization of mesoporous SBA-15	30
4.2.2 Synthesis and characterization of mesoporous CMK-3	33
4.3 Impregnation of mesoporous carbon with $\text{Zn}(\text{NO}_3)_2$	35
4.4 Conversion of ZnO precursor and template removal	38
4.5 Synthesis of mesoporous ZnO	40
4.5.1 Characterization of composite materials	40
4.5.2 Characterization of mesoporous ZnO	42
4.6 Gas sensing properties of mesoporous ZnO	48
5. Synthesis and characterization of mesoporous indium(III) oxide	49
5.1 Indium oxide	49
5.2 Synthesis and characterization of mesoporous templates	49
5.2.1 Synthesis and characterization of mesoporous KIT-6	49
5.3 Conversion of In_2O_3 precursor in mesoporous templates	52
5.4 Synthesis and characterization of mesoporous In_2O_3 with silica as template	53
5.4.1 Synthesis of mesoporous In_2O_3	53
5.4.2 Characterization of composite materials	54
5.4.3 Characterization of mesoporous In_2O_3	58
5.4.3.1 Characterization of mesoporous In_2O_3 with SBA-15 as template	58
5.4.3.2 Characterization of mesoporous In_2O_3 with KIT-6 as template	62
5.4.4 Investigations on growth and morphology of In_2O_3 particles in KIT-6	65
5.4.5 Investigations on the morphology of In_2O_3 particles in SBA-15	70
5.4.6 Temperature stability of mesoporous In_2O_3	73
5.5 Synthesis and characterization of mesoporous In_2O_3 with carbon as template	76
5.6 Gas sensing properties of mesoporous In_2O_3	79
5.6.1 Methane sensing properties of mesoporous In_2O_3	79
5.6.2 Ozone sensing properties of mesoporous In_2O_3	83

6. Synthesis and characterization of mesoporous tin(IV) oxide	88
6.1 Tin oxide	88
6.2 Synthesis of mesoporous templates	88
6.3 Conversion of SnO ₂ precursor in mesoporous silica	88
6.4 Synthesis and characterization of mesoporous tin oxide	89
6.4.1 Synthesis of mesoporous SnO ₂	89
6.4.2 Characterization of composite materials	90
6.4.3 Characterization of mesoporous SnO ₂	92
6.4.4 Temperature stability of mesoporous SnO ₂	96
6.5 Gas sensing properties of mesoporous SnO ₂	97
7. Summary	100
8. Outlook	104
9. Zusammenfassung	106
10. Literature	110
Part IV – Appendix	117

Hiermit versichere ich, die vorliegende Arbeit eigenständig und ausschließlich unter Verwendung der angegebenen Hilfsmittel und Quellen durchgeführt zu haben. Die Arbeit wurde zuvor keiner Prüfungsbehörde in gleicher oder ähnlicher Form vorgelegt.

Gießen, den 08.11.2009

Thomas Waitz

Abkürzungsverzeichnis

<i>BET:</i>	Brunauer, Emmet, Teller: method for determination of the specific surface area
<i>BJH:</i>	Barret, Joyner, Halenda: method for determination of the pore size distribution
<i>CB:</i>	conduction band
<i>CMK:</i>	Carbon Mesostructured by Korea Advanced Institute of Science and Technology
<i>EDX:</i>	energy dispersive X-ray spectroscopy
<i>EISA:</i>	evaporation induced self-assembly
<i>FWHM:</i>	full width at half maximum
<i>GB:</i>	grain boundary
<i>HFIP:</i>	hexafluoroisopropanol
<i>ITO:</i>	tin-doped indium oxide
<i>IUPAC:</i>	International Union of Pure and Applied Chemistry
<i>KIT:</i>	Korea Advance Institute of Science and Technology
<i>LED:</i>	light-emitting-diode
<i>MCM:</i>	Mobil Composition of Matter
<i>MS:</i>	mass spectrometry
<i>MWD:</i>	microwave digestion
<i>NLDFT:</i>	Non local density functional theory
<i>P-123:</i>	Pluronic® P123 (PEO ₂₀ PPO ₇₀ PEO ₂₀)
<i>PF:</i>	phenol-formaldehyd-polymers
<i>PL:</i>	photoluminescence
<i>QMB:</i>	quartz-micro-balance
<i>SAED:</i>	selected area electron diffraction
<i>SBA:</i>	Santa Barbara
<i>SDA:</i>	structure-directing agent
<i>SEM:</i>	scanning electron microscopy
<i>TCO:</i>	transparent conductive oxide
<i>TEM:</i>	transmission electron microscopy
<i>TEOS:</i>	tetraethylorthosilicate
<i>TG:</i>	thermogravimetry
<i>THF:</i>	tetrahydrofurane

TLCT: true liquid crystal templating

TSE: tensile strength effect

XRD: X-ray diffraction

Part I – FUNDAMENTALS

1. Introduction

1.1 Introduction to porous materials

According to IUPAC recommendations, porous substances are classified by their pore sizes as micro-, meso-, and macroporous materials.^[1] Microporous materials exhibit pore sizes smaller than 2 nm. Typical representatives of this material class are the various types of crystalline zeolites.^[2] Their structures, consisting of polyhedra, layers or chains, are yielded by corner-linked $[(\text{Al},\text{Si})\text{O}_4]$ -tetrahedra. Zeolites and zeolite-related materials are generally synthesized by a structure directed sol-gel process, where small molecules, *e.g.*, quaternary ammonium salts serve as a ‘template’^a.^[3, 4] Due to their LEWIS acidity, large surface areas (up to $1000 \text{ m}^2\text{-g}^{-1}$), and small pore size distributions, zeolites are frequently used in catalysis, as adsorption material or as molecular sieves for size- and particle-selective isolation of ions and small molecules.

The present thesis concerns mesoporous materials, which consist of pores whose diameters are in the range between 2 and 50 nm. The most well-known representatives of this material class are the extensively investigated M41S-silica materials, prepared first by the Mobil Oil Company in 1992.^[5] These materials are particularly characterized by periodically arranged pore systems, small pore size distributions, large surface areas, as well as a high thermal stability.^[6-9] Figure 1 shows mesostructures of the most well-established representatives of the M41S family, including (a) the MCM-41 silica with a 2-D hexagonal pore arrangement (space group: $p6mm$), (b) the MCM-48 silica with a cubic arrangement of the mesopores (space group: $la3d$) and (c) MCM-50 silica (non-porous), possessing a lamellar structure (space group: $p2$).

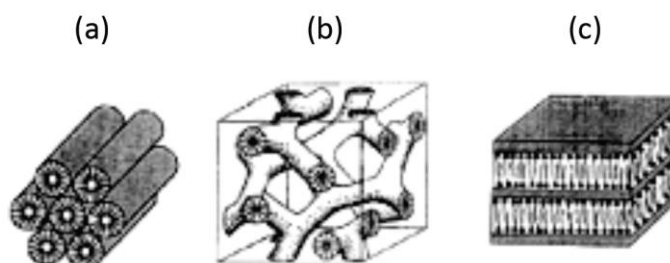


Figure 1. Structures of the mesoporous 2-D hexagonal MCM-41 silica (a); the cubic MCM-48 silica (b) and the lamellar MCM-50 silica (c). Scheme modified according to reference.^[9]

^a In the frame of this thesis, the term ‘template’ and ‘structure directing agent’ (SDA) are utilized synonymously for any species which is applied for a selective manipulation of the products’ structural or morphological features. A more detailed consideration concerning these terms can be found in references [3,4].

The SBA-n and the KIT-n materials represent further families of ordered mesoporous materials with larger pores, which were synthesized for the first time at Santa Barbara University and the Korea Institute of Science and Technology.^[10] In contrast to M41S-silica, the SBA-n and KIT-n phases usually consist of larger mesopores, which are additionally linked by micropores or small mesopores, leading to an interconnected pore system. However, with regard to the mesostructure of the SBA-n and the KIT-n materials, there are structural analogies to the MCM-n materials. SBA-15 silica, the most well-established representative of the SBA family, exhibits a hexagonal pore arrangement identical with MCM-41 with the space group $p6mm$. On the other hand, KIT-6 silica with the space group $la3d$ can be envisaged as the large-pore analogue of MCM-48.

The syntheses of these mesoporous materials are accomplished similar to the zeolite syntheses by a structure-directed sol-gel process in a way like this: to a solution containing amphiphilic molecules as a template, a silica source (precursor), *e.g.* tetraethylorthosilicate (TEOS), is added. During hydrolysis and condensation of the precursor a rigid composite material is formed into which the template is incorporated. After removal of the template by calcination or solvent extraction a rigid mesoporous solid is obtained. In contrast to the structure-directed zeolite synthesis by individual molecules, the MCM-n, SBA-n and KIT-n syntheses are directed by supramolecular aggregates of amphiphilic molecules (micelles) *e.g.* long chain alkyltrialkylammonium halides or (tri)block copolymers which cause the formation of larger pores.

The utilization of amphiphilic molecules as structure-directing agents is often described as 'soft matter-' or 'endotemplating'. Much research activity has been focused on the formation mechanism of ordered endotemplated mesoporous materials, where two different mechanisms are considered to be involved (see *Figure 2*).^[11, 12] In case of the *true liquid crystal templating* (TLCT) mechanism, the concentration of the surfactant is high enough that under the prevailing conditions (temperature, pH value) a lyotropic liquid crystalline phase is formed, serving as structure-directing agent (SDA) even in the absence of a silica source. In case of the *cooperative mechanism* a mesostructure is formed even at lower concentration of the surfactant, when a cooperative self-assembly between surfactant molecules and already added silica precursor leads to the formation of a liquid crystalline phase.^[13]

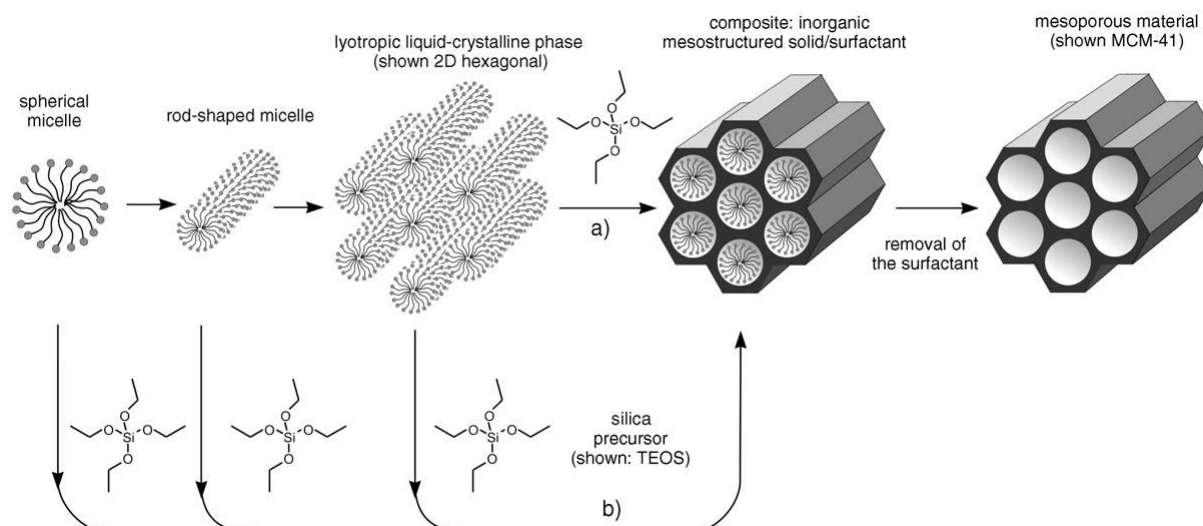


Figure 2. Formation process of the mesoporous materials by the true liquid crystalline template mechanism (a) and the cooperative liquid crystalline template mechanism (b).^[11]

Apart from the synthesis of pure silica materials, the endotemplating concept can be transferred to inorganic/organic hybrid materials (organosilica) as well as purely organic materials. In the former case bissilylated organosilica precursors, like 1,4-bis(triethoxysilyl)benzene (BTEB) lead to the class of the periodic mesoporous organosilicas (PMO) which are promising candidates for hydrogen storage or chromatography.^[11] In case of purely organic materials, ordered mesoporous phenol-formaldehyd polymers (PF) can be synthesized with a soluble low-molecular weight resol-polymer precursor consisting of phenol and formaldehyde ($M_w = 500 - 5000$) which is added to a solution containing amphiphilic molecules. The mesostructure is obtained by a solvent evaporation induced self-assembly (EISA), followed by thermopolymerization of the 'resol' precursor to form a rigid-structure matrix polymer. A stable mesoporous organic material is obtained after calcination or extraction. Such a synthesis facilitates access to a hexagonal FDU-15 (space group: $p6mm$) as well as cubic phases FDU-14 and FDU-16 (space group: $Im\bar{3}d$ and $Im\bar{3}m$).^[14-16]

The third class of porous materials are macroporous substances, containing pores larger than 50 nm. The synthesis of various metal oxides and phosphates is typically accomplished by a template-directed synthesis using rigid structures like ordered arrays of polystyrene latex spheres, with metal alkoxides as precursors.^[17] The latex spheres can be removed either by calcination or extraction with a THF/acetone mixture. Macroporous organic substances, such as polyester ('polyglycolides'), exhibit potential for application as biomaterials, e.g. in surgery

of orthopedics. A promising synthesis approach for this materials is the thermally induced elimination of metal halides from halogenoacetates. Within this solid-state reaction the eliminated metal halide forms a skeleton for the polymerizing organic species. After leaching off the salt with water, a material with non-ordered sponge-like porosity is obtained; vice versa, the polyglycolide can be removed with hexafluoroisopropanol (HFIP) resulting in the respective macroporous salt.^[18-20]

1.2 Synthesis strategies for ordered mesoporous metal oxides

1.2.1 Endotemplating

Despite the large variety of mesoporous siliceous materials which can be fabricated by the endotemplating strategy, only a few ordered mesoporous metal oxides are known to be accessible by a sol-gel process utilizing amphiphilic molecules as structure-directing agents. *Table 1* depicts a short overview of these metal oxides and their corresponding precursor compounds; a review of further mesoporous inorganic materials (*e.g.* metal phosphates) is given in reference^[21]

<i>composition</i>	<i>inorganic precursor</i>	<i>references</i>
TiO ₂	TiCl ₄ , TiO ₂	[22] [23] [24]
SnO ₂	SnCl ₄	[25]
ZrO ₂	ZrCl ₄	[22]
Nb ₂ O ₅	Nb(OEt) ₅	[26]

Table 1. Overview of ordered endotemplated mesoporous metal oxides.

The synthesis of further metal oxides, however, has not been successful, since the removal of the organic template often leads to a structural collapse of the inorganic framework.^[4] Principally, four reasons for this can be identified:^[3, 21, 27] *i)* Some materials cannot be completely condensed under the prevailing conditions, *e.g.* due to low synthesis temperatures; the removal of the template then leads to a structural collapse. *ii)* Some metal oxides are redox-unstable. During removal of the organic species reduction and re-oxidation of the framework takes place, destroying the mesostructure. *iii)* The necessary curvature to form the cylindrical mesoporous channels are best compatible with amorphous wall

structures. While siliceous materials remain amorphous even up to high temperatures, most metal oxides form crystalline phases. The crystallization process involves in general a shift of atoms, which often results in a structural collapse, since soft templates are unable to create rigid, yet crystalline structures. *iv)* Some metal oxides tend to form dense crystalline phases in aqueous solution; during formation of the solid crystalline structure, a phase separation between the inorganic and the organic phase occurs, preventing the formation of an organic/inorganic composite material.

As a result of the current available research, the endotemplating pathway using metal oxide precursors is not universally transferable to most metal oxides. Moreover, the obtained metal oxides often consist of amorphous phases which possess only poor thermal and mechanical stability that might restrict the range of potential applications, *e.g.* in the field of semiconducting technology. Attempts to yield crystalline pore walls by a subsequent tempering procedure often lead to a structural collapse, due to the necessary shift of the atoms within the pore wall. A post-synthetic filling of the pores with carbon or silica which then serves as a rigid skeleton during the subsequent crystallization process, however, has been proved to prevent a collapse of the mesostructure in Nb/Ta oxides, even after removal of the skeleton.^[28] Another promising and simple strategy of manufacturing mesoporous crystalline metal oxides is the recently developed approach of surfactant templating of already preformed metal oxide nanocrystals. Detailed information concerning this concept can be found in references ^[24, 29]. However, the utilization of rigid structure matrices is a promising approach (nanocasting) for the synthesis of a variety of mesoporous metal oxides with different mesostructures, as described in the following.

1.2.2 Nanocasting

As an alternative to surfactant templating, the *nanocasting concept* provides a promising strategy for the preparation of mesostructured materials. A casting process on the macroscopic scale is generally based on a rigid mold made of wax, plaster, metal or other material as a shaping structure. By filling the void of the mold with the material to be cast, or with a corresponding precursor, subsequent optional processing and final removal of the mold, the casting product can be obtained as the negative replica of the mold.

If this procedure is conceptually scaled down to the nanometer scale, the term *nanocasting*, *exotemplating*^[4] or *hard matter templating* is used to describe this process. The nanocasting pathway to create nanostructured materials is accordingly very straightforward and involves three consecutive steps: *i*) synthesis of a porous template; *ii*) impregnation of the pores with a precursor species for the desired product (*e.g.* a metal salt for a metal oxide), and subsequent thermal conversion *in situ*; *iii*) template removal which yields the product as the negative replica of the structure matrix^[21], see *Figure 3*.

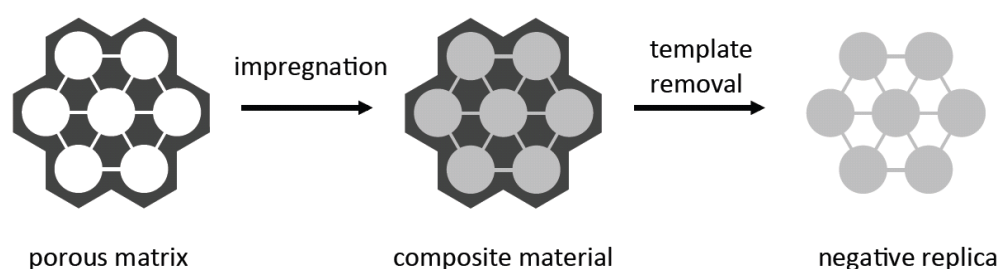


Figure 3. Schematic illustration of the nanocasting concept (exotemplating, hard matter templating). Scheme modified according to reference^[30].

Zeolites, mesoporous silica and phenol-formaldehyd polymers phases (PF) as well as carbon phases are promising candidates for utilization as rigid structure matrices for the nanocasting process. These materials are chemically and thermally stable under appropriate conditions, so that various precursors can be converted into the desired oxides even under harsh conditions, (*e.g.* high synthesis temperatures) without substantial structural loss of the structural integrity of the template. In addition, these templates can afterwards be removed by chemical treatment or thermal combustion. The respective templates generally exhibit a linked pore system, which is a prerequisite for the creation of a stable mesoporous replica structure, as described in detail the following section. Their wall thicknesses are usually in the range between 2 and 10 nm; hence the pores of the respective nanocast structures lie within the same region, as desired. With regard to the pore structure, the materials replicated from such templates generally consist of pores with a slit like geometry, since the original matrices are composed of pores with a cylindrical structure.

1.2.2.1 Mesoporous silica phases as hard templates

As already mentioned above, silica phases are promising candidates for the nanocasting process, serving as rigid structure matrices, as far as they exhibit an interconnected pore system. The absence of bridging pores between the main channels of a hexagonal pore arrangement present in MCM-41 silica for example, would lead to isolated nanowire replicas instead of an interconnected structure after template removal.^[31] In case of an interpenetrating pore system without bridging pores, like in the cubic MCM-48 material a porous replica can be obtained, but the symmetry of this replica is somewhat lower, because the silica removal leads to a gradient displacement of the resultant subframeworks relative to each other.^[32-34]

In this work two types of ordered mesoporous silica systems with interconnected pore systems were employed as hard templates – the 2-D hexagonal SBA-15 and the 3-D cubic KIT-6. Typical features of SBA-15 silica are the hexagonally close packed cylindrical pore channels belonging arranged in the $p6mm$ space group. The pores have uniform sizes from 3 to 10 nm which are additionally interconnected by disordered micropores. The pore wall thicknesses are in the range from 2.5 to 5 nm. Both parameters, the pore size as well as the wall thickness, can be tailored by variation of the synthesis conditions, in particular by the synthesis temperature.^[35] With increasing temperature, the 2-D mesopores become larger whereas the pore wall thickness and the amount of small micropores (< 1 nm) (and ultramicropores) within the pore walls decreases. The latter can be explained by an expansion of the small micropores to larger micro- and mesopores, which leads to an improved interconnectivity.^[35] Figure 4 shows a schematic representation of SBA-15, synthesized at 80 °C (a) and 140 °C (b), respectively.

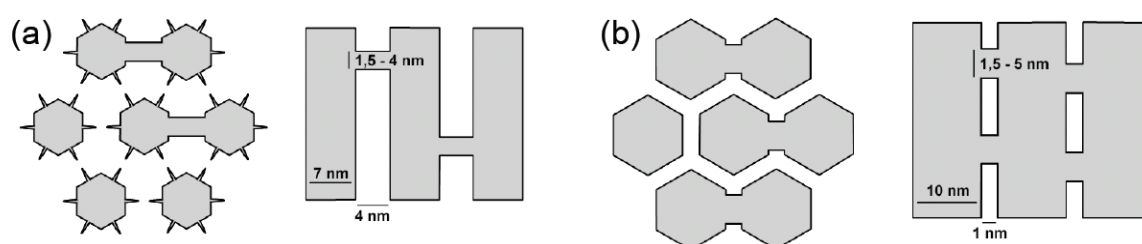


Figure 4. Schematic representation of SBA-15 synthesized at 80 °C showing micropores and poor connections between mesopores (a). A synthesis temperature of 140 °C leads to a better connection between the 2-D channels(b). Scheme modified according to reference^[35].

The KIT-6 material consists of an enantiomeric pair of interpenetrating branched mesoporous channels (space group $la3d$) which are interconnected through smaller micropores, analogues to the SBA-15 material. This unique 3-D channel network provides a highly branched and open pore structure with easy and direct access for guest species, facilitating inclusion or diffusion through the pore channels without pore blockage.^[36] The pore size and the wall thickness are in the range from 3 to 10 nm respectively, and are also adjustable by variation of the synthesis temperature. The utilization of silica matrices is suitable for the synthesis of metal oxides which resist the template removal procedure by chemical treatment with either hydrofluoric acid (HF) or concentrated sodium hydroxide (NaOH) solution.

The first report on the synthesis of mesoporous metal oxides with SBA-15 and cubic SBA-16 silicas as hard templates was made by Zhao et al. in 2003;^[37] several metal oxides including, In_2O_3 , Fe_2O_3 , and Cr_2O_3 , were synthesized by using a solution of the corresponding metal nitrates in ethanol as precursors. After infiltration of the precursor species into the silica pores, subsequent evaporation of the solvent and thermal conversion of the nitrates into the respective oxides at 550 °C, the silica was leached with 2 M NaOH. The resulting metal oxide powders had surface areas between 65 $\text{m}^2\cdot\text{g}^{-1}$ (Cr_2O_3) and 137 $\text{m}^2\cdot\text{g}^{-1}$ (Fe_2O_3), well ordered porosity confirmed by electron microscopy, and a high degree of crystallinity. *Table 2* gives some further examples of successfully synthesized metal oxides with silica as hard template.

<i>structure matrix</i>	<i>replica</i>
SBA-15	CeO_2 ^[37-39] , Co_3O_4 ^[37, 40-43] , Cr_2O_3 ^[37, 43, 44] ,
	Fe_2O_3 ^[37] , In_2O_3 ^[37] , MnO_2 ^[45] , NiO ^[37] , WO_3 ^[44] , SnO_2 ^[46] , ZrO_2 ^[47]
KIT-6	CeO_2 ^[38, 39, 48] , Co_3O_4 ^[40, 42, 43, 49] , Cr_2O_3 ^[43] ,
	Fe_2O_3 ^[50] , In_2O_3 ^[51, 52] , RuO_2 ^[53] , WO_3 ^[35, 49] , SnO_2 ^[46]

Table 2. Overview of ordered mesoporous metal oxides with mesoporous silica as hard template.

Apart from mesoporous metal oxides in form of powders, Smått et al.^[54] reported on the synthesis of monolithic Co_3O_4 , SnO_2 , and MnO_2 with multimodal porosity using silica monoliths as structure matrices with disordered macro- and mesopores. In 2008, the same

group referred to the synthesis of nanocrystalline SnO_2 , ZrO_2 , Mn_2O_3 , and Fe_2O_3 , composed of micrometer-sized spheres with additional internal mesopores and/or macropores, prepared by nanocasting using mesoporous silica spheres as templates.^[55] The metal oxide sphere diameter can easily be adjusted by changing the particle diameter of the starting silica spheres. Furthermore, by variation of the degree of metal salt loading of the spheres, it was also possible to prepare hollow spheres with a porous surface.

Beyond oxidic materials, various mesoporous metal sulfides, CdS ^[56, 57], In_2S_3 ^[56], MoS_2 ^[58], WS_2 ^[58], ZnS ^[56], SiC ^[59, 60] and some metals such as Ag ^[61], Au ^[61], Pd ^[62] and Pt ^[61, 63] have been manufactured by the nanocasting strategy using mesoporous silica as hard templates. A recent review, concerning further nanocast mesoporous materials can be found in reference^[3].

1.2.2.2 Mesoporous carbon phases as hard templates

Originating from the fact, that nanocasting with mesoporous silica as structure matrix is limited to NaOH and HF stable materials, this synthesis strategy can be extended to other metal oxides by using mesoporous carbon materials as hard templates. Mesoporous carbon matrices are generally stable under the prevailing synthesis conditions for metal oxides, *e.g.* thermal decomposition of metal nitrates or acetates; furthermore, they can be removed by combustion.

The fabrication of ordered mesoporous carbon materials (OMC) was realized for the first time in 1999 by two different groups, Ryoo et al.^[64], and Kim et al.^[65] In a typical synthesis procedure, the pores of a rigid silica matrix are infiltrated with a carbon precursor like sucrose or furfuryl alcohol. The precursor is then carbonized at high temperatures in vacuum or inert gas atmosphere to obtain carbon within the pores of the silica matrix. In the last synthesis step, the silica is leached off with HF or NaOH to obtain an OMC matrix. Taking into account that the fabrication procedure utilizes a rigid silica matrix, the synthesis strategy of OMCs is another example of a nanocast process. The great variety of silica phases which are suitable for the nanocasting method permitted the access of a large number of carbon phases, whereas the CMK-n phases (*Carbon Mesoporous by Korea Advanced Institute of Science and Technology*) are the most prominent, including the carbon replica of the MCM-48, SBA-15 and KIT-6 silica, denoted as CMK-1^[64], CMK-3^[66] and CMK-8^[67]. In case of solely coating the

pore walls of SBA-15 and KIT-6 with a carbon layer instead of a complete pore filling, ordered networks of hollow carbon tubes are obtained, designated as CMK-5^[68-70] and CMK-9^[71]. For further details concerning ordered mesoporous carbon materials a recent review from Lee et al. can be recommended.^[72] The first report on utilizing mesoporous carbon as a structure matrix for the synthesis of mesoporous metal oxides was published in 2002 simultaneously by two independent groups. Schüth et al.^[73] as well as Kim et al.^[74] utilized SBA-15 silica for the synthesis of mesoporous CMK-3 carbon, which was applied 'one step further' as template for the synthesis of mesoporous silica. The first non-siliceous ordered mesoporous metal oxide was manufactured in 2005 by Roggenbuck and Tiemann^[30, 75], who utilized CMK-3 carbon for the synthesis of mesoporous MgO. The material possesses a high surface area of $306 \text{ m}^2 \cdot \text{g}^{-1}$, a long-range ordered pore system and a high thermal stability up to 800°C . After these publications a variety of new mesoporous metal oxides was synthesized using CMK-n carbon as hard matter including Al_2O_3 ^[76, 77], CeO_2 ^[78, 79], CuO ^[80], SiO_2 ^[73, 74, 81, 82] and ZnO ^[83-85]. A monolithic CoAl_2O_4 spinel with a bimodal macro-/mesoporous pore size distribution and a surface area of $60 \text{ m}^2 \cdot \text{g}^{-1}$ was synthesized by Schüth et al.^[86], using a carbon monolith as a template. The template was manufactured with SBA-15 silica for the generation of mesopores and NaCl as a porogen for the creation of macropores.

For the fabrication of mesoporous metal oxides the choice of the hard template, either carbon or silica, has an influence on the resulting structure. The utilization of silica leads to a metal oxide which is the negative replica of the structure matrix, while carbon leads to an oxide, which is the positive replica of the original silica matrix, see *Figure 5*.

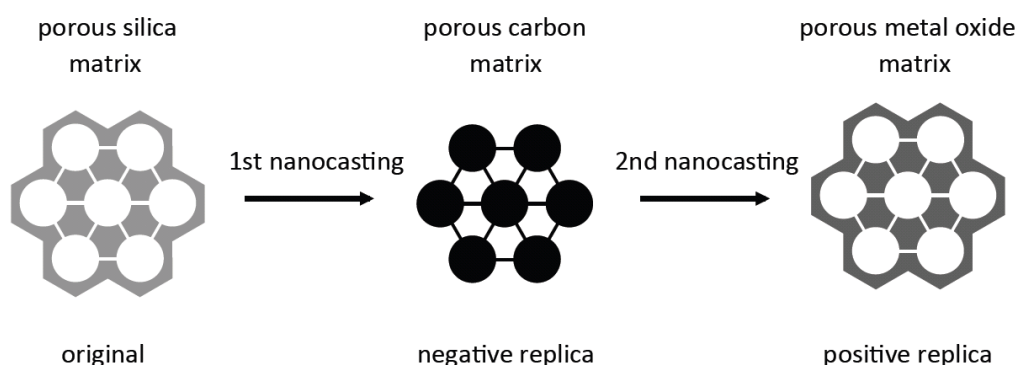


Figure 5. Schematic illustration of the nanocasting concept.
Scheme modified according to reference^[30].

Additionally, in dependence of the used structure matrix, different pore geometries have to be expected. In case of silica as a structure matrix, the resulting metal oxide possesses slit-like pores, whereas carbon as template creates cylindrical pores in the product.

1.2.3 Synthesis details using hard templates

Straightforward as the nanocasting concept may seem to be, research activity has to be focused on apparently small details in the synthesis process which are responsible for the success of the synthesis of mesoporous metal oxides. The optimum realization of these synthesis details is a key factor for the quality of the resulting metal oxide nanostructure; hence they have to be adapted individually for each metal oxide system. Particularly three factors are decisive for the success of the synthesis:

i) Efficient impregnation of the structure matrix: the pore system of the structure matrix must be loaded efficiently with the precursor species to obtain a sufficient cross-linking of the resultant metal oxide inside the pore system. The successful impregnation depends on the consideration of mainly three factors; such as the surface polarity of the structure matrix, the solvent polarity, and the solubility of the precursor in the solvent. For a pore surface with a high density of polar functions, such as free silanol groups in a silica matrix, a polar solvent (ethanol or water) will be suitable in order to obtain a high degree of wettability and convenient diffusion through the pores. Furthermore, the need of polar solvents will be expedient if metal salts are used as the precursors, since these will then have a high solubility. With CMK carbon, which mainly has a non-polar surface, the wettability and the infiltration of precursor with aqueous solutions is more difficult. To enhance the impregnation efficiency the utilization of less polar solvents substantially increases the wettability of the non-polar pore surface of the carbon material. A disadvantage is the low solubility of metal oxide precursor (mostly nitrates or chlorides) in comparison to polar solvents such as water; hence, a compromise between these two aspects must be chosen. Tetrahydrofuran (THF) has turned out to be suitable for this purpose, as the solubility of various metal nitrates is still reasonably high.^[87] Another way to improve the impregnation efficiency of carbon materials is a postsynthetic surface modification with HNO_3 which generates oxygen functionalities such as carbonyl, carboxyl or phenol thus rendering the surface more polar. Due to the harsh conditions which are necessary to create such surface functionalities (a mixture of carbon and

HNO₃ is heated up under microwave irradiation), only carbon materials with thick pore walls (ca. 6 nm) are suitable for the surface modification procedure, since a thin walled carbon structure matrix sustains a structural loss.^[87]

For the infiltration of the precursor two methods are principally available. In case of the *wet impregnation technique* a homogeneous distribution of the metal oxide precursor in the structure matrix is achieved by immersing the matrix in a precursor solution for several hours allowing the precursor species to enter the pores by diffusion. After filtration, drying under mild conditions, and thermal conversion of the precursor into the oxide these cycles are commonly repeated several times, since a volume shrinkage caused by the latter procedures (e.g. evaporation of solvent) does generally not provide a sufficient pore filling. The application of diluted solutions is here mandatory, since a sufficient filtration or centrifugation of excess amounts of precursor is not possible when higher concentrated metal salt solutions are utilized. The high viscosity of these solutions would lead to the deposition of significant amounts of the precursor/metal oxide at the external surface of the mesoporous particles. To avoid the creation of such particles, the *incipient wetness technique* may be more suitable. For impregnation a saturated solution of the metal oxide precursor, which corresponds to the exactly pore volume of the sample, is added and transported into the pores by capillary forces. The advantage using the higher concentrated precursor solution may be fewer impregnation cycles, but a more heterogeneous distribution of precursor in the sample is to be expected.

ii) *Evaluation of suitable conditions for the precursor conversion:* metal nitrates or chlorides are the precursor compounds of choice since they can easily be converted into the desired product by thermal treatment. The conversion temperatures of most precursors are significantly lower than the synthesis temperatures of the silica matrices, e.g. temperature required for calcination. In addition, no reactions of the silica matrix and products/by-products are to be expected which might influence the template function of the matrix. By application of mesoporous carbon however, the conversion conditions of the nitrates must be carefully selected, since the resultant metal oxides catalyze the combustion of the carbon matrix, which might influence the template's function. Pristine CMK-3 carbon, for example, has a combustion temperature of ca. 630 °C. This value is shifted to 220 °C in case of a CuO/CMK-3 composite or 280 °C for a CeO₂/CMK-3 composite.^[79] Both combustion

temperatures are in the range of the nitrate decomposition temperature, so that the evaluation of suitable conversion temperatures is essential.

iii) *Template removal*: the template removal procedure should ensure a complete removal of the structure matrix on the one hand and preserve the structural integrity of the resultant metal oxide matrix on the other. In case of silica, the metal oxide must resist the template removal with either NaOH or HF, while in case of carbon and PF the metal oxide structure needs to withstand the template removal by combustion, *i.e.* high temperatures. As already mentioned, individual synthesis conditions have to be developed, since unfavorable temperatures in case of carbon for example, might damage the metal oxide structure. The main synthesis details are summarized in *Table 3*.

	Silica	Carbon
Efficient impregnation	polar solvents enable a high solubility of metal nitrates and good wettability of the structure matrix	<p>non-polar solvent enables a good wettability of the structure matrix, but the solubility of most metal nitrates is then reduced</p> <p>polar solvent enables a high solubility of nitrates, the wettability is then reduced</p> <p>surface modification with polar functions enhances the wettability for polar solvents – the potential benefit in comparison to the other impregnation strategies must be individually evaluated</p>
Conversion of precursor	evaluation of decomposition temperature to achieve a complete conversion of the precursor into metal oxide	exploration of optimal conversion temperature which ensures the structural integrity of the carbon matrix
Template removal	exploration of leaching time and leaching cycles to achieve a complete template removal	exploration of optimal combustion temperature; avoid unnecessary high temperatures

Table 3. Summary of main aspects of the impregnation procedure.

2. Aim of this work

Among the exhaustively examined mesoporous silica and carbon phases, only very few metal oxide phases with comparable mesostructures existed at the beginning of the present thesis, which possess large specific surface areas, ordered pore systems and a uniform pore size distribution. The development of modern structure replication techniques, however, offered the possibility to prepare well defined crystalline metal oxides with the desired features. Previously the main research activity was predominantly focused on the creation of new mesoporous metal oxides, but no detailed investigations were carried out concerning the formation and growth of the respective materials inside the pores of the structure matrices for example. The relation between the macroscopic particle morphologies of the parental templates and the corresponding replica remained to be elucidated.

With regard to potential applications, mesoporous metal oxides are promising candidates in fields of heterogeneous catalysis^[78, 79], electrode materials^[88] and as gas sensors^[89]. For the latter field, materials with semiconducting properties are required. Within the range of gas sensor technology for example, crystalline nanoscaled systems of non-porous semiconducting metal oxides such as ZnO^[90, 91], In₂O₃^[92-94] and SnO₂^[95] are frequently used as sensitive materials (*chemiresistors*) for the detection of oxidizing and reducing gases. Based on this, aim of the present thesis was the synthesis and characterization of these metal oxides in a mesoporous form, as well as their characterization as sensor materials in cooperation with the working group of Prof. Dr. C.-D. Kohl (Gießen).

The synthesis part was to focus on the application of modern structure replication techniques on the above-mentioned metal oxide systems as well as the already mentioned determination of the morphological relations between template and replica; therefore various rigid structure matrices with different mesostructures (cubic/hexagonal) and varying topologies (pore size/wall thickness) were to be utilized.

At the beginning of this work the synthesis of mesoporous ZnO via the nanocasting route has not been reported yet. For this reason, the synthesis is predominantly subject of these investigations. The fabrication of mesoporous In₂O₃ with silica as hard template has been described previously; investigations concerning the thermal stability, tailoring of parameters like surface area, wall thickness and pore size however, were not reported and are therefore a

further aim of this work. The last part of the thesis concerns the fabrication of mesoporous SnO_2 , which has already been described, but only for a macro-/mesoporous monolithic material. According to the above-mentioned systems, investigations concerning the thermal stability, gas sensing properties as well as morphology were also conducted. To study the materials as well as their formation in the structure matrices, the metal oxides as well as the composite materials were characterized by default with powder X-ray diffraction (P-XRD), nitrogen physisorption, transmission electron microscopy (TEM), scanning electron microscopy (SEM) and thermogravimetry coupled with mass spectrometry (TG-MS).

Part II – Experimental

3. Experimental

3.1 Synthesis procedures

The synthesis procedures are described in 'Part III – Results and Discussion'.

3.2 Characterization Methods

3.2.1 Powder X-ray diffraction (P-XRD)

Powder X-ray diffraction was carried out on a PANalytical X'Pert PRO with an X'Celerator real-time multiple-strip detector using Cu-K α radiation (40 kV, 40 mA). The counting time was 25 seconds in steps of $2\theta = 0.0167^\circ$ for low-angle measurements ($2\theta < 10^\circ$) and 20 seconds in steps of $2\theta = 0.0167^\circ$ for wide-angle measurements ($2\theta > 10^\circ$). Data analysis of P-XRD pattern were conducted with *X-Pert HighScore Plus (2.2.1)* software.

3.2.2 Nitrogen physisorption

Gas adsorption analysis is one of the standard characterization methods for the determination of the specific surface area, pore size distribution as well as pore volume of mesoporous materials. In case of powdery samples nitrogen physisorption measurements are carried out by analyzing the amount of adsorbed nitrogen at a constant temperature (-196 °C) under equilibrium conditions in dependence of the relative pressure, by which the adsorption isotherm of the system is obtained. According to IUPAC, six types of isotherms are classified, as illustrated in *Figure 6*. Type I shows the characteristic isotherm for the adsorption of gases and vapors on microporous solids like activated carbon and zeolite materials. Isotherms of type II can be observed for the gas adsorption on non-porous or macroporous materials. If the interactions among the adsorbate molecules are stronger than the interactions between adsorbate and adsorbent (like in case of nitrogen on ice) type III isotherms are obtained. Mesoporous materials cause a type IV isotherm, distinguished by a steep increase of the amount of adsorbed nitrogen in the relative pressure region of $p/p_0 = 0.6$ to 0.8 , as a result of capillary condensation. Type V isotherms resemble type IV isotherms at middle and high relative pressures.

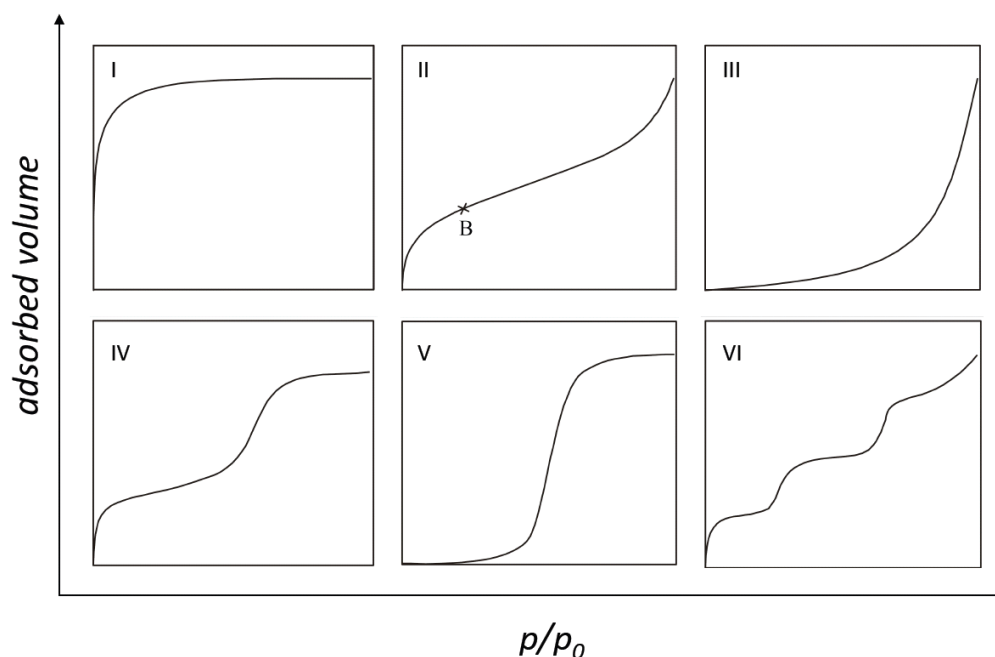


Figure 6. Schematic drawing of characteristic isotherms. Modified according to reference ^[1].

However in the low pressure region, type V isotherms are characterized by weak adsorbate-adsorbent interactions, often observed for the adsorption of water vapor on activated carbon. Type VI isotherms are generated by a stepwise formation of a multilayer on a non-porous surface, whereas primary each adsorbate layer is completely built up, before the formation of the next layer is initiated. More detailed theoretical considerations concerning the isotherm characteristics can be found in some reviews.^[96, 97] In case of type I, II and III isotherms, the adsorption process is reversible, although type I isotherms might cause a hysteresis loop observed for microporous materials in special cases. In contrast, isotherms of type IV and V, which refer to mesoporosity more frequently, possess a hysteresis between adsorption and desorption branch of the isotherm. On the basis of the isotherm's characteristic, conclusions concerning the pore geometry and structure can be obtained. According to IUPAC, four types of hysteresis (H1 to H4) can be distinguished, depicted in *Figure 7*. Type H1 is attributed to mesoporous materials with cylindrical pores and a narrow pore size distribution. Mesoporous materials possessing pores with irregular shape and a broader pore size distribution generate H2 hysteresis. Large slit-like pores and agglomerates of platelike particles are correlated to H3 hysteresis, whereas microporous slit-like pores cause H4 hysteresis.

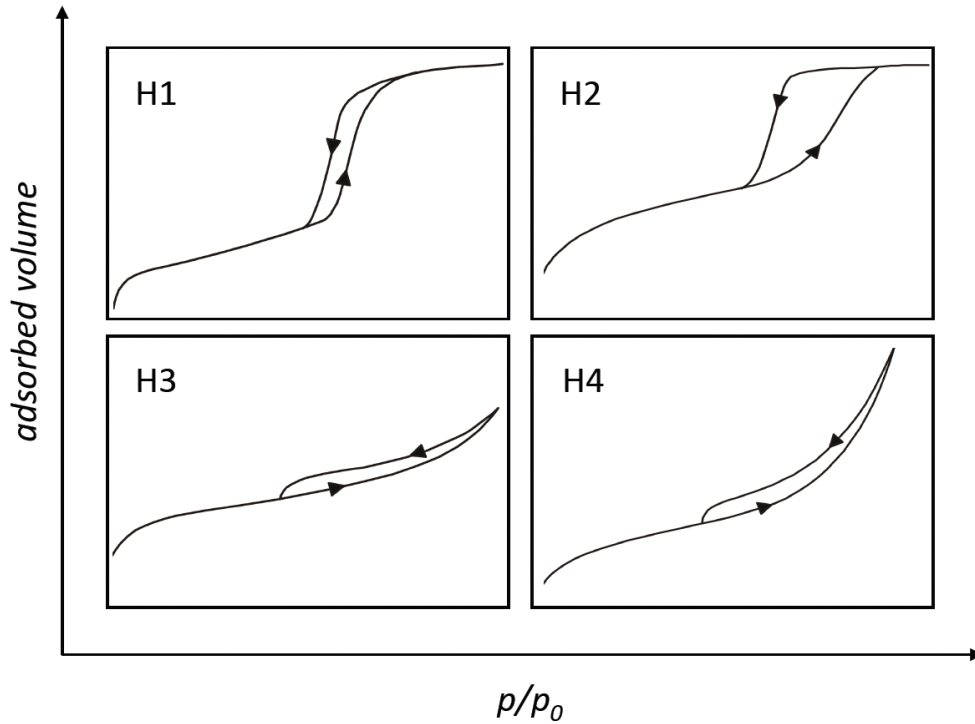


Figure 7. Schematic illustration of characteristic hysteresis loops. Modified according to reference.^[1]

The determination of the specific surface area was conducted according to the theoretical equation (1) of BRUNAUER, EMMET and TELLER (BET)^[98] describing the adsorption of a multilayer on the material's surface in the low pressure region by:

$$\frac{p}{V(p_0 - p)} = \frac{1}{V_m C} + \frac{C - 1}{V_m C} \frac{p}{p_0} \quad (1)$$

p = equilibrium pressure

p_0 = saturation pressure

V = adsorbed gas quantity

V_m = monolayer adsorbed gas quantity

C = BET constant

By plotting $p/V(p_0 - p)$ against p/p_0 with application of N_2 as adsorbate, a straight line is obtained in the pressure region of $p/p_0 = 0.05$ to 0.3 . The specific surface area A_{BET} is determined by the following equation (2):

$$A_{BET} = \frac{V_m \cdot a \cdot N_A}{m} \quad (2)$$

N_A = Avogadro's Number

a = cross-sectional area of an adsorbed N_2 -molecule

m = weight of sample

For the evaluation of the pore size distribution, two methods, NLDFT and BJH, were used. In case of NLDFT (*Non-Local Density Functional Theory*) analysis, the data obtained by experiments of the nitrogen physisorption are compared with simulated isotherms (3).

$$N(p/p_0) = \int_{D_{min}}^{D_{max}} N(p/p_0, D) f(D) dD \quad (3)$$

$N(p/p_0)$ = experimental sorption data

$N(p/p_0, D)$ = simulated sorption data with the pore diameter D

$f(D)$ = pore size distribution

Based on this, the corresponding pore size distribution can be determined by utilizing the following kernels:

- (I) N_2 at 77 K on carbon (slit pore, NLDFT equilibrium model)
- (II) N_2 at 77 K on carbon (cylindrical pore, NLDFT equilibrium model)
- (III) N_2 at 77 K on carbon (slit/cylindrical pore, NLDFT equilibrium model)
- (IV) N_2 at 77 K on silica (cylindrical pore, NLDFT equilibrium model)
- (V) N_2 at 77 K on silica (cylindrical pore, NLDFT adsorption branch)

The application of silica kernels for other oxidic materials is feasible, if kernel (IV) as well as kernel (V) provide nearly the same value for the pore size distribution's maximum. With respect to this work, kernel (IV) was used for all silica phases as well as mesoporous ZnO, In_2O_3 and SnO_2 . If such a consistence was not observed, like in case of carbon/metal oxide composite materials, pore size distribution was calculated by application of BJH (BARRET-JOYNER-HALENDA) method (4) using the data of the desorption branch of the isotherms.^[99]

$$\ln(p/p_0) = -\frac{2\gamma \cdot V_{mol}}{RT} \cdot \frac{1}{r_k} \quad (4)$$

γ = surface tension of the fluid adsorptive at boiling point (N_2 : $8.85 \cdot 10^{-3} \text{ J} \cdot \text{m}^{-2}$)

R = pore size distribution

T = temperature

r_k = Kelvin-radius of the pore

The BJH method is based on the KELVIN equation that describes a correlation between the pore radius and the relative pressure at which the pore condensation occurs. Additionally, it has to be noted that for oxidic materials, BJH analysis tends to underestimate the pore size of about 20 %.^[100, 101]

Nitrogen physisorption measurements were accomplished at -196 °C on a Quantachrome Autosorb 6. The samples were degassed at 120 °C 24 hours prior to measurement. The measuring range was between $p/p_0 = 0.025$ and $p/p_0 = 0.995$ and consisted of 41 points for the adsorption and desorption branch. All calculations were carried out with the Autosorb software 1.51. (June 2005).

3.2.3 Thermogravimetry coupled with mass spectrometry (TG-MS)

Thermal analyses (TG-MS) were carried out under synthetic air flow with a Netzsch STA409PC thermobalance connected to an Aeolos 403C quadrupole mass spectrometer.

3.2.4 Transmission electron microscopy (TEM)

Transmission electron microscopy (TEM) and selected area electron diffraction (SAED) were performed on a Philips CM30-ST microscope; for energy-dispersive X-ray (EDX) analysis an EDAX PV 9900 was used.

3.2.5 Scanning electron microscopy (SEM)

Scanning electron micrographs (SEM) were recorded with a HREM EDX Leo Gemini 982. In case of mesoporous semiconducting metal oxides, the powdery samples were dispersed in deionized water ($10 \text{ mg}\cdot\text{ml}^{-1}$), placed on carbon foil, adhered to the sample holder, and dried. For mesoporous silica materials, the samples were sputtered with platinum for 60 s prior to measurement.

3.2.6 Raman measurements

Raman experiments were performed using a Jobin Yvon microscope system with multichannel detection and 514.5 nm excitation. The measurements were recorded in the spectral range between 250 and 750 cm^{-1} obtained in backscattering geometry with unpolarized detection. The measurements were carried out in collaboration with the working group of Prof. Dr. P. J. Klar (Gießen).

3.2.7 Photoluminescence measurements (PL)

Low-temperature photoluminescence (PL) experiments were conducted at $-268\text{ }^{\circ}\text{C}$ using a HeCd laser (325 nm) as an excitation source and a 1 m Jobin Yvon monochromator with a photomultiplier for detection. The measurements were carried out in collaboration with the working group of Prof. Dr. B. K. Meyer (Gießen).

3.3 Gas sensing

Gas sensors are applied in many fields of industry, automobiles, domestic living and environmental monitoring for analyzing the chemical composition of the ambient atmosphere, *e.g.* to protect from harmful and hazardous gases as well as dangerous solvent vapors. According to the working principle, several kinds of gas sensors can be distinguished, like pellistors, quartz-micro-balances (QMB), optical systems, electrochemical sensors as well as semiconducting gas sensors for example. For further and more exhaustive description of the different sensor types and working principals the following literature is recommended.^[102]

The working principle of semiconducting metal oxide gas sensors, which is one of the most widely used class of gas sensors, is described in more detail in the following:

Semiconducting metal oxides like SnO_2 , ZnO , In_2O_3 , Co_3O_4 and WO_3 reversibly change their surface electronic resistance in the presence of oxidizing as well as reducing gases, which can be processed as an electric signal (see *Figure 8*).

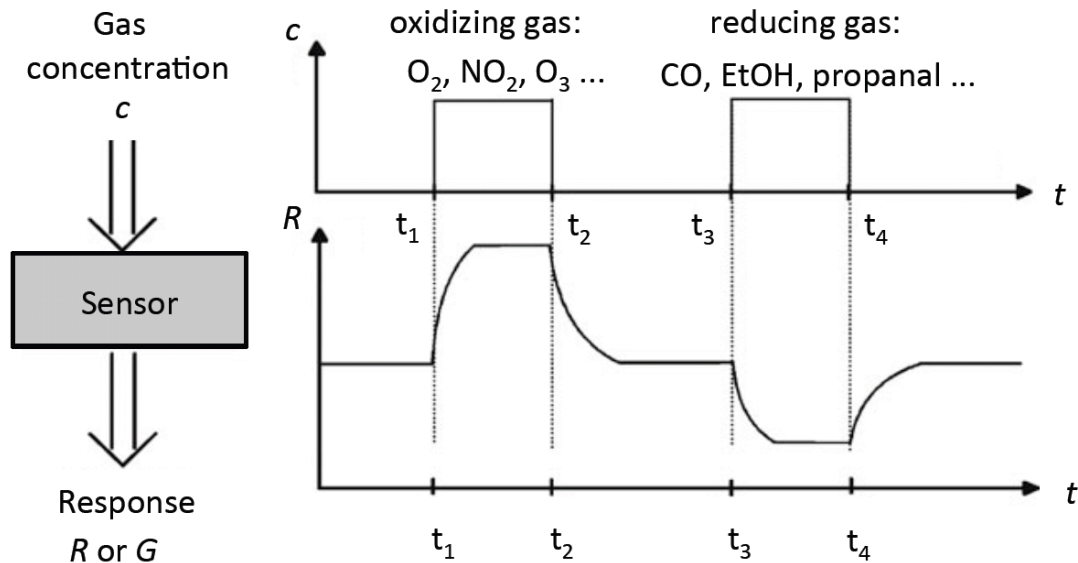


Figure 8. Metal-oxide-based gas sensor: The changes in the gas concentration lead to changes in the conductance G or resistance R of the sensor. Scheme modified according to reference.^[103]

The sensor activity is expressed in terms of either R , G , or S with

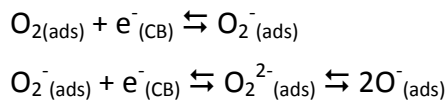
$$\begin{aligned}
 R &= \text{resistance} \\
 G &= \text{conductance } (1/R) \\
 S &= \text{sensitivity with } S = R_{\text{gas}}/R_{\text{air}} \text{ (oxidizing gases)}^b \\
 &\quad \text{and } S = R_{\text{air}}/R_{\text{gas}} \text{ (reducing gases)}
 \end{aligned}$$

Despite the extensive scientific and engineering research the physics and chemistry of semiconducting gas sensors are still not understood in detail. So far it has not been possible to entirely separate several factors concerning the operating principle in order to investigate their individual impact on the overall sensor performance, such as the impact of the surface area, humidity and the porosity.^[89]

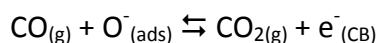
The working principle of a semiconducting metal oxide gas sensor is often described with a standard model. According to this model, the change in the electronic conductance for an n -semiconductor, is based on oxygen vacancies serving as electron donors or excess oxygen atoms acting as electron acceptors in case of p -type semiconductors. The processes of gas detection are not yet clarified in depth. However the mechanism of gas sensing can be explained by the ionosorption model, in the following only detailed described for n -type semiconductors due to the importance for that thesis. Oxygen species, like O_2^- , O_2^{2-} , O^{2-}

^b R_{gas} and R_{air} denote the sensor resistance in the presence and in the absence of the target gas.

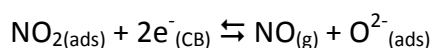
and O^- originated by chemisorption of oxygen from the ambient gas phase, creates extrinsic surface acceptor states, immobilizing conduction band electrons (CB) from the near surface region.



That near surface region is therefore depleted of electrons relative to the interior parts of the metal oxide crystal, which causes a band bending in the respective region creating a double Schottky barrier in adjacent metal oxide crystals (see also *Figure 9*). In this region, called depletion layer, the surface coverage with oxygen functionalities is at equilibrium; the conductance is lower compared to the absence of oxygen. Presence of either oxidizing or reducing gases influences the density of the charge carriers in the near surface region. Reducing gases like CO lead to a decrease of the depletion layer thickness and potential barrier height due to the abstraction of surface-bound oxygen atoms. During this process a release of the previously immobilized electrons in the conduction band occurs, resulting in a decreased electronic resistance.

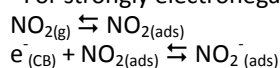


Contrary, oxidizing gases like nitrogen dioxide (NO_2) immobilize further conduction band electrons from the near surface region by creating additional surface acceptor states, resulting in an increase of the depletion layer thickness and an increase of the electronic resistance.^c



Additionally to the above described ionosorption mechanisms, changes in conductivity of a sensing layer is often explained by 'grain boundary models'.^[89] In this context, the term *grain* is used as a synonym for a single crystalline particle, regardless of whether or not the grain is agglomerated or sintered to form larger entities (polycrystalline). It has been shown, that the particle size as well as the connection of adjacent metal oxide grains, either agglomerated or

^c For strongly electronegative gaseous species like NO_2 a direct adsorption is also proposed:



sintered, affects substantially the conductivity and thus the sensitivity of a sensor. The gas response increases abruptly when the particle size D becomes comparable or smaller than the depletion layer thickness L , which for example, is determined to 5-15 nm for SnO_2 grains. Furthermore, a proportional relation between the sensitivity to $1/D$ was obtained by theoretical simulation, confirming the experimental results.^[104, 105] In this regard, a semiquantitative model was proposed by Xu et al., which concerns the relationship between grain size D and L of sintered and agglomerated grains, whereas three different cases can be distinguished, illustrated in *Figure 9*.

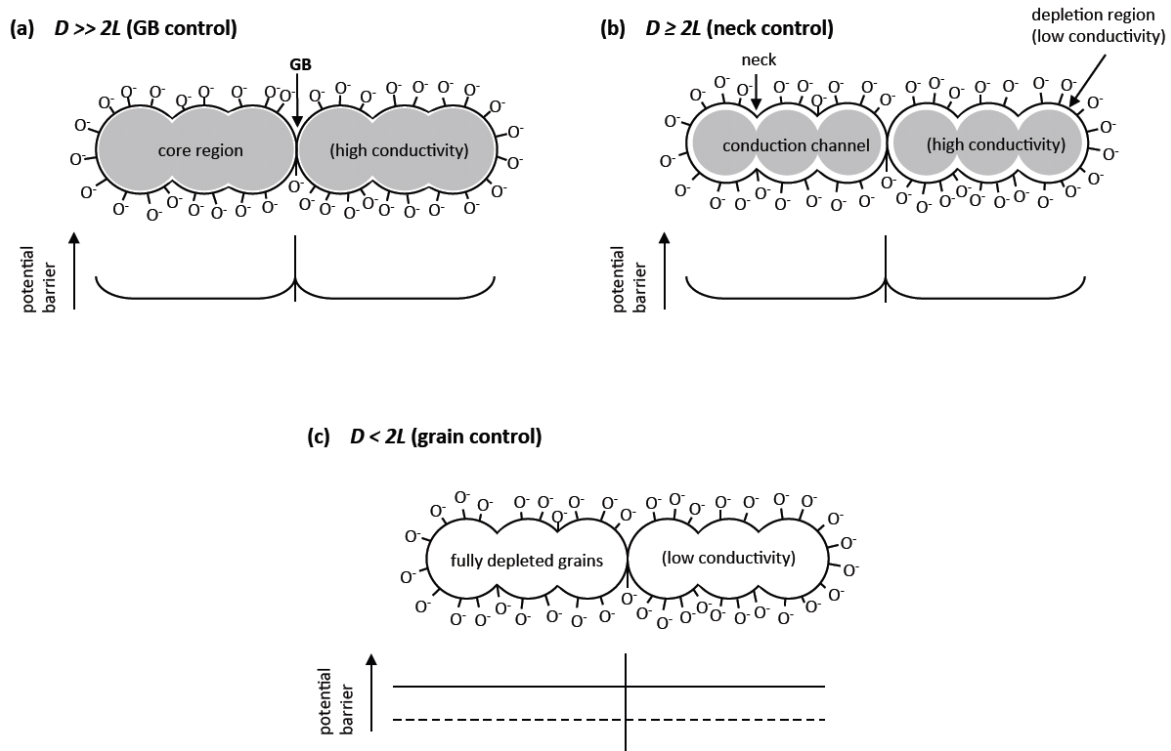


Figure 9. Model of grain size effect in n-type semiconducting metal oxide gas sensor. (a) $D \gg 2L$, conductivity is grain boundary controlled, (b) $D \geq 2L$, the conductivity is neck controlled, (c) $D < 2L$, the conductivity is grain controlled. Illustration modified according references^[89, 105]

In case of large grains with a small surface-to-volume ratio, L is significantly smaller than the single crystallite size ($D \gg 2L$). Most of the volume of the crystallites is unaffected by the surface interactions with the gas phase. Basically, the conductivity depends on the grain boundary barrier height (GB) for intercrystallite charge transport from one grain to another (see *Figure 9*, a) and is therefore independent of the grain size (grain boundary controlled). In case of higher surface-to-volume ratio, *i.e.* smaller grains but still larger than twice the

depletion layer ($D \geq 2L$), that region extends into the grains forming constrictions, so called *necks* (see *Figure 9, b*). As a consequence, the conductivity is affected by the cross section area of these necks which is dependent on the ambient gas composition (neck controlled). Compared to the former case ($D \gg 2L$) the mentioned constriction effect adds up to the effect of GB barriers resulting in an improvement of the gas sensitivity. Again, oxidizing gases increase the depletion layer thickness leading to smaller necks, whereas reducing gases cause a decrease, resulting in larger necks. When $D < 2L$, the depletion layer extends throughout the whole grain and the crystallites are almost entirely depleted (see *Figure 9, c*). Thus the conductivity decreases steeply since the conduction channels between the grains are gone. The energy bands are nearly flat throughout the whole structure of the interconnected grains, and since there are no significant barriers for intercrystallite charge transport the conductivity is primarily controlled by the intracrystallite conductivity (grain controlled). It was found empirically as well as theoretically, that the highest gas sensitivity towards reducing gases (CO and H_2) is obtained in this case. Already very small variations in the trapped charge density lead to a significant change in the effective carrier concentration and finally in the electrical conductivity. Moreover, a proportional relation between the sensitivity to $1/D$ was found theoretically by Rothschild^[105], approving the results previously obtained experimentally by Xu et al.^[104] The considerations reveal, that high surface-to-volume ratios, present in mesoporous metal oxides, are desired for gas sensing purposes. A more extensive discussion about the complex processes of the gas detection is given in some recent reviews.^[89, 102, 103]

For evaluation of the gas sensing properties the change in resistance of a metal oxide layer with a thickness of ca. 10 μm was determined under varying ambient conditions. The measurement of the sensing layers resistance was accomplished with a commercially available sensor device (Umweltsensortechnik, UST), consisting of 3 x 3 mm alumina substrates with integrated platinum electrodes and an integrated platinum heater (Pt-10) see *Figure 10 (a)*. A photograph of the platinum electrodes for the resistance measurement is shown in *Figure 10 (b)*; the distance between the electrodes was 38 μm . For preparation of gas sensors, 20 mg of mesoporous metal oxide powder were ground and dispersed in 2 ml deionized water. The dispersion was deposited onto the sensor device, dried at room temperature, and tempered for 24 hours at 350 °C.

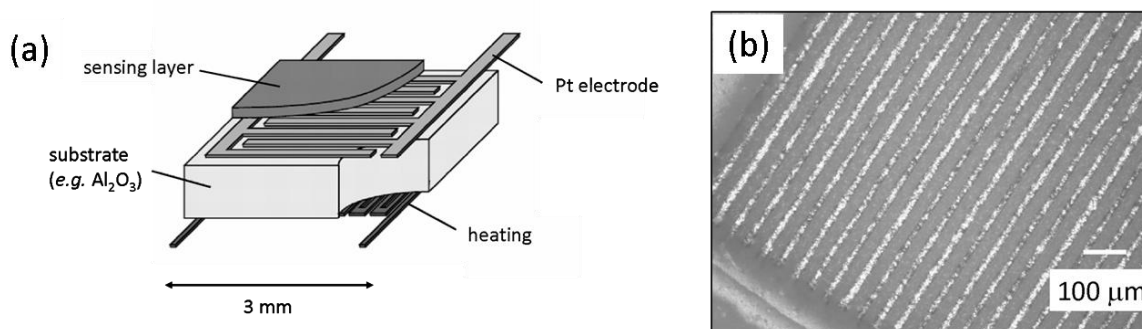


Figure 10. Schematic drawing of an example sensor substrate. Modified according to reference.^[89]

ZnO samples (*section 4.6*) were measured with a constant voltage of 0.5 V. The resistance of In₂O₃ samples (*section 5.6*) were determined with a logarithmic amplifier to cover the high dynamic of sensors resistance especially required under ozone exposure. The bias voltage was set to 0.5 V. Due to potential polarization effects, mesoporous SnO₂ samples (*section 6.5*) were measured utilizing a Keithley Electrometer amplifier (Keithley 6517A) with a pulsed bias voltage of 0.5 V and pulse length of 100 ms.

Part III – Results and Discussion

4. Synthesis and characterization of mesoporous zinc(II) oxide

4.1 Zinc oxide

Zinc oxide (ZnO) is a transparent, non-toxic, II-VI, wide band gap (3.20 – 3.40 eV) semiconductor, having *n*-type conductivity which is due to intrinsic defects such as oxygen vacancies or zinc interstitials acting as electron donors. It crystallizes in two forms, the cubic ‘zincblende’ (‘sphalerite’) and hexagonal ‘wurtzite’ structure, the latter being the thermodynamically stable form. ZnO is widely used for example in fields of pharmaceuticals, optoelectronics, catalysis and gas sensing. The high interest in ZnO materials in these days is reflected in more than 2000 ZnO-related publications in 2005 alone.^[106]

4.2 Synthesis and characterization of mesoporous templates

4.2.1 Synthesis and characterization of mesoporous SBA-15

The synthesis of SBA-15 silica was accomplished in a modification of a literature procedure.^[107] 12.0 g of P-123 block copolymer (Sigma) were dissolved at 35 °C in a mixture of 360 g deionized water and 43.0 g hydrochloric acid (32 %) for 24 hours. After addition of 24.0 g of tetraethylorthosilicate (TEOS; Merck) the mixture was stirred at 35 °C for 24 hours. The resulting gel was transferred to a Teflon-lined autoclave and kept for 24 hours at 80 °C for a mesopore diameter of 7 nm, or at 140 °C for a mesopore diameter of ca. 10 nm respectively. The resulting solid product was filtered off and washed with deionized water. For the removal of the P-123 block copolymer the dried product was calcined under air atmosphere at 550 °C for 6 hours (heating rate 2 °C·min⁻¹).

Figure 11 (left) shows the low-angle XRD patterns of two representative mesoporous SBA-15 samples synthesized at 80 °C and 140 °C (denoted in the following as *SBA-15-80* and *SBA-15-140*). The diffraction patterns of both samples show three well-resolved peaks indicating long-range structural order. The three peaks can be indexed as (100), (110) and (200) according to a hexagonal *p6mm* array of mesopores. A typical characteristic of ordered mesoporous silica phases is the increase of the repeat distance with increasing time and/or temperature of hydrothermal treatment during synthesis.^[108] Accordingly, the *d*-value (*d*₁₀₀) of *SBA-15-80* is about 1 nm smaller than that of *SBA-15-140*. The long-range

order of the pore system is further confirmed by TEM analysis. *Figure 11* (right) shows a representative image perpendicular to the pore axis.

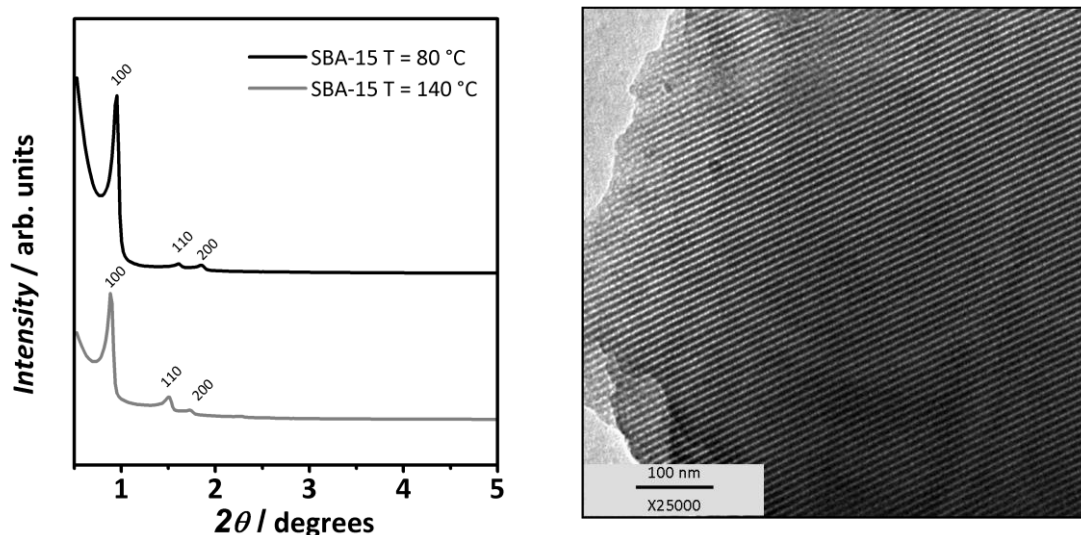


Figure 11. Low-angle P-XRD pattern of mesoporous SBA-15, synthesized at distinct temperatures (left). TEM image of mesoporous SBA-15 silica with view perpendicular to the pore axis (right).

Nitrogen physisorption analysis of the mesoporous SBA-15 samples is shown in *Figure 12* (left). Both materials exhibit type IV isotherms with a sharp step in the adsorption branch and a pronounced hysteresis (H1 type) in the desorption branch, which is characteristic of materials with cylindrical mesopores. The capillary condensation step occurs for *SBA-15-80* at a relative pressure of $p/p_0 \approx 0.7$ which is shifted to higher relative pressures of $p/p_0 \approx 0.8$ for *SBA-15-140*. The pore size distributions obtained by NLDFT calculations are shown in *Figure 12* (right). Both samples show a narrow pore size distribution with a maximum of 7.3 nm and 10.1 nm for SBA-15 synthesized at 80 °C and at 140 °C, respectively. The FWHM of the distribution is somewhat broader for *SBA-15-140* which is attributed to the existence of complementary mesopores interconnecting adjacent channels through the silica wall (see also *section 1.2.2.1*).^[35, 109] The calculated specific surface areas of the mesoporous silica samples using the BET model are 530 m²·g⁻¹ and 900 m²·g⁻¹ for *SBA-15-140* and *SBA-15-80*.

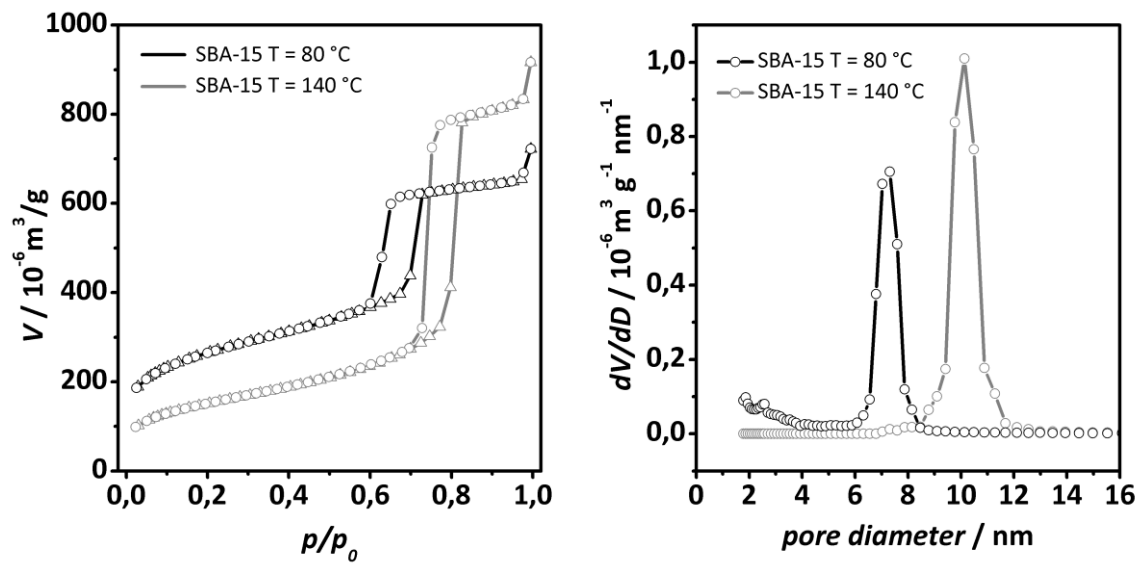


Figure 12. Nitrogen physisorption isotherms of mesoporous SBA-15 silica samples synthesized at distinct temperatures (left) and their corresponding pore size distributions calculated by the NLDFT model (right).

The average pore wall thickness h was calculated by combining the average pore size D_h with the information obtained from the P-XRD data. For the 2-D hexagonal ($p6mm$) symmetry this is achieved by

$$h = a - D_h \quad (5)$$

where the lattice constant a is calculated from the d_{100} value by

$$a = 2d_{100} / \sqrt{3} \quad (6)$$

The average pore wall thickness decreases with increasing temperature of hydrothermal treatment. For *SBA-15-80*, h is calculated to 3.4 nm and for *SBA-15-140* to 1.5 nm which is in good agreement with the results from Zhao et. al.^[107] Table 4 summarizes the results again.

	d_{100} [nm]	average pore width D_h (NLDFT) [nm]	average pore wall thickness h [nm]	specific surface area A_{BET} [m ² ·g ⁻¹]	pore volume [cm ³ ·g ⁻¹]
SBA-15-80	9.3	7.3	3.4	900	1.3
SBA-15-140	10.0	10.1	1.5	529	1.0

Table 4. Structural data of mesoporous SBA-15 silica synthesized at distinct temperatures.

4.2.2 Synthesis and characterization of mesoporous CMK-3

The fabrication of mesoporous CMK-3 carbon was accomplished in a variation of a literature procedure.^[66] In a representative synthesis 2 g of a SBA-15 silica was added to a solution obtained by dissolving 2.5 g of sucrose ($C_{12}H_{22}O_{11}$) and 0.3 g of sulfuric acid (H_2SO_4) in 10 g of water. The mixture was placed in a drying oven for initially 6 hours at 100 °C, and subsequently for further 6 hours at 160 °C. During the thermal treatment the sample turned dark brown or black. For a complete pore filling the silica sample, containing partially polymerized and carbonized sucrose at this stage, was treated again at 100 °C and 160 °C after the addition of 1.6 g of sucrose, 0.18 g of H_2SO_4 and 10 g of H_2O . The carbonization was completed by pyrolysis with heating to 900 °C for 5 hours under vacuum applying the following temperature program:

<i>temperature [°C]</i>	<i>heating rate [°C·min⁻¹]</i>
up to 300	10
300-360	1
360-900	5

The carbon-silica composite obtained after pyrolysis was immersed in 5 wt % hydrofluoric acid (HF) at room temperature to remove the silica template. The carbon product thus obtained was filtered, washed with ethanol, and dried at 120 °C. To verify an almost complete removal of the template, gravimetric analysis was carried out which delivered a residual silica content of less than 2 wt %.

Figure 13 (left) shows the low-angle XRD patterns of a representative mesoporous SBA-15 sample and its nanocast mesoporous carbon replica (CMK-3). The CMK-3 shows one intensive and two less intensive reflections which indicate a long-range structural order of the material, also confirmed by TEM analysis (*Figure 13, right*). The low-angle reflections of the CMK-3 can be assigned to a hexagonal $p6mm$ symmetry of the ordered pore system and indexed as (100, 110 and 200), corresponding to the SBA-15 structure. Compared to the parental SBA-15, the diffraction peaks of the CMK-3 are shifted to larger 2θ angles which is the result of a structural shrinkage caused by the high-temperature treatment during the synthesis.^[66, 68, 109]

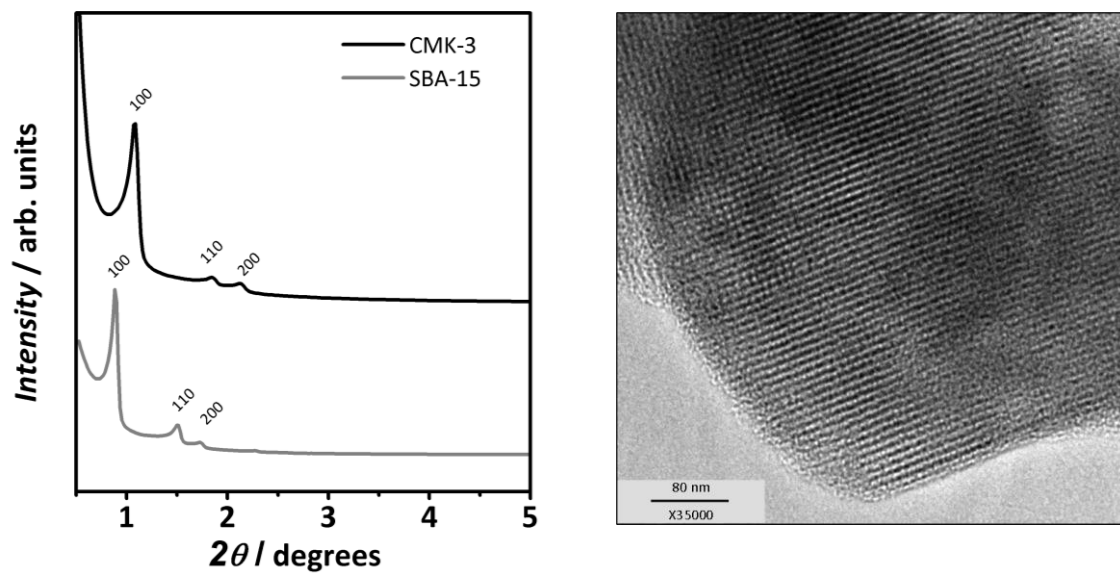


Figure 13. Low-angle P-XRD pattern of mesoporous CMK-3 carbon and its SBA-15 structure matrix (left). TEM image of mesoporous CMK-3 carbon mostly perpendicular to the pore axis (right).

Figure 14 shows the nitrogen physisorption isotherms of the CMK-3 and SBA-15 sample (left) with the corresponding pore size distributions obtained by NLDFT calculations (right).

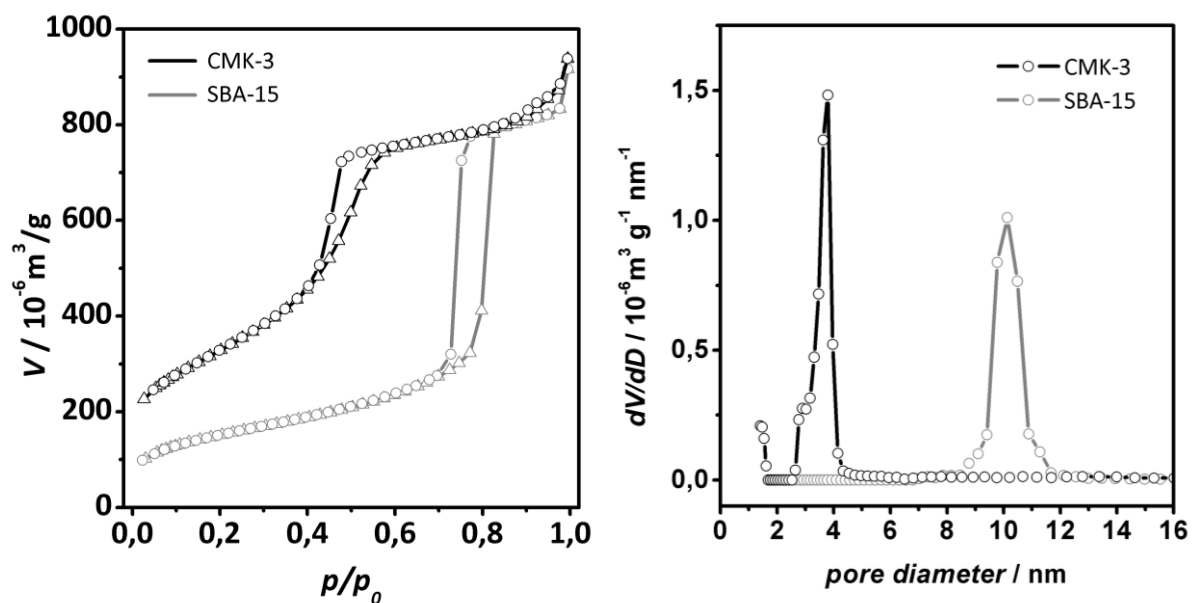


Figure 14. Nitrogen physisorption isotherms of mesoporous CMK-3 carbon and SBA-15 silica (left) and the corresponding pore size distributions calculated by the NLDFT model (right).

The isotherm of the CMK-3 can be assigned to type IV, with a capillary condensation step at $p/p_0 \approx 0.4$. The characteristic of the hysteresis indicates the presence of slit pores, which is

expected for a negative replica of a cylindrical pore arrangement (see also *section 1.2.2.2*). The specific surface area of the CMK-3 sample is $1320 \text{ m}^2\cdot\text{g}^{-1}$ (BET), the total pore volume is determined as $1.5 \text{ cm}^3\cdot\text{g}^{-1}$ (NLDFT). The average pore wall thickness of the CMK-3 is calculated as 5.7 nm.

With regard to a perfect replica, the differences in the structural parameters of CMK-3 and the silica, *e.g.* $D_h(\text{silica}) > h(\text{CMK-3})$ or $h(\text{silica}) < D_h(\text{CMK-3})$ can be explained with the structural shrinkage already mentioned. *Table 5* summarizes the results again.

	d_{100} [nm]	average pore width D_h (NLDFT) [nm]	average pore wall thickness h [nm]	specific surface area A_{BET} [$\text{m}^2\cdot\text{g}^{-1}$]	pore volume [$\text{cm}^3\cdot\text{g}^{-1}$]
SBA-15	10.0	10.1	1.4	529	1.4
CMK-3	8.1	3.7	5.7	1320	1.5

Table 5. Comparison of the structural data of mesoporous SBA-15 silica and the nanocast CMK-3 carbon.

4.3 Impregnation of mesoporous carbon with $\text{Zn}(\text{NO}_3)_2$

The efficient infiltration of ZnO precursor in mesoporous carbon is a key factor for a sufficient pore filling and a complete cross-linking of the material inside the pore system (see also *section 1.2.3*). $\text{Zn}(\text{NO}_3)_2$ was chosen as the precursor due to its high solubility in water as well as in tetrahydrofuran (THF), which has been turned out to be the most suitable solvent for a good wettability of the non-polar carbon surface (see below). Furthermore, $\text{Zn}(\text{NO}_3)_2$ has a low decomposition temperature of ca. 180 °C and the by-products are all gaseous and are therefore easily removable from the pores of the matrix. As an alternative to the utilization of THF, a surface modification of the non-polar carbon surface can be accomplished so that polar solvents like water can be used for an efficient impregnation.

*For surface modification 10 ml of nitric acid (HNO_3 ; 32 %) were added to 0.2 g of thick-walled CMK-3 carbon (see *section 1.2.3*) in a teflon autoclave and exposed to microwave irradiation (MARS 5, 300 W). The samples were heated under stirring to 110 °C within 3 min and kept at that temperature for another 15 min. The carbon was filtered off, washed with deionized water and dried at 60 °C for 12 hours. The samples were finally characterized by XRD and*

physisorption to verify that the structural integrity was retained. In addition, IR spectra confirm the surface modification by the appearance of a band at 1735 cm^{-1} , assignable to C=O stretching of carboxyl and carbonyl groups, not observed in the pristine material.

Table 6 shows the structural data of a typical surface modification treatment.^d

	d_{100} [nm]	average pore width D_h (NLDFT) [nm]	average pore wall thickness h [nm]	specific surface area A_{BET} [$\text{m}^2\cdot\text{g}^{-1}$]	pore volume [$\text{cm}^3\cdot\text{g}^{-1}$]
CMK-3 pristine	8.1	3.6	5.8	1400	1.17
CMK-3 modified	8.1	3.6	5.8	1250	1.00

Table 6. Comparison of the structural data of mesoporous pristine and modified CMK-3.

To achieve optimum conditions for the impregnation procedure the loading rates of various impregnation strategies were explored by determination of the pore volume and the surface area after two consecutive cycles of impregnation and conversion into the oxide. To investigate the impact of the solvent polarity, samples of mesoporous carbon were impregnated with solutions of $\text{Zn}(\text{NO}_3)_2$ in THF and water. In addition to this, further experiments with varying concentrations of the precursor in the appropriate solvent were carried out. The influence of a surface modification and the impregnation with the *incipient wetness* technique were examined too.

Figure 15 shows the results for the impact of the solvent polarity (left) and the precursor concentration (right) on the specific surface area and the pore volume after one and two consecutive cycles of impregnation and conversion into the oxide. In both experiments the structure matrices were impregnated by the *wet impregnation* technique. Concerning the influence of the solvent polarity, the specific surface area as well as the pore volume decrease from cycle to cycle for both solvents, but the decrease is more pronounced (about 12 % for each of both cycles) when THF is used as the solvent instead of water.

^d A more detailed characterization including XRD pattern, physisorption isotherms and IR spectra can be found in reference [82].

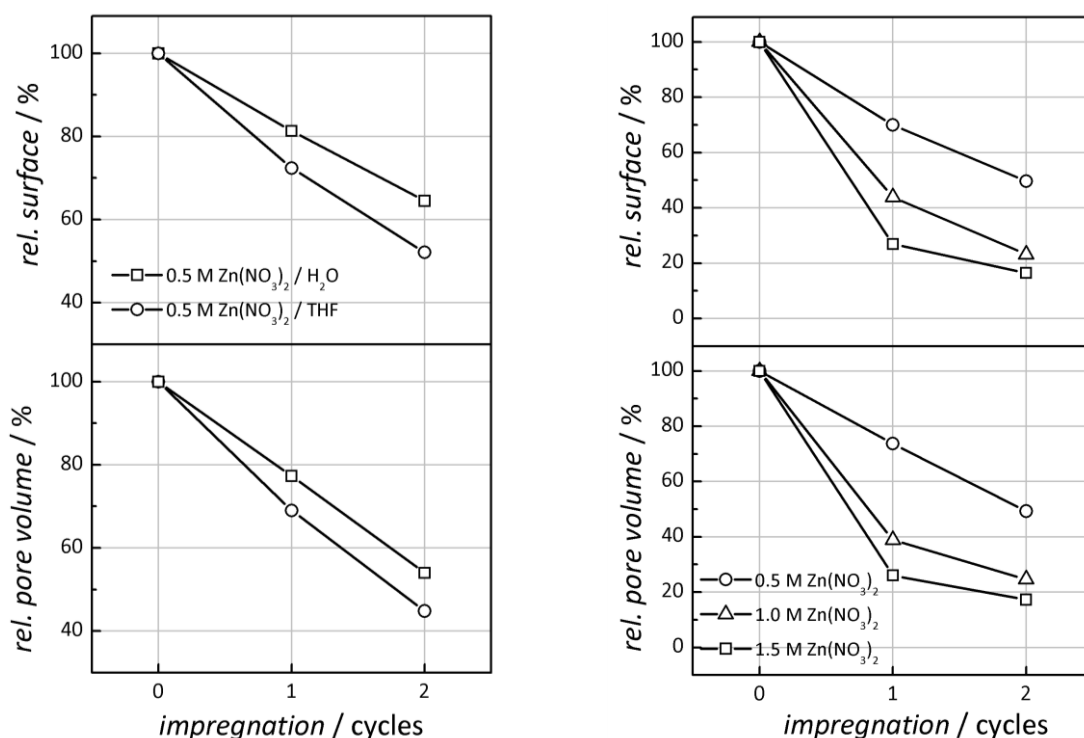


Figure 15. Influence of the solvent polarity (left) and the concentration (right) of precursor solutions on the decrease of relative surface area and pore volume in mesoporous carbon after consecutive cycles of impregnation with $\text{Zn}(\text{NO}_3)_2$. Measurements were carried out after conversion into ZnO .

This result can be explained by the lower polarity of the THF molecule, which leads to a better wettability of the hydrophobic carbon surface. *Figure 15* (right) shows the influence of the precursor concentration with THF as the solvent. After two impregnation cycles a pore filling of approximately 80 % can be achieved using a 1.5 M solution of $\text{Zn}(\text{NO}_3)_2$.

Figure 16 (left) shows the results of impregnating a carbon matrix with and without a post-synthetic surface modification using a 0.5 M $\text{Zn}(\text{NO}_3)_2$ in water solution (wet impregnation technique). An almost complete pore filling is obtained for the surface modified matrix after the second cycle, the pore volume as well as the surface area decrease more than 80 %. Similar results are obtained when the carbon matrix is impregnated by the incipient wetness technique with a saturated $\text{Zn}(\text{NO}_3)_2$ solution in THF (2.5 M); here a pore filling of ca. 85 % is obtained after two cycles (*Figure 16*, right).

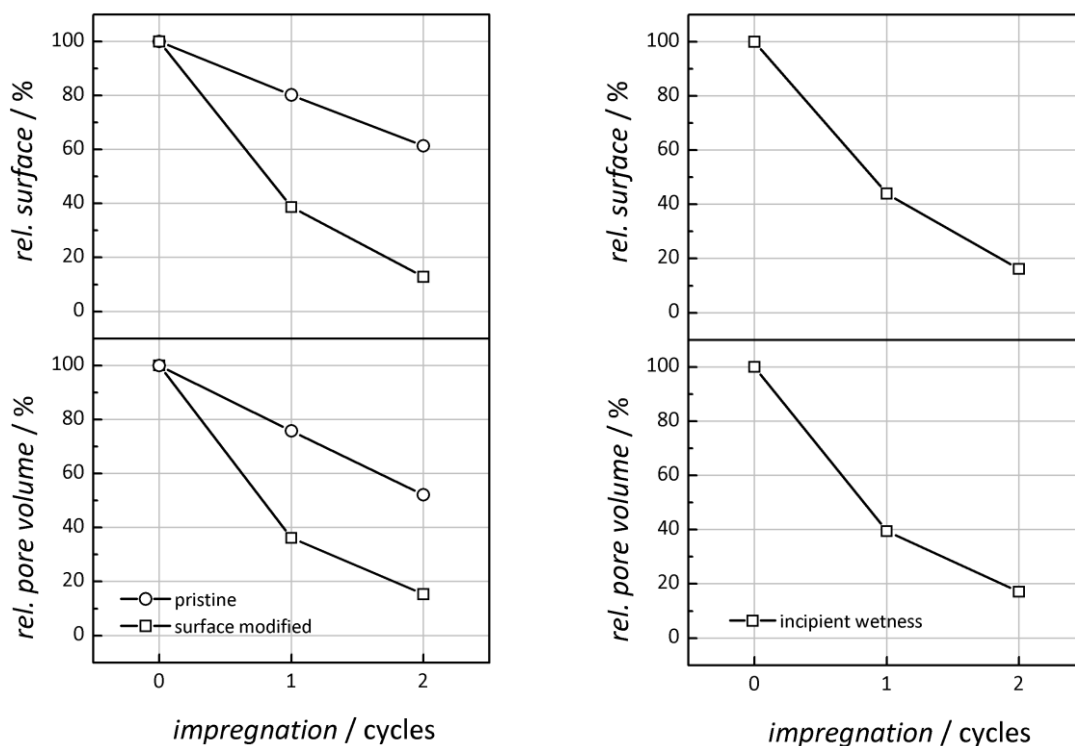


Figure 16. Influence on the relative surface area and pore volume after consecutive cycles of impregnation and oxide formation, on pristine and surface modified mesoporous carbon (left) and the application of the incipient wetness technique (right).

4.4 Conversion of ZnO precursor and template removal

The thermal conversion of $\text{Zn}(\text{NO}_3)_2$ into ZnO and the subsequent removal of the carbon matrix are, apart from an efficient impregnation, a key factor for the successful synthesis of the mesoporous zinc oxide. The conditions for the thermal decomposition of $\text{Zn}(\text{NO}_3)_2$ must be carefully selected in order to remain the structural integrity of the carbon matrix and to obtain a complete conversion into the oxide. On the other hand, the template removal procedure should preserve the structural integrity of the resulting metal oxide and ensure a complete template removal. Even though high temperatures are necessary for the carbon template removal on the one hand, too high temperatures might damage the metal oxide structure on the other hand.^[52] To determine the suitable temperature conditions for the template removal procedure, TG-MS analysis was carried out. A carbon matrix impregnated with $\text{Zn}(\text{NO}_3)_2$ was heated under synthetic air atmosphere to 1100 °C with a heating rate of 5 °C·min⁻¹ to track the oxide formation as well as the template combustion.

Figure 17 shows the TG curve and its first derivative (DTG) together with mass ion detection signals (MS). The mass loss of the sample occurs in two major steps, the first one between 70 and 220 °C and the second one between 250 and 630 °C. The first step corresponds to the conversion of $\text{Zn}(\text{NO}_3)_2$ into ZnO which is confirmed by the detection of nitric oxide (NO^+ , $m/z = 30$) and the release of residual water (H_2O^+ , $m/z = 18$). In the range of the oxide formation temperature, small quantities of CO_2 are formed indicating a partial oxidation of the carbon matrix which ends simultaneously with the nitrate decomposition at 220 °C. The second step, with a mass loss of ca. 40 %, corresponds to the total combustion of the carbon matrix, verified by the detection of CO_2 (CO_2^+ , $m/z = 44$).

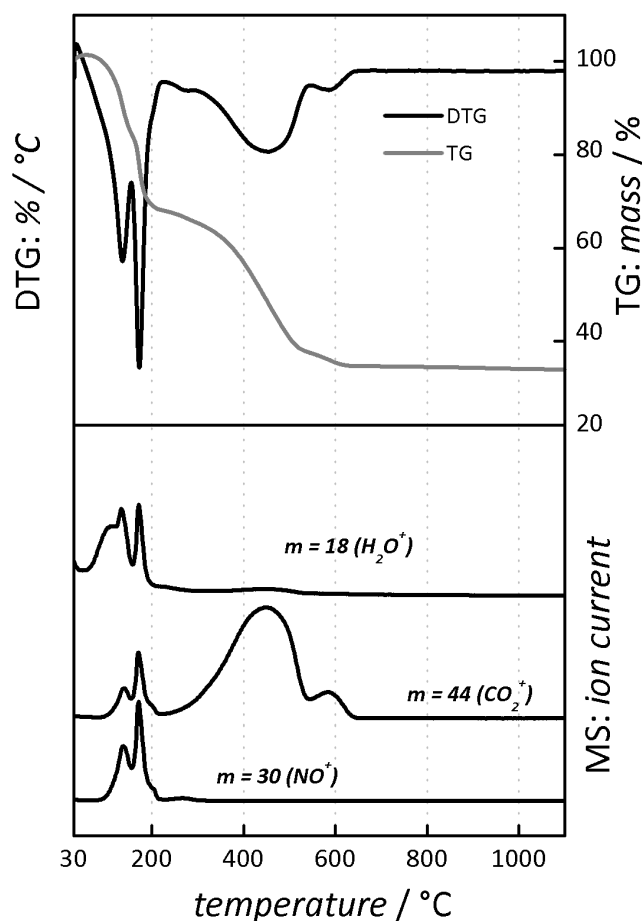


Figure 17. Coupled thermogravimetry (TG) and mass ion detection for CMK-3 carbon impregnated with $\text{Zn}(\text{NO}_3)_2$.

The DTG curve reveals that the main mass loss occurs in the range of 450 to 480 °C. Both processes, decomposition of $\text{Zn}(\text{NO}_3)_2$ and combustion of the CMK-3 matrix, seem to overlap in the temperature to a certain degree.

4.5 Synthesis of mesoporous ZnO

In a typical synthesis, mesoporous ZnO was prepared by immersing 0.5 g CMK-3 carbon in 20 ml of a solution of $\text{Zn}(\text{NO}_3)_2$ in THF (1.5 M) and stirring at room temperature for 6 hours. After filtration the impregnated carbon was dried at ambient temperature, heated under air atmosphere to 200 °C with a constant rate of $2.5\text{ °C}\cdot\text{min}^{-1}$, and kept at that temperature for two hours to convert zinc nitrate quantitatively to zinc oxide, according to the results of TG-MS measurements. This procedure was repeated twice, before removal of the carbon matrix by heating under air to 550 °C with a heating rate of $2.5\text{ °C}\cdot\text{min}^{-1}$ and keeping at that temperature for two hours, to achieve a quantitative template removal.

4.5.1 Characterization of composite materials

Figure 18 (left) shows the low-angle XRD pattern of a representative series of ZnO/CMK-3 composite materials after several cycles of impregnation and subsequent conversion into the oxide. The intensities of the reflections decrease with every cycle, which indicates an increased filling of the pores with ZnO that diminishes the scattering contrast. After the second cycle, only a slight shoulder is observed. The wide-angle pattern (right) confirm the formation of crystalline ZnO with the hexagonal wurtzite structure.

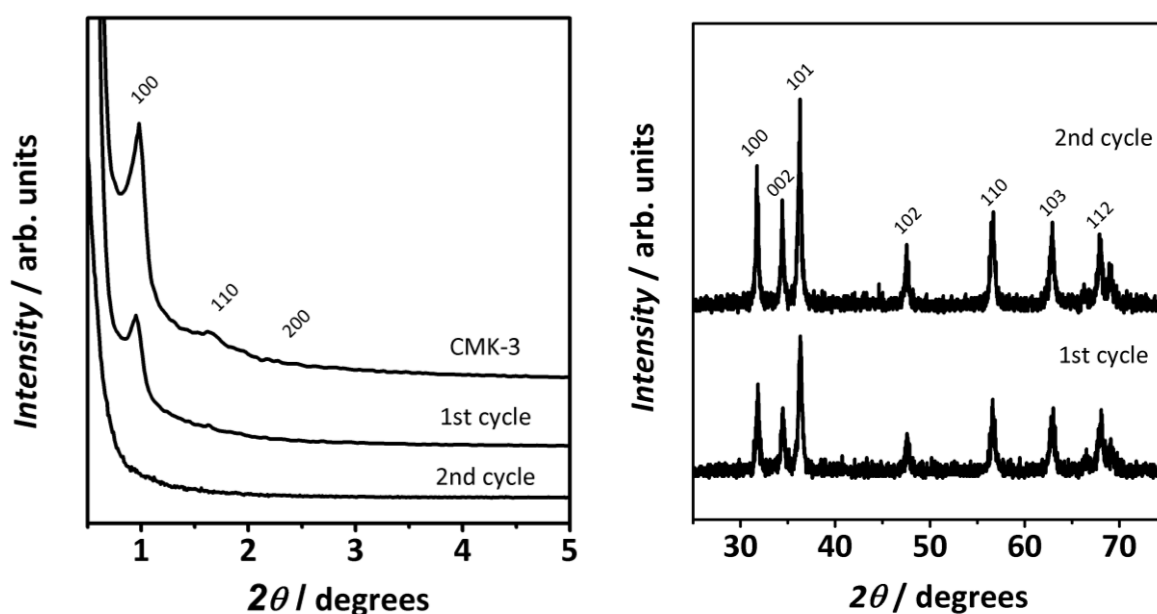


Figure 18. Low-angle P-XRD pattern of mesoporous CMK-3 carbon and ZnO/CMK-3 composite materials obtained after each cycle of impregnation and oxide formation (left) and the associated wide-angle pattern (right).

The reflections of the ZnO composite material are somewhat broader than that of bulk ZnO material, indicating that the crystalline domains formed in the confined space are quite small.^e Figure 19 shows the physisorption isotherms (left) and the corresponding pore size distributions, calculated by the BJH model (right) after each cycle.

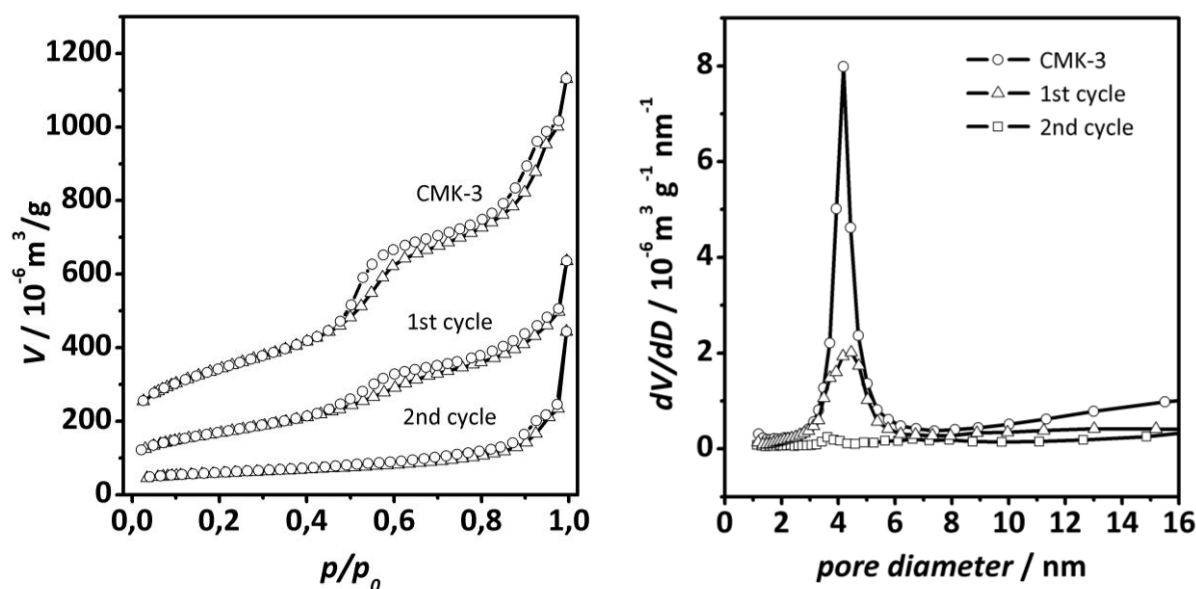


Figure 19. Nitrogen physisorption isotherms of mesoporous CMK-3 and ZnO/CMK-3 composite materials obtained after each cycle (left) and the corresponding pore size distribution determined by the BJH model (right).

The capillary condensation step of the isotherms becomes less pronounced with progressing cycles, indicating a decrease in porosity. This is caused by an increased filling of the pores with zinc oxide, reflected in a significant decrease in the surface areas and pore volumes of the sample, as summarized in Table 7.

	d_{100} [nm]	average pore width D_h (BJH) [nm]	specific surface area A_{BET} [$\text{m}^2 \cdot \text{g}^{-1}$]	pore volume [$\text{cm}^3 \cdot \text{g}^{-1}$]
CMK-3	9.1	4.2	1165	1.53
1 st cycle	9.1	4.3	580	0.77
2 nd cycle	-	-	193	0.27

Table 7. Overview of the structural data of CMK-3 carbon and ZnO/CMK-3 composites.

^e The XRD pattern of these materials were recorded with a Bruker AXS D8 Advance diffractometer. The data were collected in a step scan mode of $2\theta = 0.01^\circ$ and a counting time of 4 s per step for the low-angle region. For the wide-angle region, diffractograms were recorded with a step of $2\theta = 0.02^\circ$ and a counting time of 2 s per step.

No significant shift is observed in the pore size distribution. This indicates that the growth of zinc oxide material takes place predominantly along the pore axis rather than from the pore walls towards the pore center. In the latter case a pronounced shift of the average pore width towards lower values would have to be expected. This aspect will be considered in more detail in *section 5.4.4.* and *5.4.5.*

4.5.2 Characterization of mesoporous ZnO

Figure 20 shows the low- and wide -angle XRD pattern of mesoporous ZnO after removal of the CMK-3 carbon matrix. In the low-angle region (left) a small shoulder at $2\theta \approx 1.00$ ($d_{100} = 8.8 \text{ nm}$) can be observed which is attributable to the 100 reflection. The peak is much less pronounced compared to that of the related CMK-3 template, and furthermore the 110 and 200 peaks cannot be observed in the ZnO replica, indicating a loss of the long-range order. This might be a result of the template deterioration during the oxide formation (see also *section 4.4*). Still, a large number of particles with ordered mesoporosity are observed in TEM analysis. *Figure 21* shows representative TEM images with the mesopores being oriented perpendicular (left) and along (right) to the pore axis.

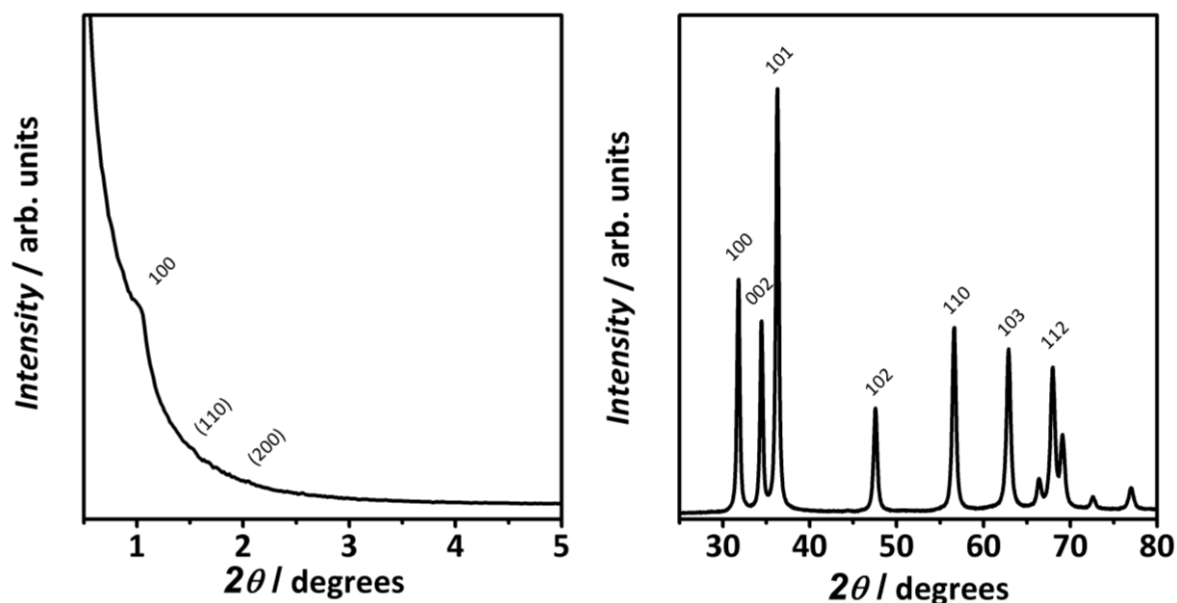


Figure 20. Low-angle (left) and wide-angle (right) P-XRD pattern of mesoporous ZnO.

The wide-angle diffraction pattern (*Figure 20*, right) shows well-resolved peaks which can be indexed according to the expected hexagonal wurtzite structure. In comparison, the

reflections of nanocast mesoporous ZnO are somewhat broader than these of commercially available bulk ZnO, indicating the presence of a polycrystalline material. The average crystallite size $S_{\text{crystallite}}$ was calculated as 7.2 nm by application of the SCHERRER formula (7) to the 110 peak ($2\theta = 56.6^\circ$, FWHM = 1.2°).

$$S_{\text{crystallite}} = \frac{k \cdot \lambda}{FWHM \cdot \cos \theta} \quad (7)$$

with

k = Scherrerconstant (depends on the geometry of the crystal system: hexagonal = 0.9)

λ = wavelength of incident X-rays

FWHM = full width half maximum

θ = diffraction angle

Taking into account that this value is just a rough approximation, the crystalline domain size of the mesoporous ZnO is in the range of the wall thickness of the material. This structural property has already been described for several nanocasted polycrystalline metal oxides such as MgO and CeO₂.^[75, 79] The polycrystalline nature of the mesoporous ZnO is also confirmed by the selected area electron diffraction (SAED) pattern. Insets of *Figure 21* show representative patterns consisting of single spots super-imposed on diffuse rings, which confirms a polycrystalline material with small crystalline domains. Energy dispersive X-ray analysis of the spots (EDX) reveal that the sample consists to more than 99% of ZnO.

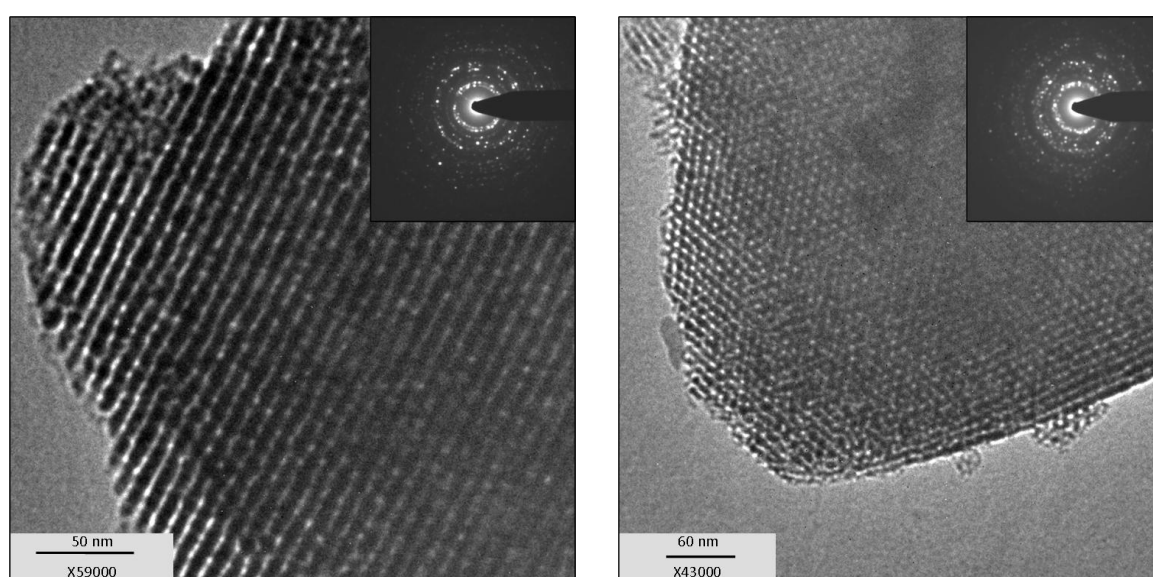


Figure 21. TEM images of mesoporous ZnO, perpendicular (left) and along the pore axis (right). The insets display the corresponding SAED pattern.

Nitrogen physisorption measurements (*Figure 22*) show a type IV isotherm (left) with a steep increase at $p/p_0 \approx 0.7$ and a H1 hysteresis which is typical for larger cylindrical mesopores. These are expected for the negative replica of CMK-3 carbon consisting of slit pores (see *section 1.2.2.2*). *Figure 22* (right) displays the corresponding pore size distribution calculated by the NLDFT method with a pronounced peak at 6.5 nm , which is in good agreement with the corresponding wall thickness ($h = 6.3 \text{ nm}$) of the carbon template. Also, the wall thickness ($h = 3.7 \text{ nm}$) approximately corresponds with the pore size of the mesoporous carbon ($D_h = 4.2 \text{ nm}$). The specific surface area, calculated by the BET method, and the total pore volume are $51 \text{ m}^2 \cdot \text{g}^{-1}$ and $0.24 \text{ cm}^3 \cdot \text{g}^{-1}$, respectively.

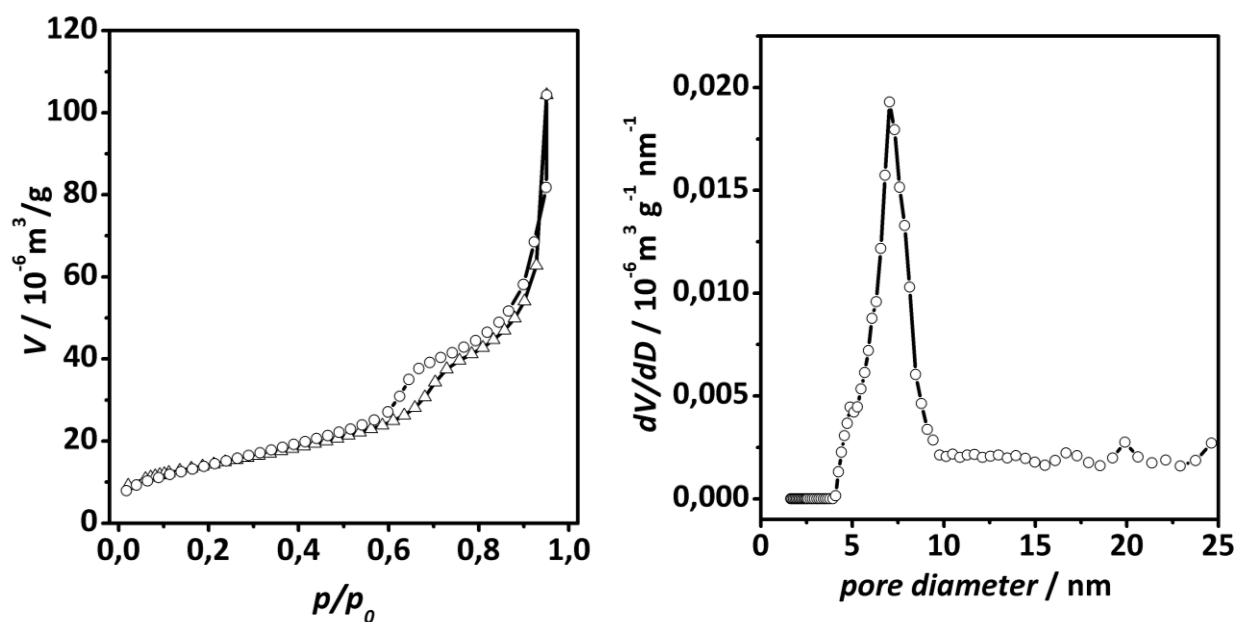


Figure 22. Nitrogen physisorption isotherms of mesoporous ZnO (left) and the corresponding pore size distribution obtained by the NLDFT model (right).

Both values are significantly lower than those of the templates' (see also *Table 8*), which can partly be explained by differences in the densities of silica ($\rho = 2.2 \text{ g} \cdot \text{cm}^{-3}$) and carbon ($\rho \approx 1.8 - 2.1 \text{ g} \cdot \text{cm}^{-3}$) in comparison to ZnO ($\rho = 5.6 \text{ g} \cdot \text{cm}^{-3}$).^[110] Another potential reason for the discrepancy is the lower surface roughness of crystalline ZnO, compared to amorphous silica. Moreover, the formation of non-porous ZnO, originating from precursor deposition outside the pores, cannot be excluded; this would additionally decrease the specific surface area as well as the pore volume of the sample.

	d_{100} [nm]	average pore width D_h (NLDFT) [nm]	average pore wall thickness h [nm]	specific surface area A_{BET} [m ² ·g ⁻¹]	pore volume [cm ³ ·g ⁻¹]
SBA-15	9.8	10.1	1.2	484	1.1
CMK-3	9.1	4.2	6.3	1165	1.56
ZnO	8.8	6.5	3.7	51	0.24

Table 8. Overview of the structural data of mesoporous ZnO and the respective templates.

Figure 23 displays representative SEM images of mesoporous CMK-3 carbon (left) and its nanocast ZnO replica (right). No apparent relationship between the morphology of the CMK-3 and the mesoporous ZnO particles can be revealed. The particles of mesoporous CMK-n materials commonly form ropes^[77, 111] or rods^[112] similar to those in the image. This shape is not observed for mesoporous ZnO, whose particles are randomly distributed. Another obvious difference is the particle size determined as 1-2 μm in length and 0.5 μm in width for a representative CMK-3. In contrast to that, the values for mesoporous ZnO material are significantly smaller, and in the range of ca. 50 - 150 nm. A detailed consideration concerning the relations between topology and morphology of templates and its nanocast product are object of a study described in section 5.4.4. and 5.4.5.

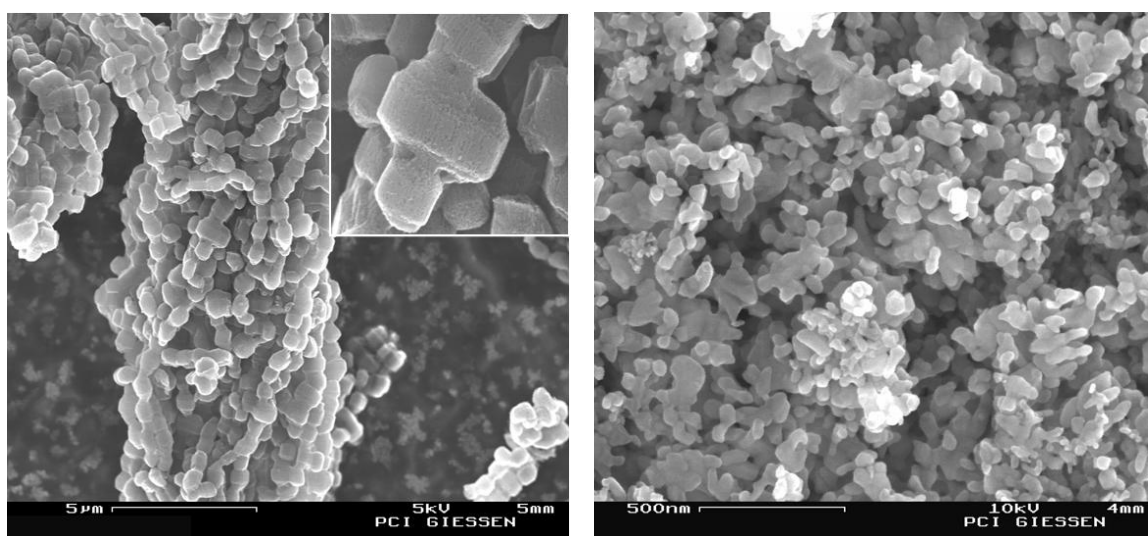


Figure 23. SEM images of mesoporous ZnO (right) compared to its CMK-3 carbon structure matrix (left). Inset of CMK-3 image shows a close-up view of a group of chains.

The ZnO samples were additionally analyzed by Raman and low-temperature photoluminescence (PL) spectroscopy, also confirming the high degree of crystallinity as well as the high surface-to-volume ratio. *Figure 24* depicts the Raman spectrum of mesoporous ZnO in the spectral range between 250 and 750 cm^{-1} obtained in backscattering geometry with unpolarized detection. The spectrum shows all feature characteristics of wurtzite ZnO crystalline material. The fundamental modes are labeled by their symmetry type. The fundamental modes at 389 cm^{-1} [$A_1(\text{TO})$], at 440 cm^{-1} (E_2), at 539 cm^{-1} [$A_1(\text{LO})$], and at 586 cm^{-1} [$E_1(\text{LO})$] can be clearly seen in the spectrum. The 410 cm^{-1} fundamental [$E_1(\text{TO})$] can be distinguished as a weak shoulder to the much stronger E_2 signal. The second fundamental E_2 mode would occur at about 100 cm^{-1} which is outside the detection range of the Raman microscope system used (see *section 3.2.6*). The signals at 333 and 660 cm^{-1} are due to multiphonon processes.

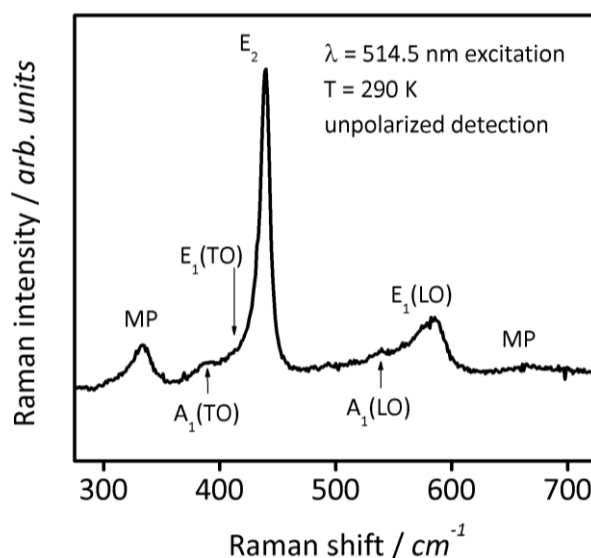


Figure 24. Raman spectrum of mesoporous ZnO.

The low-temperature PL spectrum is shown in *Figure 25*. The band edge and near band edge luminescences are dominant in the entire spectral range from 3.4 to 2 eV, the deep recombinations in the visible spectral range being almost five orders of magnitude lower in intensity. The deep luminescence in the range from 2.6 to 2 eV has its maximum at about 2.3 eV; the band is unstructured and thus not related to the phonon-structured copper green band in ZnO. A straightforward assignment of the defect state involved in this recombination process is not possible. The near band edge luminescence displays two prominent lines at 3.307 and 3.3625 eV, respectively. Lines in the vicinity of 3.31 eV are

commonly observed in P, As, and N doped ZnO films, as well as in NH_3 -annealed ZnO powders. The preparation conditions cannot rule out the incorporation of quantities of group-V elements in the doping range, especially as the purity of the educts was only approximately 99 %. Since the line is 55 meV below the free A-exciton transition, neutral donor or acceptor-bound exciton recombination is not a likely cause. The band edge recombination consists of three transitions: at 3.366, at 3.3625, and at 3.359 eV. The high-energy line may be attributed to ionized donor-bound exciton recombination or surface excitons; the line at 3.359 eV is close to the neutral donor-bound exciton recombination with a Ga donor (18). The line at 3.3625 eV is very close to the I4 recombination line attributed to the hydrogen donor. The incorporation of hydrogen during the chemical synthesis of the material seems unlikely because of the high temperature during the carbon combustion step. This temperature is considerably higher than 500 °C, which is usually sufficient for hydrogen to diffuse out of the bulk ZnO. Therefore, the presence of the hydrogen-related PL line indicates that hydrogen has diffused into the material under ambient conditions in the course of time. This is most likely promoted by the high specific surface area of the material, in addition to the low activation energy for hydrogen diffusion known for bulk ZnO. The I8 recombination line appears to be significantly broadened compared to bulk samples. The broadening is attributed to arising from different local environments of donors situated at the surface and in the interior of the pore walls; this is another manifestation of the high surface-to-volume ratio of the mesoporous ZnO.

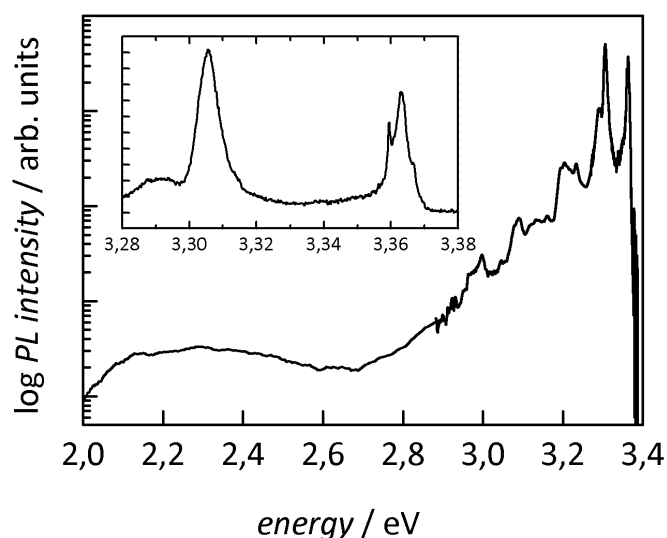


Figure 25. Low-temperature photoluminescence of the mesoporous ZnO (325 nm excitation, $T=4.2$ K). Inset: band edge region.

4.6 Gas sensing properties of mesoporous ZnO

This section concerns the gas sensing properties of mesoporous ZnO for carbon monoxide (CO) and nitrogen dioxide (NO₂) in technically relevant concentrations between 2 and 10 ppm at a relative humidity of 50%. In most countries the legal thresholds for long-term exposure to CO and NO₂ without health damage are specified to 30 ppm and 5 ppm respectively. The performance of the sensor prepared from mesoporous ZnO was compared to that of a bulk (non-porous) ZnO sensor (specific BET surface area: 10 m²·g⁻¹). The measurements were performed at 350 °C operating temperature. *Figure 26* shows the sensitivity, defined as $(G/G_0)-1$, where G is the measured electronic conductance and G_0 the base conductance in absence of the analyte gas. The sensitivity changes with opposite sign, because CO is a reducing gas while NO₂ is oxidizing (see also *section 3.3*). The experiments show a higher sensitivity for the mesoporous sensor compared to the bulk sensor to both gases at each measured gas concentration. The results reveal that mesoporous ZnO synthesized by nanocasting turned out to exhibit superior gas sensing properties for CO as well as NO₂ in comparison to non-porous (bulk) ZnO.

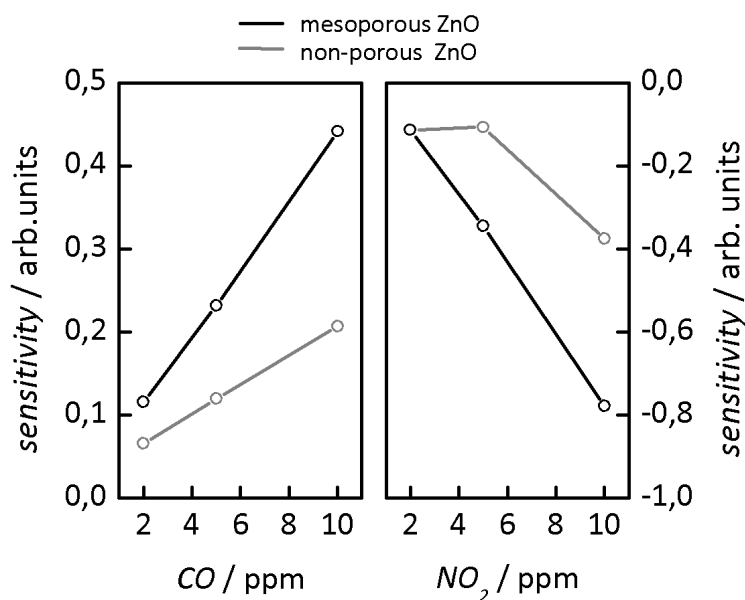


Figure 26. Gas sensing measurements for CO and NO₂ gases at distinct concentrations at a relative humidity of 50 % and an operating temperature of 350 °C.

5. Synthesis and characterization of mesoporous indium(III) oxide

5.1 Indium oxide

Indium oxide crystallizes in two forms, the ‘corundum’ type and the ‘bixbyite’ type. The latter is the thermodynamic stable one. Indium oxide is widely used as a transparent *n*-semiconductor, with a direct band gap of ca 3.0 eV^[113] and an indirect band gap of 2.6 eV.^f Indium oxide and tin-doped indium oxide (ITO) are used for photocatalysis or for transparent conductive coatings in, *e.g.*, flat-panel displays and solar cells. Furthermore In₂O₃ is frequently applied as gas sensor material, especially for ozone sensing.^[93]

5.2 Synthesis and characterization of mesoporous templates

For the synthesis of mesoporous In₂O₃ SBA-15, CMK-3 and KIT-6 silica were utilized as matrices. The synthesis and characterization of mesoporous SBA-15 and CMK-3 are described in *section 4.2.1 and 4.2.2.*

5.2.1 Synthesis and characterization of mesoporous KIT-6

Mesoporous KIT-6 silica was synthesized by a modified literature procedure.^[67] 12.0 g of P-123 block copolymer (Sigma) were dissolved in a mixture of 360 g deionized water and 43.0 g hydrochloric acid (32 %). 12 g *n*-butanol was then added and the solution was stirred for one hour. After addition of 24.0 g of TEOS (Merck) the mixture was stirred at 35 °C for 24 hours. The resulting gel was transferred to a Teflon-lined autoclave and kept for 24 hours at 80 °C for a mesopore width of ca. 7 nm or at 140 °C for a mesopore width of ca. 10 nm, respectively. The samples will be denoted as *KIT-6-80* and *KIT-6-140* in the following. The resulting solid product was filtered off and washed with deionized water. For the removal of the P-123 block copolymer the dried product was calcined under air atmosphere at 550 °C for 6 hours (heating rate 2 °C·min⁻¹).

^f It has to be mentioned that in contrast to other well-known properties, the nature of the band structure and the band gap of bixbyite In₂O₃ remains contentious, this will be depicted below.

Figure 27 (left) shows the low-angle XRD patterns of two representative samples of *KIT-6-80* and *KIT-6-140* silica. The diffraction patterns of both samples show three well resolved peaks indicating a long-range structural order of the materials. The intensive (211) and the three less intensive peaks (220), (420) and (332) can be indexed according to a cubic $Ia\bar{3}d$ structure. Similar to the hexagonal SBA-15 phase (see section 1.2.2.1) the lattice plane increases with time and temperature of the hydrothermal treatment step; the d-value (d_{211}) of *KIT-6-80* is accordingly somewhat smaller than that of *KIT-6-140*. The long-range order of the pore system is further confirmed by TEM analysis (see Figure 27, right).

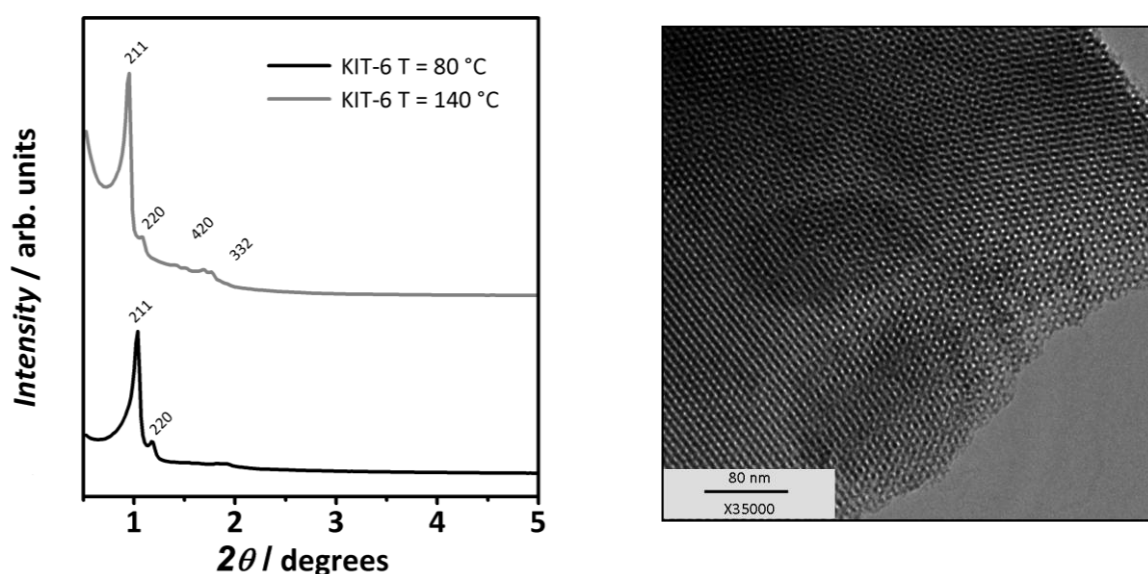


Figure 27. Low-angle P-XRD pattern of mesoporous KIT-6, synthesized at distinct temperatures (left). TEM image of mesoporous *KIT-6-80* (right).

Nitrogen physisorption measurements of the mesoporous KIT-6 samples are shown in Figure 28. Both materials show type IV isotherms (left) with a clear step in the adsorption branch and a pronounced hysteresis (H1 type) in the desorption branch, indicating the presence of cylindrical pores comparable to those of SBA-15 silica. The capillary condensation step occurs for *KIT-6-80* at a relative pressure of $p/p_0 \approx 0.7$ which is shifted to higher relative pressures of $p/p_0 \approx 0.8$ for *KIT-6-140*. The corresponding pore size distributions (NLDFT method) are shown in Figure 28 (right). Both samples show a small pore size distribution with a maximum of 7.3 nm and 10.0 nm for KIT-6 prepared at 80 °C and at 140 °C. The width of the distribution is somewhat broader for *KIT-6-140* (1.7 nm vs. 0.8 nm) which is attributable to the existence of complementary mesopores

interconnecting adjacent channels through the silica wall (see also *section 1.2.2.1*).^[35, 109]

The calculated specific surface areas of the mesoporous silica samples (BET model) are $534 \text{ m}^2 \cdot \text{g}^{-1}$ (*KIT-6-140*) and $920 \text{ m}^2 \cdot \text{g}^{-1}$ (*KIT-6-80*) respectively. The corresponding pore volumes are determined as 1.5 and $1.0 \text{ cm}^3 \cdot \text{g}^{-1}$, respectively.

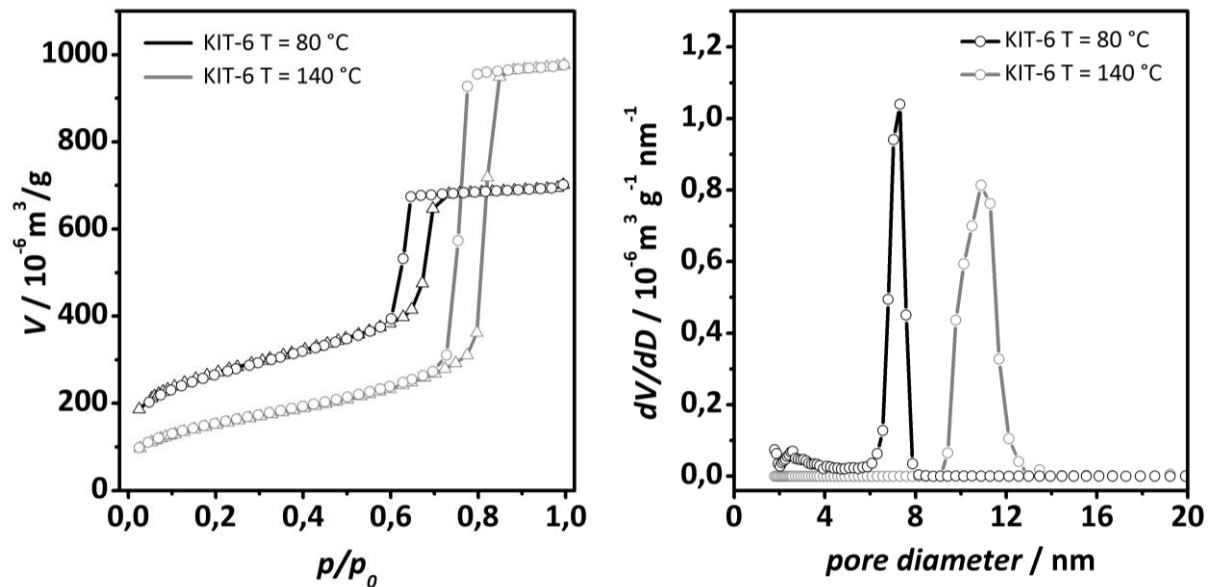


Figure 28. Nitrogen physisorption isotherms of mesoporous KIT-6 synthesized at distinct temperatures (left) and their corresponding pore size distributions (NLDFT model, right).

The average pore wall thickness h was calculated by combining the average pore size D_h with the information obtained from the P-XRD data. For the cubic ($Ia3d$) symmetry the pore wall thickness is given as:^[114]

$$h = a / 2 - D_h \quad (8)$$

where the lattice constant a is calculated from the d_{211} value by

$$a = d_{211} / \sqrt{6} \quad (9)$$

The average pore wall thickness decreases with increasing temperature of hydrothermal treatment. For *KIT-6-80*, h is calculated as 3.2 nm and for *KIT-6-140* as 1.4 nm which is in good agreement with the literature results.^[67, 114] *Table 9* summarizes the results.

	d_{211} [nm]	average pore width D_h (NLDFT) [nm]	average pore wall thickness h [nm]	specific surface area A_{BET} [m ² ·g ⁻¹]	pore volume [cm ³ ·g ⁻¹]
KIT-6-80	8.6	7.3	3.2	920	1.0
KIT-6-140	9.3	10	1.4	534	1.5

Table 9. Overview of the structural data of mesoporous KIT-6 silica with different synthesis temperatures.

5.3 Conversion of In_2O_3 precursor in mesoporous templates

Thermal analysis was carried out to evaluate suitable conditions for a quantitative conversion of In_2O_3 precursor into In_2O_3 and in case of carbon serving as structure matrix additionally to elucidate an appropriate combustion temperature. For this reason, the thermal decomposition of $\text{In}(\text{NO}_3)_3$ in the respective matrices was monitored.

Figure 29 (left) shows the results of TG-MS experiments in mesoporous KIT-6 silica loaded with $\text{In}(\text{NO}_3)_3$.⁶ A mass loss of ca. 46 % is observed in the temperature region between 30 °C and 220 °C which is attributable to the release of water and to the formation of In_2O_3 , confirmed by the detection of characteristic mass fragments. Release of residual water after drying (H_2O^+ , $m/z = 18$) occurs in the temperature interval between 50 and 150 °C. NO^+ and NO_2^+ fragments ($m/z = 30$ and $m/z = 46$, respectively) are detected at temperatures between ca. 120 and 230 °C. This latter instance, *i.e.* the decomposition of $\text{In}(\text{NO}_3)_3$ into In_2O_3 , takes place in two consecutive steps (120 – 180 °C and 180 – 220 °C), a behavior which is also observed for the thermal decomposition of pure $\text{In}(\text{NO}_3)_3 \cdot 5\text{H}_2\text{O}$.^[52]

Similar to the mesoporous KIT-6 silica matrix, the CMK-3 carbon matrix, (Figure 29, right) does not seem to affect significantly the temperature range for the thermal decomposition of indium nitrate (ca. 120 – 220 °C). The only significant difference is that here the decomposition does not take place in two distinct steps, as in case of $\text{In}(\text{NO}_3)_3$ but in one continuous instance. This is obviously due to the presence of carbon which, as a reducing agent with high surface area, is likely to influence the reduction of nitrate into nitric oxides (NO , NO_2); this is confirmed by the detection of small quantities of CO_2 in the respective

⁶ The same results are obtained for SBA-15 serving as structure matrix.

temperature interval. Once this conversion of indium nitrate into indium oxide is completed the oxidation of the carbon matrix sets in, as can be seen by further mass loss accompanied by the evolution of CO_2 (mass fragment with $m/z = 44$). This process extends to a temperature of ca. 620 °C which is a comparably high value for the combustion of mesoporous carbon in the presence of a metal oxide inside the pores (see section 1.2.3).

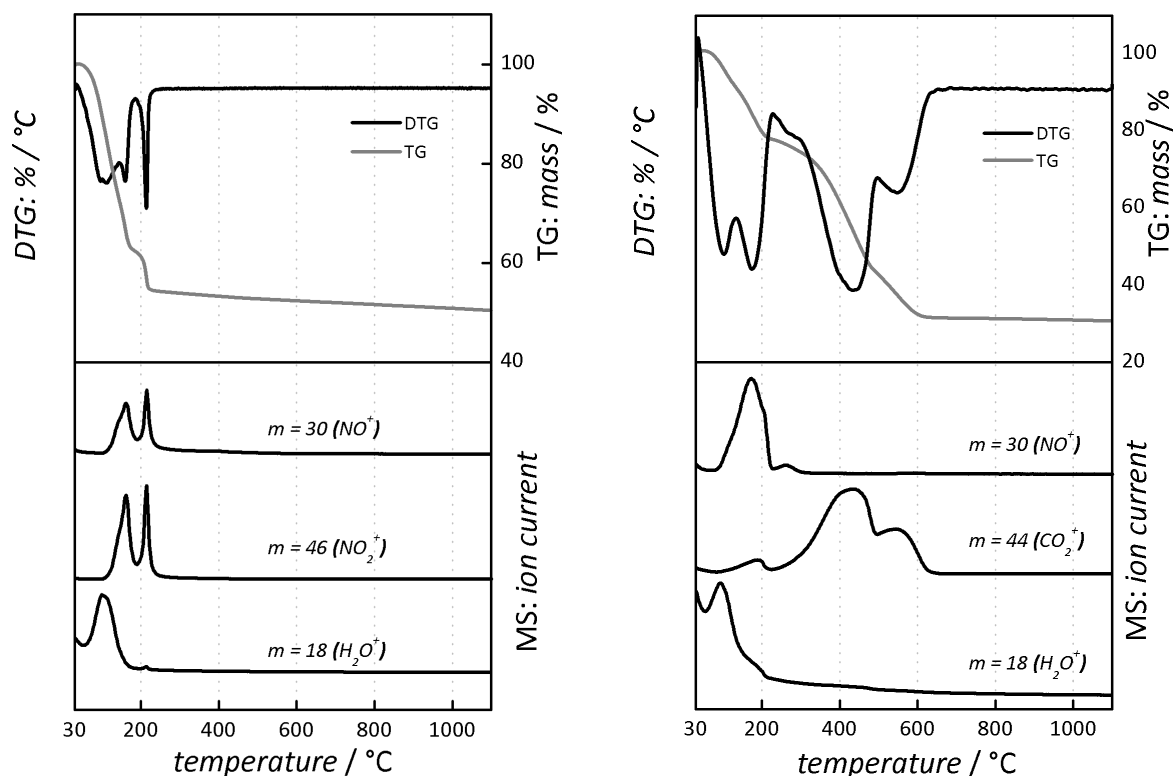


Figure 29. Coupled thermogravimetry (TG) and mass ion detection (MS) for mesoporous KIT-6 silica (left) and CMK-3 carbon (right), both impregnated with $\text{In}(\text{NO}_3)_3$.

5.4 Synthesis and characterization of mesoporous In_2O_3 with silica as template

5.4.1 Synthesis of mesoporous In_2O_3

In a typical synthesis a KIT-6 or SBA-15 silica was impregnated by the incipient wetness technique with a saturated aqueous solution of $\text{In}(\text{NO}_3)_3 \cdot 5\text{H}_2\text{O}$ (99 %, Sigma). After filtration, the sample was dried at ambient temperature, heated under air atmosphere to 300 °C at a constant rate of 2 °C·min⁻¹, and kept at that temperature for two hours to convert indium nitrate quantitatively to indium oxide, according to the results of TG-MS measurements.

This procedure was repeated three times to achieve a sufficient complete pore filling. The silica matrix was finally removed by leaching with a sodium hydroxide solution (2 M) for 4 hours at room temperature. This procedure was repeated twice to ensure a complete silica removal.

5.4.2 Characterization of composite materials

Figure 30 shows the low-angle XRD pattern of a representative series of $\text{In}_2\text{O}_3/\text{SBA-15-80}$ (left) and $\text{In}_2\text{O}_3/\text{KIT-6-80}$ (right) composite materials after one, two, and three cycles of impregnation with $\text{In}(\text{NO}_3)_3$ and subsequent conversion into the oxide. The reflection intensities decreases with every cycle indicating an increased filling of the pores with In_2O_3 , which diminishes the scattering contrast.

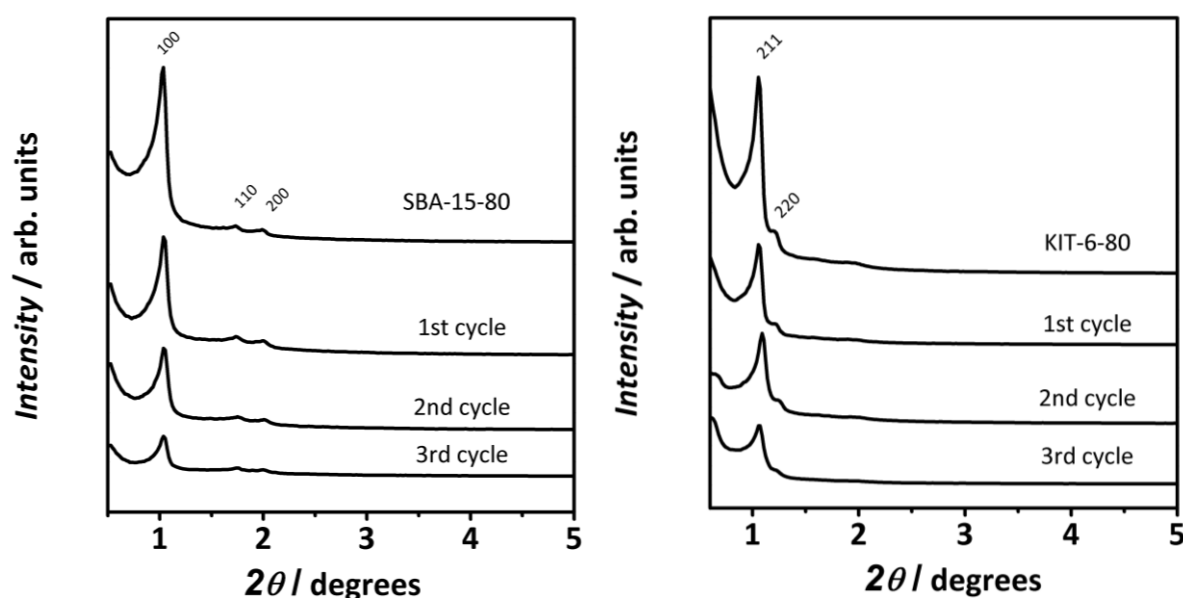


Figure 30. Low-angle P-XRD pattern of mesoporous SBA-15 (left) and KIT-6 (right) and the corresponding In_2O_3 /silica composite materials obtained after several cycles of impregnation and oxide formation.

The filling of the pores with In_2O_3 is further confirmed by the wide-angle diffraction patterns (see Figure 31) indexable as the cubic body-centered bixbyte type crystal structure. The FWHM of the 222 reflection decreases slightly from the first to the second cycle, whereas no significant difference from the second to the third cycle is observed for In_2O_3 in both matrices. With application of the SCHERRER formula (see eq. 7) the average size of the crystalline domains

is 30 nm after the first and 40 nm after the second and third cycle for In_2O_3 in SBA-15. For KIT-6 the size of the crystalline domains is calculated as 25 nm after the first and 30 nm after the second and third cycle. The slight growth of the crystalline domains with progressing cycles indicates that the In_2O_3 particles grow with a certain degree of epitaxial attachment. However, for porous materials the reliability of the SCHERRER method must be regarded as limited.

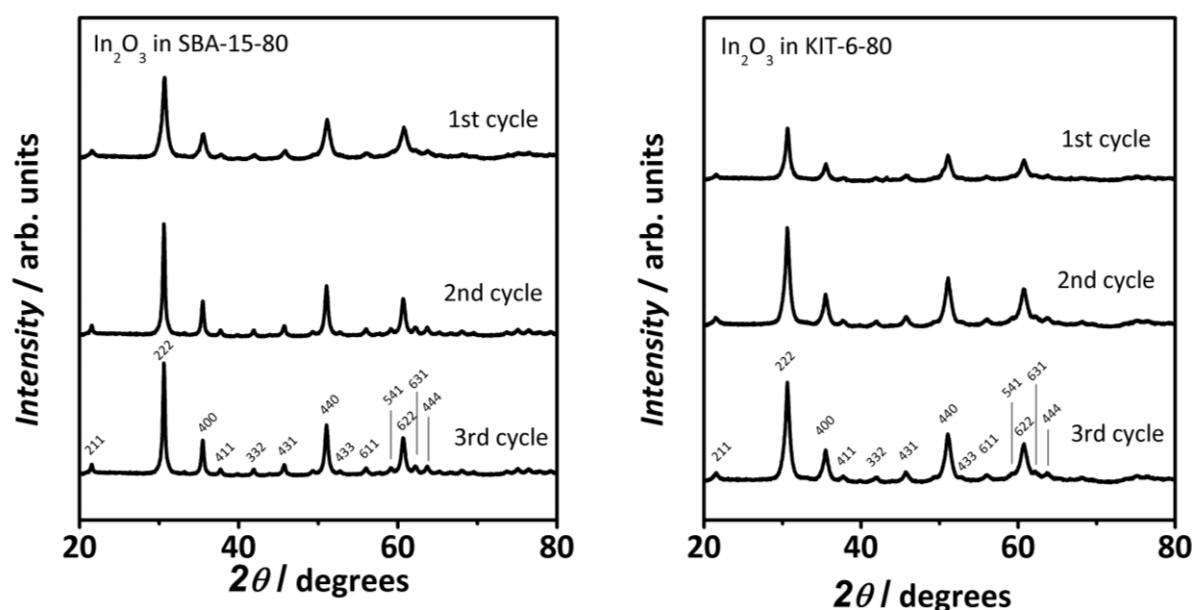


Figure 31. Wide-angle P-XRD pattern of $\text{In}_2\text{O}_3/\text{SBA-15}$ (left) and $\text{In}_2\text{O}_3/\text{KIT-6}$ (right) composite materials obtained after one, two and three cycles of impregnation and conversion into In_2O_3 .

Figure 32 shows the physisorption isotherms (left) of the $\text{In}_2\text{O}_3/\text{SBA-15-80}$ and $\text{In}_2\text{O}_3/\text{KIT-6-80}$ composites (right). All materials show a type IV isotherm with H1 hysteresis. After the second and the third cycle the desorption branch of $\text{In}_2\text{O}_3/\text{SBA-15-80}$ shows a drop in the adsorbed volume in the range of $p/p_0 \approx 0.4-0.5$, which is documented in the literature as the *tensile strength effect* (TSE).^[115] The TSE emerges from the formation of constrictions due to an inhomogeneous filling of the pores, which frequently results in *bottleneck pores*. The constrictions of these pores prevent the evaporation of the liquid phase from the inner of the pore, so that the desorption is shifted to lower p/p_0 values. This feature is not observed for $\text{In}_2\text{O}_3/\text{KIT-6-80}$ presumably due to the improved connectivity of the pore framework, which prevents the creation of such constrictions.

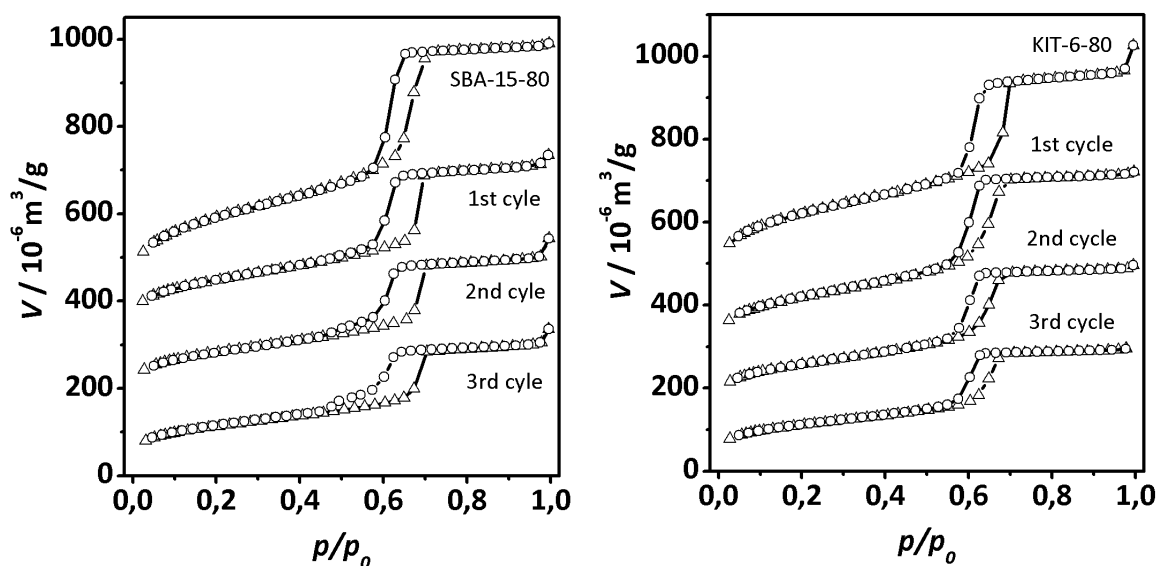


Figure 32. Nitrogen physisorption isotherms of $\text{In}_2\text{O}_3/\text{SBA-15}$ (left) and $\text{In}_2\text{O}_3/\text{KIT-6}$ (right) composite materials obtained after one, two and three cycles of impregnation and conversion into In_2O_3 .

The pore size distributions of the silica template and the composite materials calculated by the NLDFT model are shown in *Figure 33*.

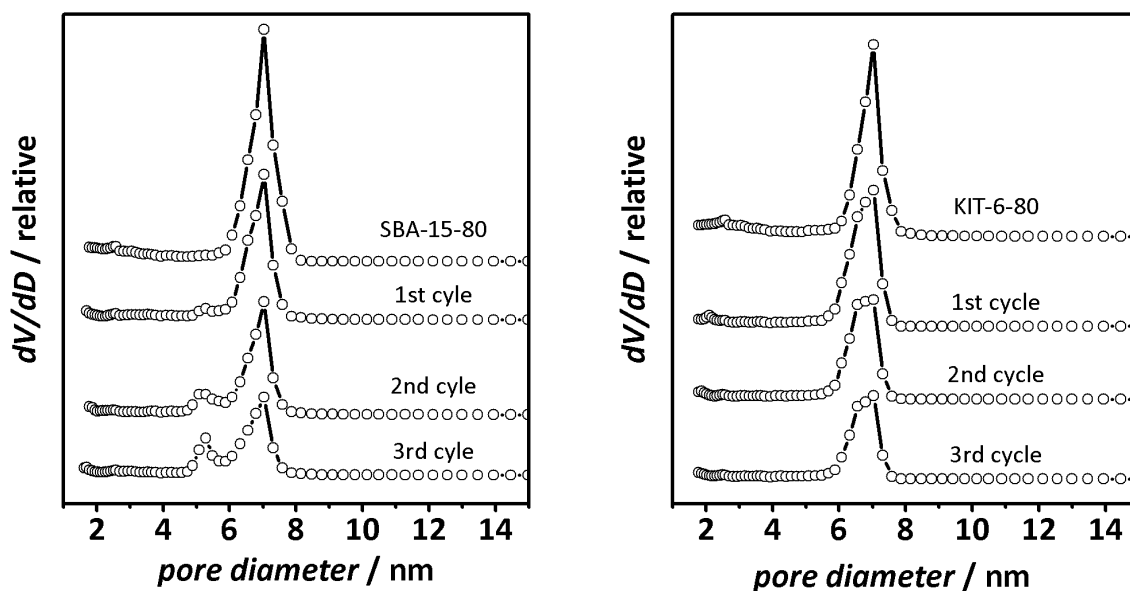


Figure 33. Pore size distributions of $\text{In}_2\text{O}_3/\text{SBA-15}$ (left) and $\text{In}_2\text{O}_3/\text{KIT-6}$ (right) composite materials obtained after one, two and three cycles of impregnation and conversion into In_2O_3 calculated by the NLDFT model.

As expected, the amount of adsorbed nitrogen decreases after each cycle for both materials, confirming a filling of the pores with In_2O_3 , which is also reflected in lower surface areas and pore volumes with progressing cycles (see also *Table 10*). No shift of the peak maximum for both materials ($D_h = 7$ nm) is observed indicating that the growth of In_2O_3 crystals takes place mostly along the pore axis rather than from the pore walls towards the pore center (or vice versa), as already observed for the formation of ZnO in mesoporous CMK-3 (see *section 4.5.1*). The additional peak at 5.3 nm for $\text{In}_2\text{O}_3/\text{SBA-15-80}$ obtained after two and three cycles is caused by the TSE already mentioned (BJH: 3.8 nm).

	$d_{100}/$ d_{211} [nm]	average pore width D_h (NLDFT) [nm]	average pore wall thickness h [nm]	specific surface area A_{BET} [$\text{m}^2 \cdot \text{g}^{-1}$]	pore volume [$\text{cm}^3 \cdot \text{g}^{-1}$]	FWHM_{222} [°]
SBA-15-80	8.5	7.0	2.8	840	0.94	-
1 st cycle	8.5	7.0	2.9	512	0.62	0.30
2 nd cycle	8.5	7.0	2.9	450	0.53	0.22
3 rd cycle	8.4	7.0	2.8	380	0.40	0.22
KIT-6-80	8.4	7.0	3.3	770	0.85	-
1 st cycle	8.4	7.0	3.3	581	0.69	0.33
2 nd cycle	8.2	7.0	3.0	470	0.55	0.30
3 rd cycle	8.1	7.0	2.9	379	0.44	0.29

Table 10. Overview of the structural data of mesoporous *SBA-15-80* and *KIT-6-80* silica and the respective composite materials obtained after one, two and three cycles of impregnation and conversion into In_2O_3 cycles.

Similar results were also obtained for the incorporation of In_2O_3 in mesoporous *SBA-15-140* and *KIT-6-140*, with larger pore diameters of about 10 nm. In these cases no TSE is observed due to the already mentioned improved pore connectivity. An overview of the structural data of these synthesis series is given in *Table 11*.

	$d_{100}/$ d_{211} [nm]	average pore width D_h (NLDFT) [nm]	average pore wall thickness h [nm]	specific surface area A_{BET} [m ² g ⁻¹]	pore volume [cm ³ g ⁻¹]	$FWHM_{222}$ [°]
SBA-15-140	9.4	10.1	0.8	438	1.10	-
1 st cycle	9.4	10.1	0.8	352	0.84	0.22
2 nd cycle	9.6	10.1	1.0	308	0.73	0.20
3 rd cycle	9.7	10.1	1.1	260	0.62	0.20
KIT-6-140	9.3	10.5	0.9	515	1.50	-
1 st cycle	9.4	10.5	1.0	304	0.87	0.28
2 nd cycle	9.3	10.5	0.9	262	0.71	0.25
3 rd cycle	9.3	10.5	0.9	207	0.57	0.25

Table 11. Overview of the structural data of mesoporous *SBA-15-140* and *KIT-6-140* silica and the respective composite materials obtained after one, two and three cycles of impregnation and conversion into In_2O_3 cycles.

5.4.3 Characterization of mesoporous In_2O_3

5.4.3.1 Characterization of mesoporous In_2O_3 with SBA-15 as template

The P-XRD pattern of hexagonal mesoporous In_2O_3 obtained after three cycles is shown in *Figure 34*. The low-angle pattern (left) reveals one intensive and two less intensive peaks for both materials which can be indexed according to the parental $p6mm$ structures of the silica matrices (100, 110, 200). The well resolved 110 and 200 reflections indicate long-range structural order of the obtained materials. The d_{100} -spacing of the replicated In_2O_3 materials are in good agreement with the values of their structure matrices (see *Table 12*), confirming that the replication procedure occurs without significant change in the unit cell size.

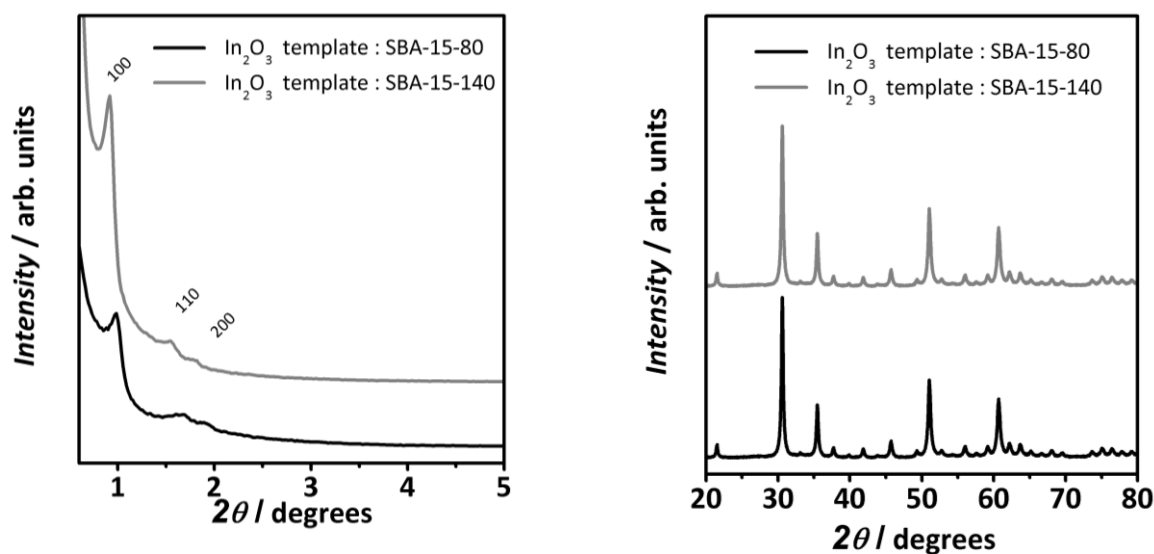


Figure 34. Low-angle P-XRD pattern of mesoporous In_2O_3 synthesized with SBA-15-80 and SBA-15-140 as template (left) and the corresponding wide-angle P-XRD pattern (right).

The long-range mesoscopic order is also confirmed by TEM analysis. Figure 35 displays representative images of each sample, viewed perpendicular to the pore axis.

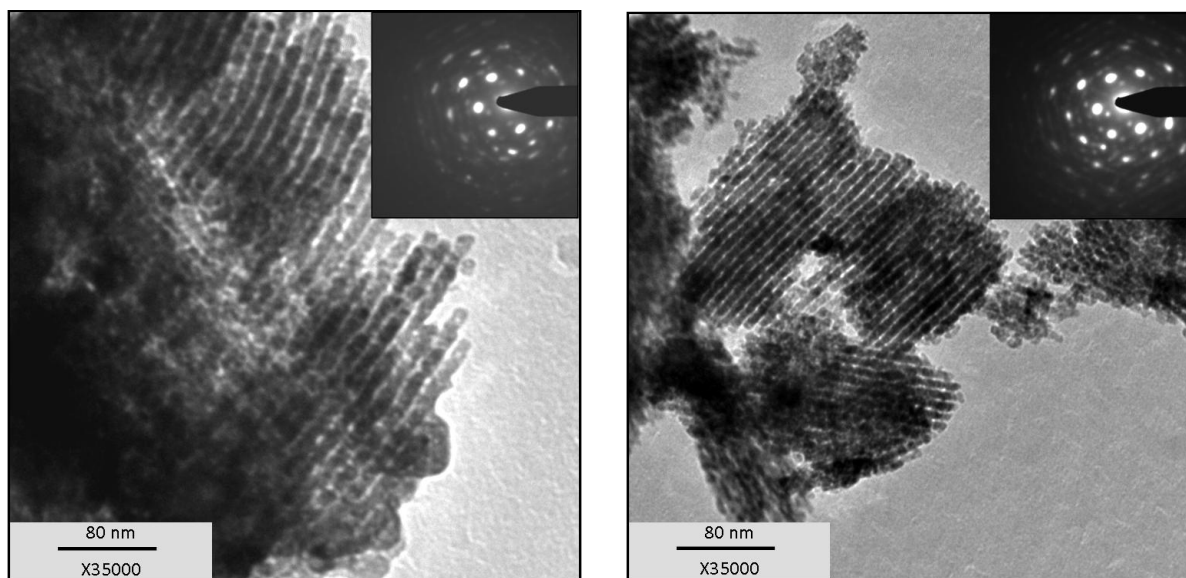


Figure 35. TEM images and the corresponding SAED pattern (inset) of mesoporous hexagonal In_2O_3 with SBA-15-80 (left) and SBA-15-140 (right) as templates.

The P-XRD wide-angle region (see Figure 34, right) confirms the presence of crystalline In_2O_3 (bixbyite) which was also observed for the composite materials (see Figure 31, left); the size of the crystalline domains does not substantially differ from that of the composite material

obtained after three cycles (ca. 40 nm). For In_2O_3 replicated from *SBA-15-80* as well as from *SBA-140* the average size of the crystalline domains are 39 and 43 nm, respectively (SCHERRER). Hence, the domains extend over several repeat distances of the mesoscopic lattice parameter, which is 10.3 and 11.1 nm, respectively. The crystalline nature of the materials was further verified by electron diffraction experiments. The insets of *Figure 35* show the SAED patterns of the corresponding TEM image areas. The patterns, consisting of distinct spots, confirm the presence of large single crystalline domains. EDX analysis verifies that the silica template is nearly completely removed after stirring the samples twice in 2 M NaOH solution, each for four hours. The average In : Si atomic ratio was then determined as 95 : 5.

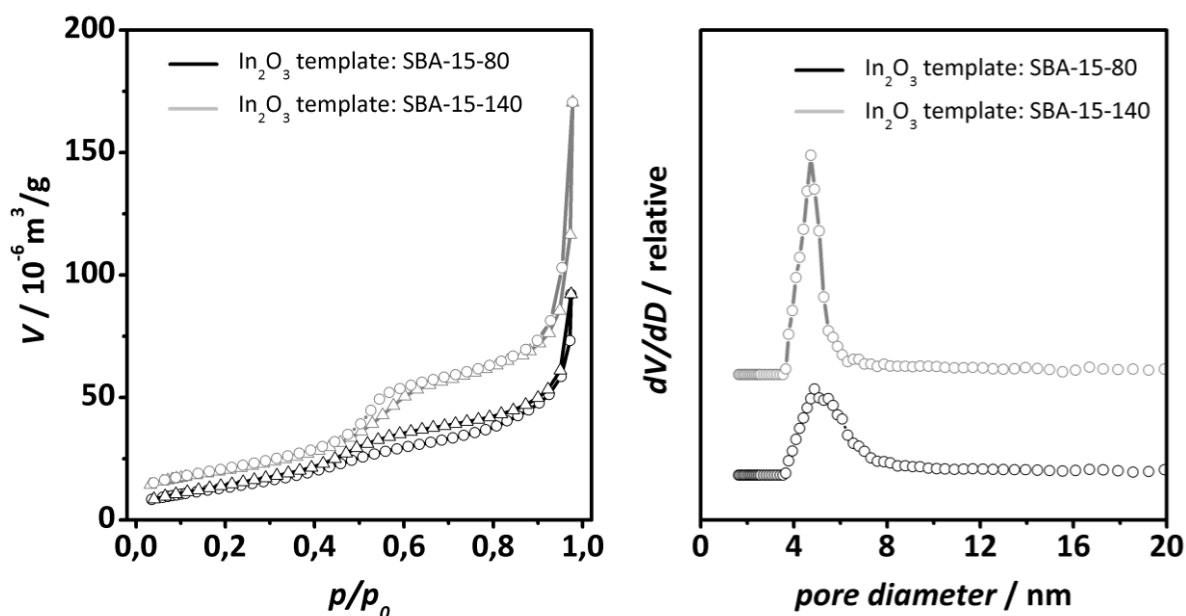


Figure 36. Nitrogen physisorption isotherms (left) and the corresponding pore size distribution (NLDFT) of mesoporous hexagonal In_2O_3 , synthesized using *SBA-15-80* and *SBA-15-140* as template (right).

Nitrogen physisorption measurements are displayed in *Figure 36*. Both In_2O_3 replicas reveal type IV isotherms with weak hysteresis (left). The corresponding pore size distribution calculated by the NLDFT model (right), exhibit an average pore size of 5.6 nm for both materials. The average pore wall thickness of In_2O_3 synthesized with *SBA-15-140* as template is 5.5 nm and for In_2O_3 synthesized with *SBA-15-80* it is 4.7 nm, which is smaller than the pore sizes ($D_h = 10.1$ and 7.0 nm) of the respective structure matrices. This observation indicates that the pores are not entirely filled with the metal oxide. Anyway, a complete pore filling with In_2O_3 from one side of the pore wall to the other is *a priori* unlikely due to a shrinkage of

the material inside the pore during the oxide formation (caused by evaporation of residual solvent and/or nitrate decomposition). Further details concerning the formation mechanism are subject of *section 5.4.4* and *5.4.5*).

The specific surface area for In_2O_3 replicated from the template with smaller pores is $60 \text{ m}^2\cdot\text{g}^{-1}$ and $73 \text{ m}^2\cdot\text{g}^{-1}$ for In_2O_3 replicated from larger pores. Usually, the specific surface areas of metal oxides replicated from matrices with smaller pores are larger than those replicated from matrices with larger pores with the same mesostructure, which is not the case here.^[114] This may originate from an increased creation of bulk material during the synthesis. Comparing the BET values with those of the structure matrices, the specific surface areas of the In_2O_3 samples are substantially lower than those of the parent silica matrices (see *Table 12*), which may be attributable to the lower structural order in some degree. However, lower BET surface areas are to be expected anyway, since: (i) The In_2O_3 replicas possess generally thicker pore walls and smaller pore widths than the respective silica samples and, thus, *a priori* a lower surface-to-volume ratio. (ii) Crystalline In_2O_3 is likely to exhibit a lower surface roughness than amorphous silica. (iii) A substantial fraction of the surface area in the silica samples (especially those which were synthesized at 80°C) originates from microporosity which is absent in the In_2O_3 samples. (iv) The densities of the two materials are different (in the bulk phase $7.2 \text{ g}\cdot\text{cm}^{-3}$ for In_2O_3 and about $2.2 \text{ g}\cdot\text{cm}^{-3}$ for amorphous SiO_2), this latter aspect probably being the most significant one.

	d_{100} [nm]	average pore width D_h (NLDFT) [nm]	average pore wall thickness h [nm]	specific surface area A_{BET} [$\text{m}^2\cdot\text{g}^{-1}$]	pore volume [$\text{cm}^3\cdot\text{g}^{-1}$]	FWHM_{222} [°]
(SBA-15-80)	8.5	7.0	2.8	840	0.94	-
In_2O_3 replica	8.9	5.6	4.7	60	0.16	0.22
(SBA-15-140)	9.4	10.1	0.8	438	1.10	-
In_2O_3 replica	9.6	5.6	5.5	73	0.26	0.20

Table 12. Overview of the structural data of mesoporous hexagonal In_2O_3 materials and their parental structure matrices *SBA-15-80* and *SBA-15-140*.

5.4.3.2 Characterization of mesoporous In_2O_3 with KIT-6 as template

Figure 37 (left) shows the low-angle P-XRD pattern of mesoporous In_2O_3 obtained after three cycles of impregnation and oxide formation with *KIT-6-80* and *KIT-6-140* as the template. Both materials exhibit one intensive (211) and three less intensive peaks (220, 420, 332) which can be indexed according to the cubic $1a3d$ structure of the parental templates.

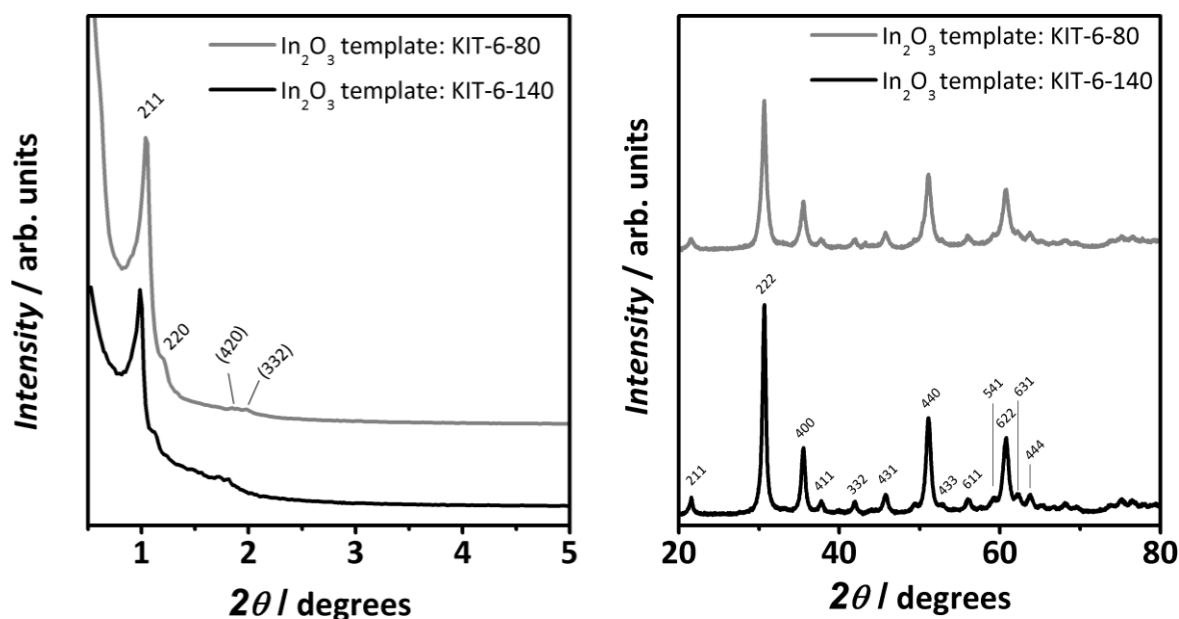


Figure 37. Low-angle P-XRD pattern of mesoporous In_2O_3 synthesized with *KIT-6-80* and *KIT-6-140* as template (left) and the corresponding wide-angle P-XRD pattern (right).

The presence of the latter reflections indicates a long-range order of the mesostructure, also confirmed by TEM analysis. Figure 38 shows representative TEM images of In_2O_3 replicated from small- (left) and large- (right) pore KIT-6 silica, which display the long mesoscopic order as well as the tortuosity of the pore systems. A comparison of the In_2O_3 d_{211} -spacing values reveals a good compliance with the values calculated for the structure matrices, confirming that the replication procedure occurs without significant changes in the size of the mesostructure (see Table 13), as also observed for mesoporous In_2O_3 replicated from SBA-15 silica. The wide-angle P-XRD patterns (Figure 37, right) show the same signature as for the composite materials (see Figure 31, right), confirming the presence of crystalline In_2O_3 (cubic bixbyite-type) even after the template removal with NaOH. The average size of the crystalline domains was calculated as 30 nm and 35 nm for In_2O_3 replicated from *KIT-6-80* and

KIT-6-140 respectively, which extend over several repeat distances of the mesopores. A comparison with the hexagonal In_2O_3 materials shows a similar trend concerning the relation between the crystalline domain size and the pore size/interconnectivity. The domain size becomes apparently larger with increasing pore size/interconnectivity, which suggests that the formation of the single crystalline domains is less hindered in case of large pore templates; however, for porous materials the reliability of the SCHERRER method must be regarded as limited. The crystallinity of the material was additionally investigated by electron diffraction experiments. Insets of *Figure 38* show the corresponding SAED pattern with distinct spots, confirming the existence of large single-crystalline domains. EDX analysis of the sample conducted on several spots reveal that the average In : Si atomic ratio was 90 : 10 after NaOH treatment of four hours, and 98 : 2 for a further NaOH treatment for another four hours.

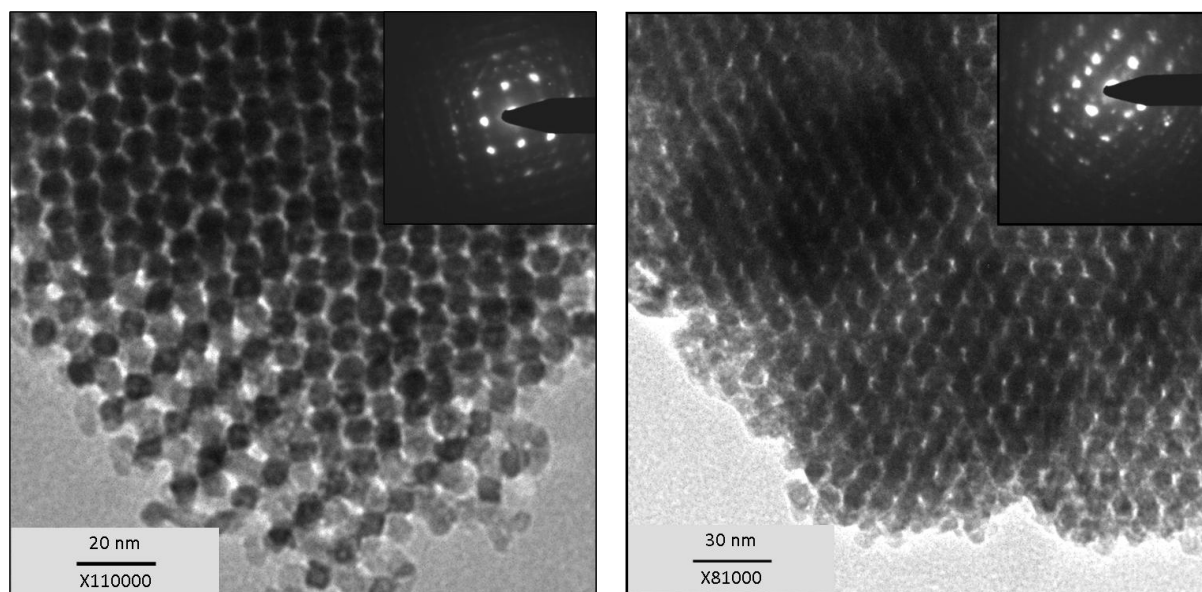


Figure 38. TEM images and the corresponding SAED pattern (inset) of mesoporous cubic In_2O_3 with *KIT-6-80* (left) and *KIT-6-140* (right) as templates.

The data of the physisorption measurements are displayed in *Figure 39*. Both In_2O_3 replicas reveal type IV isotherms with H2 hysteresis implying the presence of slit-pores (left) as expected for materials replicated from KIT-6 silica. The corresponding pore size distributions calculated by the NLDFT model (right) reveal an average pore size of 6.5 nm for mesoporous In_2O_3 replicated from *KIT-6-80* and 5.4 nm for the replica of *KIT-6-140*.

The average pore wall thickness of In_2O_3 synthesized with *KIT-6-140* as template is determined as 5.9 nm which is lower (3.9 nm) for In_2O_3 with *KIT-6-80* serving as structure matrix.

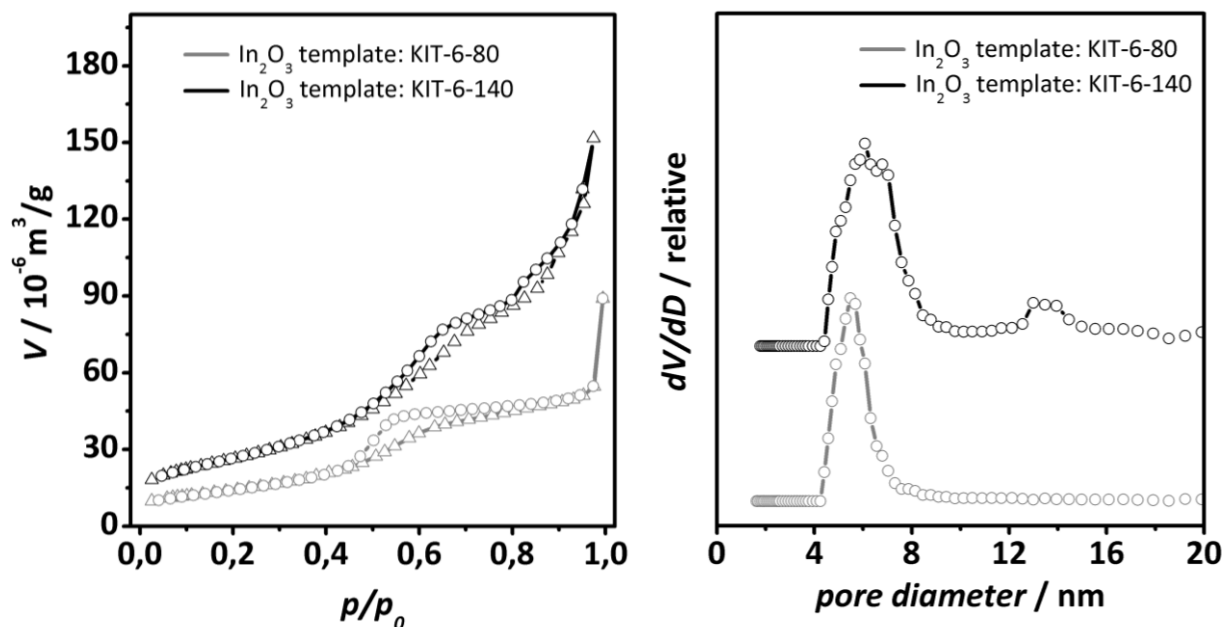


Figure 39. Nitrogen physisorption isotherms (left) and the corresponding pore size distribution (NLDFT) of mesoporous cubic In_2O_3 synthesized using *KIT-6-80* and *KIT-6-140* as template.

In case of a perfect replication procedure, the pore size of the silica template should match with the pore wall thickness of the replica and the wall thickness of the silica template should correspond to the pore size of the In_2O_3 replica. However, such consistencies can not be observed here. Instead, the pore sizes of the In_2O_3 replicas are somewhat larger than the pore wall thickness of the template and the wall thicknesses of the In_2O_3 replicas are somewhat smaller than the pore size of the silica template (see *Table 13*). The analysis is simple, when one takes into account that the d_{211} values are nearly constant for all materials, the respective structural differences can only be explained by an incomplete pore filling of the silica matrix with In_2O_3 from one side of the pore wall to the other. However an incomplete pore filling is expected anyway which is caused by a volume shrinkage of the material inside the pore primarily due to density differences between $\text{In}(\text{NO}_3)_3 \cdot 5\text{H}_2\text{O}$ and In_2O_3 with $\rho = 2.4 \pm 0.2 \text{ g cm}^{-3}$ and $\rho = 7.2 \text{ g cm}^{-3}$, respectively. An overview of the structural data of the respective metal oxides is given in *Table 13*.

	d_{211} [nm]	average pore width D_h (NLDFT) [nm]	average pore wall thickness h [nm]	specific surface area A_{BET} [m ² ·g ⁻¹]	pore volume [cm ³ ·g ⁻¹]	$FWHM_{222}$ [°]
(KIT-6-80)	8.4	7.0	3.3	770	0.85	-
In ₂ O ₃ replica	8.5	6.5	3.9	95	0.28	0.29
(KIT-6-140)	9.3	10.5	0.9	515	1.50	
In ₂ O ₃ replica	9.2	5.4	5.9	67	0.21	0.25

Table 13. Overview of the structural data of mesoporous In₂O₃ materials and their structure matrices KIT-6-80 and KIT-6-140.

5.4.4 Investigations on growth and morphology of In₂O₃ particles in KIT-6

Aim of this study was the investigation on growth and morphology of In₂O₃ particles in a mesoporous KIT-6-80 silica matrix. For this reason SEM studies of In₂O₃ products after each cycle of impregnation and oxide formation and subsequent template removal were carried out in addition to P-XRD and nitrogen physisorption measurements. Figure 40 (left) shows the low-angle P-XRD pattern of In₂O₃ products obtained after one, two and three cycles of impregnation.

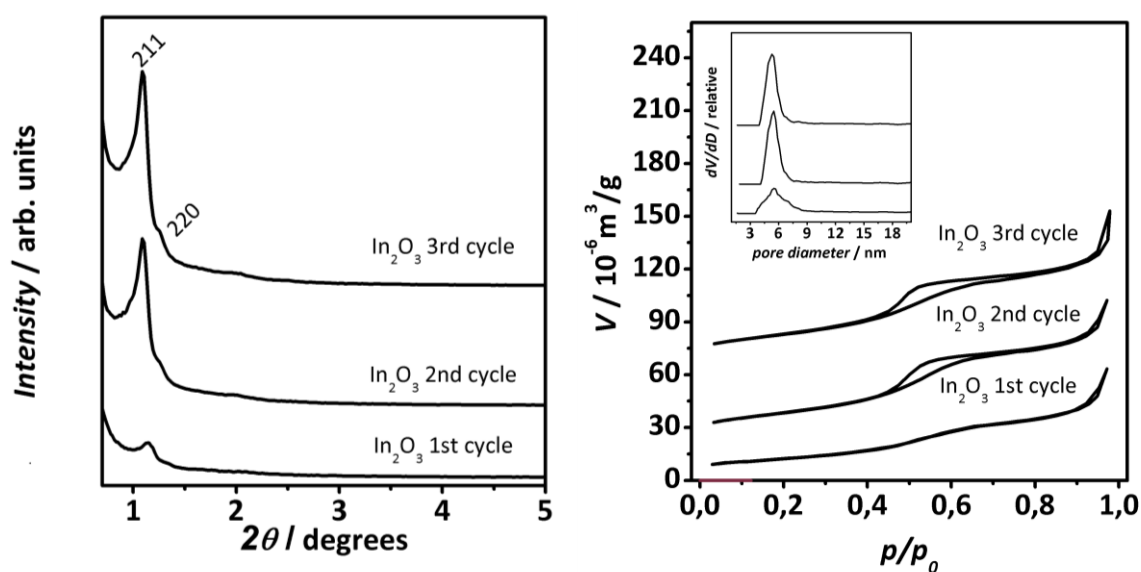


Figure 40. Low-angle P-XRD pattern of silica-free mesoporous In₂O₃ materials obtained after one, two and three cycles of impregnation and oxide formation (left). Right, the corresponding nitrogen physisorption isotherms and pore size distributions of the materials (inset).

Already after the first cycle a mesostructured material is obtained confirmed by the weak reflection at $2\theta = 1.14$ (which can be indexed as 211, assuming the cubic $Ia\bar{3}d$ symmetry). The absence of further reflections indicates that the structural long-range order is quite low. However, additional reflections can be observed as a weak shoulder after a second and third cycle, one of which can be indexed as 220; the overall intensity of all low-angle reflections increases and the peaks become narrower after each cycle, indicating larger coherent mesostructural scattering domains after each additional cycle. The data of the nitrogen physisorption measurements are displayed in *Figure 40* (right). All isotherms reveal a type IV characteristic with a small hysteresis not obtained for In_2O_3 after the first cycle suggesting a low porosity of the material. The structural data of the materials and the respective composites are listed in *Table 14*.

	$d_{211}/$ [nm]	average pore width D_h (NLDFT) [nm]	average pore wall thickness h [nm]	specific surface area A_{BET} [m ² ·g ⁻¹]	pore volume [cm ³ ·g ⁻¹]
(KIT-6-80)	8.1	7.0	2.9	690	0.80
1 cycle	8.3	7.0	3.1	480	0.61
In_2O_3 1 st cycle	7.8	5.6	4.0	85	0.25
2 cycles	8.1	6.9	3.0	375	0.42
In_2O_3 2 nd cycle	8.1	5.6	4.3	80	0.22
3 cycles	8.2	6.9	3.1	150	0.31
In_2O_3 3 rd cycle	8.1	5.4	4.4	80	0.23

Table 14. Structural data of mesoporous KIT-6, composite materials after one, two and three cycles of impregnation and oxide formation and the respective silica-free In_2O_3 products.

The materials obtained after each cycle do not differ substantially in pore diameters (5.4 ... 5.6 nm) and pore wall thicknesses (4.0 ... 4.4 nm), allowing conclusions regarding the growth direction of In_2O_3 . As depicted in *Figure 41*, three directions of growth are generally conceivable, namely parallel to the pore axis (a) or perpendicular to the axis (starting from the center, b, or from the pore walls, c).

Because of almost constant values obtained for pore sizes and wall thicknesses in the composites (see *Table 14*) as well as in the products, it becomes apparent that the growth of In_2O_3 occurs predominantly along the pore axis (a) with ca. 40 % pore volume remaining unfilled in the respective region, presumably caused by shrinkage of the precursor compound during oxide formation. In case of the other two possible growth directions (b) and (c), a pronounced shift of the pore diameters and wall thicknesses would be expected. It can be concluded as a preliminary result that at any given position in the silica matrix a pore is filled with In_2O_3 almost entirely (*i.e.* from wall to wall) or not at all.

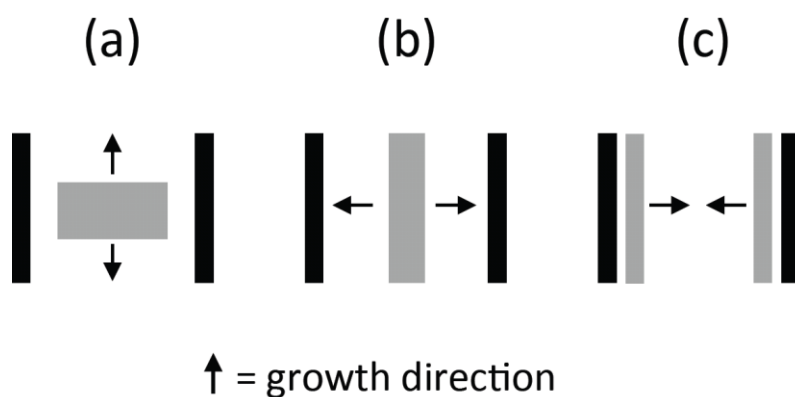


Figure 41. Schematic drawing of potential growth directions of mesoporous In_2O_3 inside the pores of the structure matrix.

For a more detailed elucidation of In_2O_3 particles' growth in KIT-6 matrix, a SEM study of the corresponding silica free In_2O_3 materials after each cycle was carried out. *Figure 42* shows representative SEM images of mesoporous KIT-6 silica (a) and the resulting silica-free In_2O_3 products yielded after the first (b), second (c) and third (d) cycle. For the In_2O_3 particles the resolution of the images is sufficient to show the nanometer-scaled periodicity of the mesopore systems at the particles' outer surfaces (insets). The In_2O_3 samples exhibit nearly spherical particles and fairly uniform particle sizes (around 200 ... 300 nm), especially after the second and third cycle of impregnation and conversion into the oxide. This observation is particularly remarkable due to the fact that the KIT-6 silica particles are irregular in shape and larger than the In_2O_3 particles by approximately one order of magnitude ($3.3 \pm 2.5 \mu\text{m}$ in length and $2.2 \pm 1.7 \mu\text{m}$ in width; mean values \pm standard deviations).

The average size of the nearly spherical In_2O_3 replica particles, on the other hand, increases after each cycle from 217 ± 60 nm (after the first cycle), over 317 ± 130 nm (after the second cycle), to 363 ± 111 nm (after the third cycle). These values were obtained by measuring the diameter of about 200 particles for each sample.

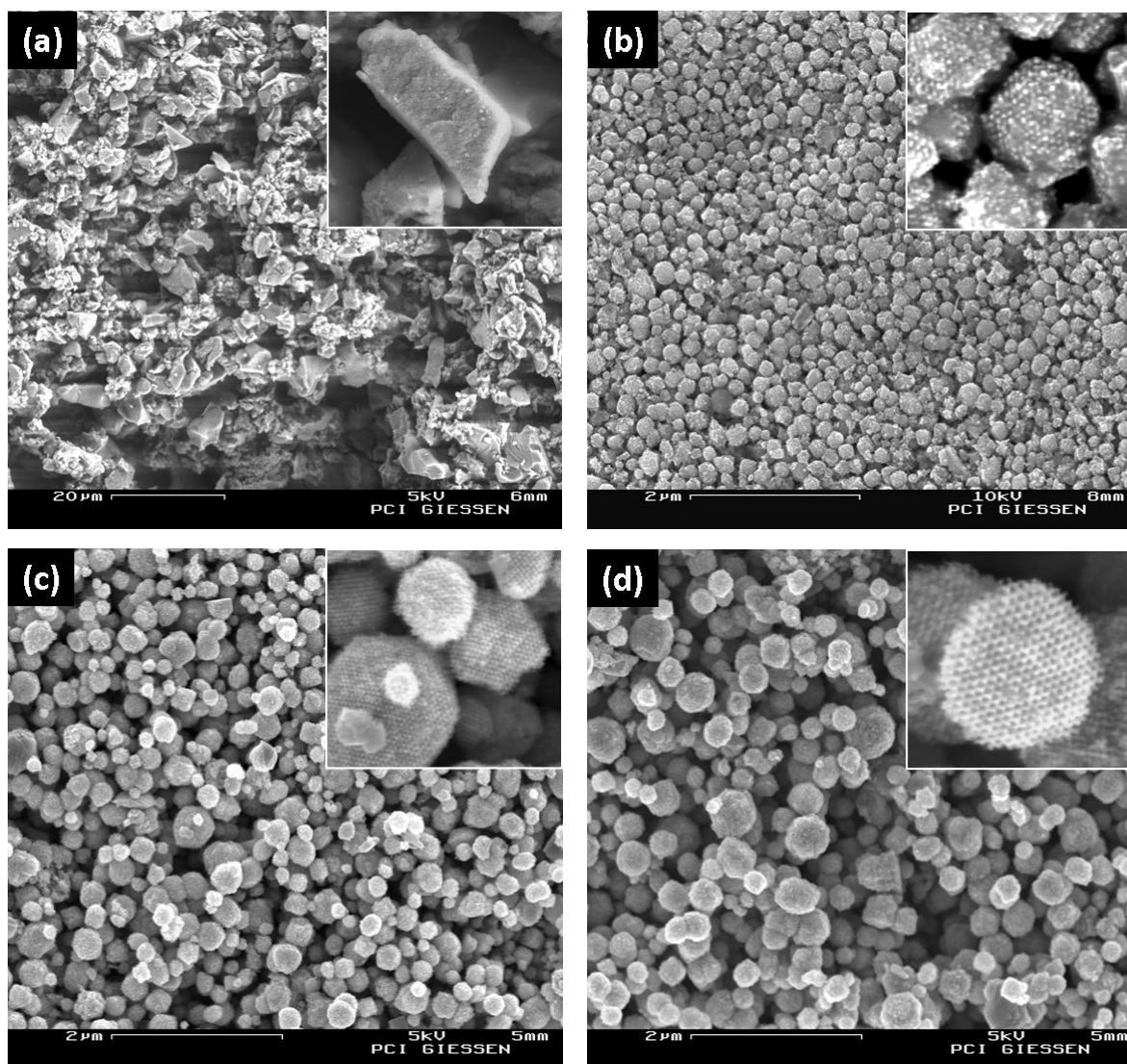


Figure 42. Representative SEM images of KIT-6 silica (a) and mesoporous In_2O_3 materials obtained after template removal of each cycle. Insets show close-up view of selected particles of the sample.

The corresponding particle size distributions are plotted as bar diagrams in *Figure 43*; the curves represent log-normal distributions, fitted by a least-square procedure.

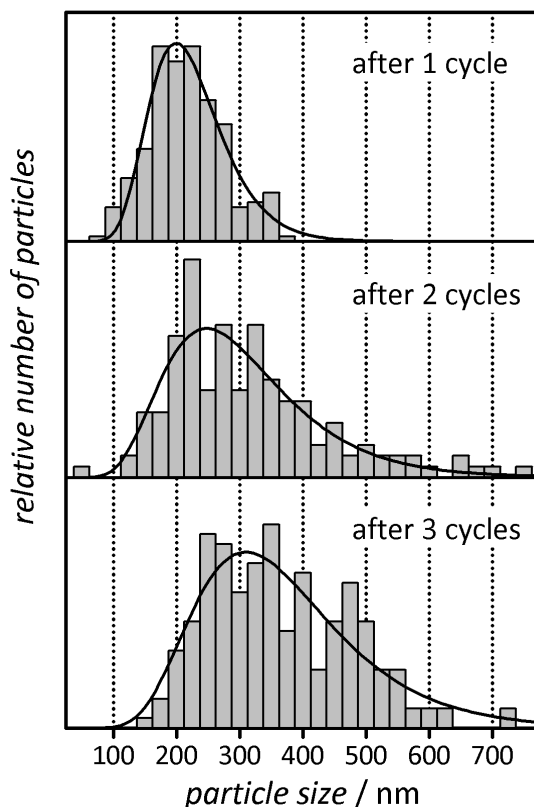


Figure 43. Particle size distribution of mesoporous In_2O_3 obtained after consecutive cycles of impregnation and oxide formation.

Apart from the shift of the distribution peaks towards larger particle sizes, it can be observed that the onsets of the distribution curves also shift while the relative fraction of very large particles (with diameters of 350 to 800 nm) increases. These observations clearly indicate that each new cycle causes the growth of already existing In_2O_3 particles, rather than leading to the formation of new particles. These findings, together with the above-made observation that the KIT-6 silica particles are substantially larger than the In_2O_3 replica particles, show that in substantial fractions of the silica particles the pores do not get filled with In_2O_3 at all, while the pores in other regions seem to get filled completely. A scheme of the growth of In_2O_3 particles inside the pores is depicted in *Figure 44*.

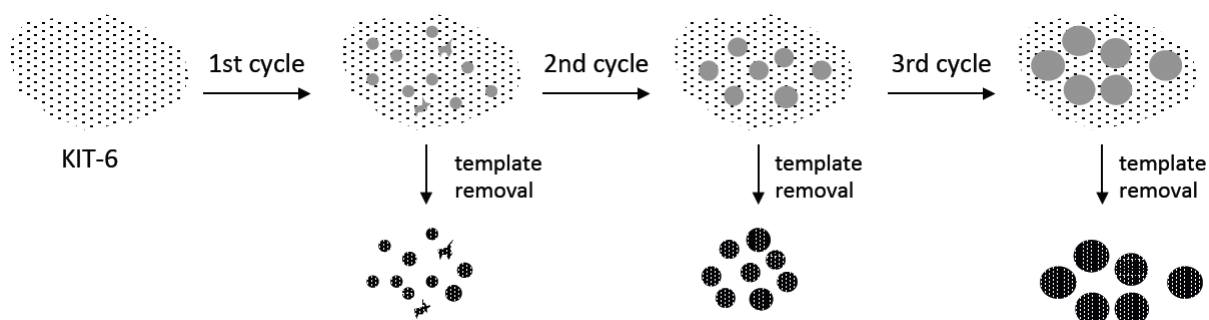


Figure 44. Schematic drawing of the growth of In_2O_3 particles inside the pores of KIT-6 silica: after the first cycle spherical 'islands' are formed inside the silica pore network; additional cycles lead predominantly to the growth of existing In_2O_3 particles rather than to nucleation of new ones.

The spherical shape of the In_2O_3 particles can only be explained by the formation of 'islands' of material within the silica pores, which are assumed to be initially filled with $\text{In}(\text{NO}_3)_3$ solution entirely. The formation of islands, obviously caused by surface minimization as the driving force, thus requires substantial mass transport which can only take place in the liquid state. This liquid-phase-based mass transport may occur either before complete removal of the solvent (water) of the $\text{In}(\text{NO}_3)_3$ solution, or afterwards, taking into account that the melting point of $\text{In}(\text{NO}_3)_3$ is lower (*ca.* 100 °C) than the temperature required for the conversion into In_2O_3 . Thus, either the nitrate solution or nitrate in the molten phase forms droplets inside the pores of the silica; these droplets are larger than the repeat distance of the silica pore system by one to two orders of magnitude. The formation of such spherical droplets is facilitated by the high pore interconnectivity present in the KIT-6 silica sample. With each additional impregnation and conversion into the oxide cycle the liquid-phase mass transport leads to attachment of precursor species to the surface of already existing In_2O_3 particles rather than to nucleation of new droplets; this is consistent with the surface minimization as a driving force.

5.4.5 Investigations on the morphology of In_2O_3 particles in SBA-15

Apart from the elucidation of the growth process of crystalline In_2O_3 in mesoporous silica the particle morphology of the resulting replicated material also represents an interesting object of research. In this regard, parameters like pore size, interconnectivity as well as symmetry of the pore system seem to have an impact on the resulting morphology of the replicated

mesoporous particles. Additionally to the preceding formation study for KIT-6 silica, SEM investigations on mesoporous In_2O_3 with hexagonal pore symmetry replicated from *SBA-15-80* and *SBA-15-140* were carried out in order to analyze this influence.

Figure 45 shows the SEM images of *SBA-15-80* (a) and *SBA-15-140* (b) as well as of the respective silica-free In_2O_3 replicas obtained after three cycles of impregnation and conversion into the oxide (c, d).

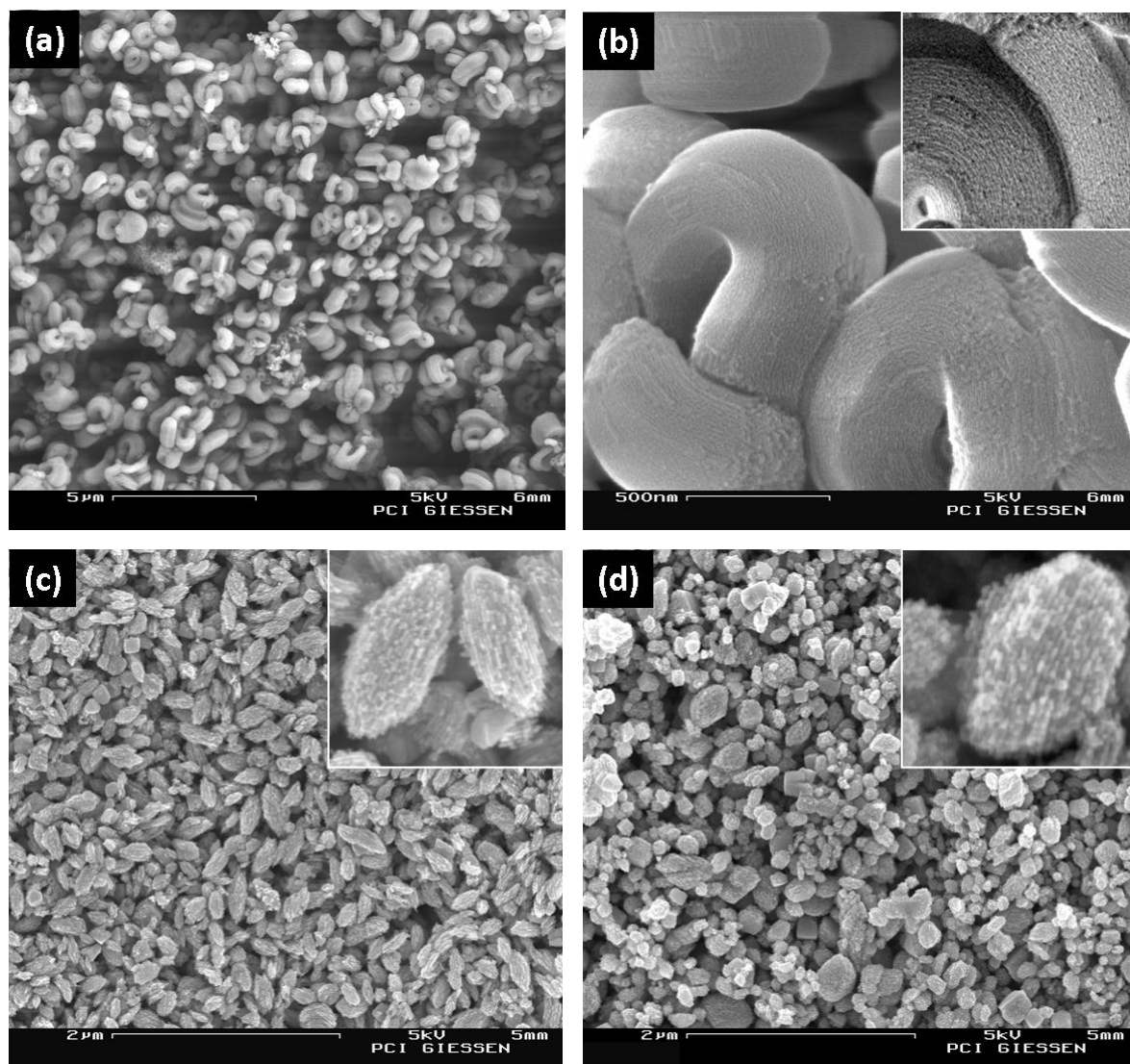


Figure 45. Representative SEM images of mesoporous *SBA-15-80* silica (a) and *SBA-15-140* silica (b), as well as of mesoporous In_2O_3 materials replicated from the two silica materials after three cycles of impregnation and oxide formation (c, d). Insets show close-up views of selected particles of each sample.

Both In_2O_3 replicas show a clearly different shape than the spherical ones originating from the KIT-6 silica matrix (see section 5.4.4). The particles here show an elongated, ellipsoidal shape with an aspect ratio of ca. 1 : 2 (284 ± 70 nm in length and 141 ± 32 nm in width) for

the sample replicated from *SBA-15-80* and 1 : 1.25 (218 ± 90 nm in length and 170 ± 64 nm in width) for the sample replicated from *SBA-15-140*. This is consistent with the substantially lower degree of interconnections between adjacent, parallel mesopores in the SBA-15 silica materials. Instead of spherical droplets (as in case of the 3-D interconnected pores in KIT-6 silica) only droplets with a preferred orientation along the pore axes are possible which results in ellipsoidal In_2O_3 particles. The effect is less pronounced for *SBA-15-140* since here the degree of pore interconnectivity is not as low as for *SBA-15-80*. These results confirm the growth model introduced above for the KIT-6 silica matrix. Interestingly, both SBA-15 silica materials show a fairly well-defined, yet peculiar particle morphology of their own. The particles appear rod-like with an aspect ratio of ca. 1 : 4, but with a strong curvature of ca. 180° . This curvature also applies to the mesopore axes, as can be distinguished in *Figure 45* (b) which shows sufficient resolution to visualize the nano-scale porosity. The SBA-15 particle sizes are in the approximate region of 1 - 2 μm in length and 0.5 μm in width which, as in case of KIT-6 silica, is larger than the size of the In_2O_3 replica particles by approximately one order of magnitude. This means that, similar to the situation found for KIT-6 silica, the particle morphology of In_2O_3 replicas obtained from SBA-15 silica is well-defined (ellipsoidal) with no relation to the morphology of the silica particles, even though the latter (contrary to KIT-6 silica) show a well-defined morphology of their own. Hence, a similar growth model for In_2O_3 inside the pores of SBA-15 silica materials can be deduced which is depicted in *Figure 46*.

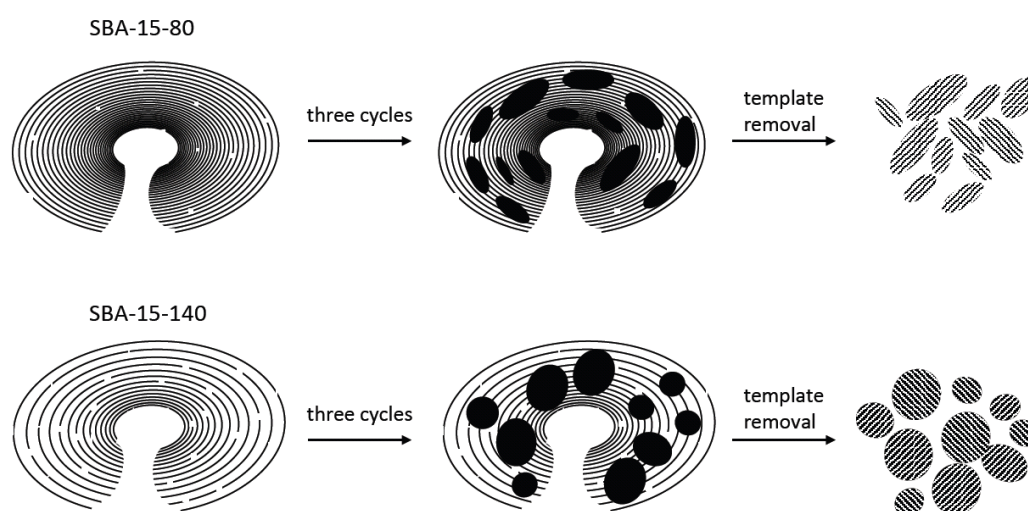


Figure 46. Schematic drawing of the growth of In_2O_3 particles inside the pores of mesoporous SBA-15 silica with distinct pore interconnectivity.

The structural data of the considered materials are summarized in *Table 15*.

	d_{100} [nm]	average pore width D_h (NLDFT) [nm]	average pore wall thickness h [nm]	specific surface area A_{BET} [m ² ·g ⁻¹]	pore volume [cm ³ ·g ⁻¹]
(SBA-15-80)	8.5	7.0	2.8	840	0.94
In ₂ O ₃ replica	8.9	5.6	4.7	60	0.16
(SBA-15-140)	9.4	10.1	0.8	438	1.10
In ₂ O ₃ replica	9.6	4.6	6.5	73	0.26

Table 15. Structural parameters from P-XRD and nitrogen physisorption data for *SBA-15-80* and *SBA-15-140*, as well as for the respective mesoporous silica-free In₂O₃ replicas obtained after three cycles.

5.4.6 Temperature stability of mesoporous In₂O₃

For applications like catalysis and gas sensing (see below) it is mandatory that mesoporous materials are temperature-stable to a certain degree. Given the fact that the operation temperature of semiconducting gas sensor devices range from room temperature to several hundred degrees Celsius, any porous material must withstand these thermal conditions without substantial loss in porosity. For sensors prepared by the conventional sol-gel method this is often not the case as discussed in *section 1.2.1*.

To investigate the thermal stability, samples of mesoporous In₂O₃ were placed in a furnace at various temperatures between 250 °C and 650 °C for four hours with a heating rate of 10 °C·min⁻¹ under air atmosphere, followed by cooling to room temperature. For each temperature a fresh (*i.e.* previously non-heated) sample was chosen.

Figure 47 shows the low-angle P-XRD patterns (left) and nitrogen physisorption measurements (right) of the materials as prepared and after the thermal treatment. The P-XRD signature and the physisorption isotherm shape remain mostly the same at temperatures up to 450 °C, which confirms that no significant loss in mesostructural order or porosity takes place.

Within this temperature interval the specific BET surface area decreases by only 15 % (from 80 to 68 $\text{m}^2\cdot\text{g}^{-1}$). Only at higher temperature a partial loss in structural order becomes apparent and the specific surface area is further reduced to 50 % of the initial value (40 $\text{m}^2\cdot\text{g}^{-1}$ after treatment at 650 °C).

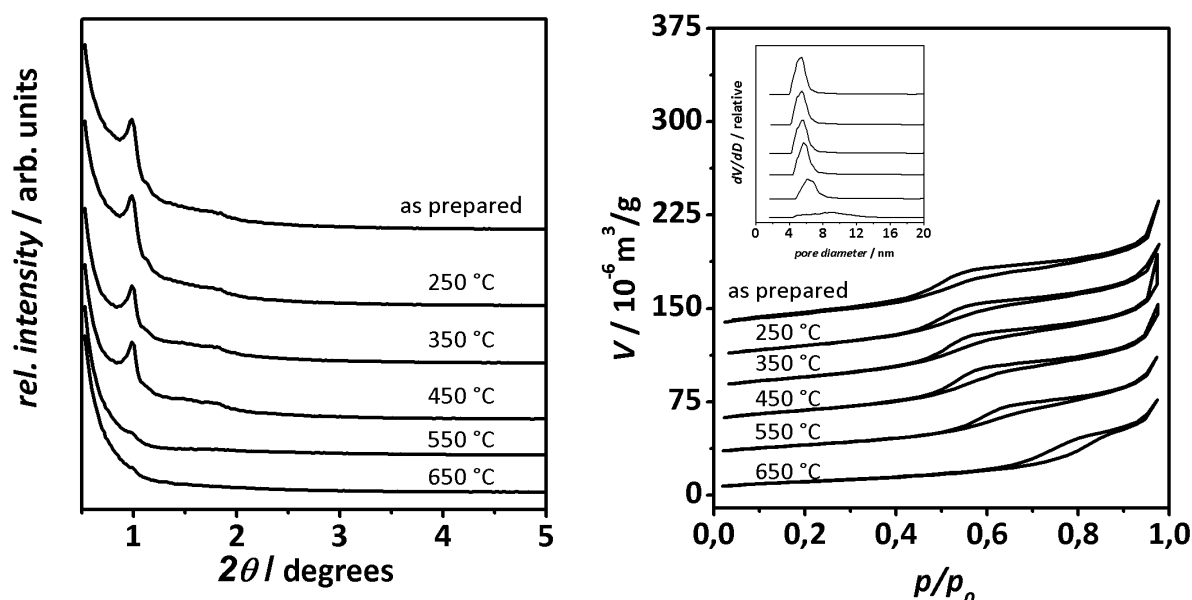


Figure 47. Low-angle P-XRD pattern (left) and nitrogen physisorption isotherms (right) with the corresponding pore size distribution (NLDFT; inset) of mesoporous In_2O_3 before and after thermal treatment at various temperatures.

For comparison, the same temperature treatment was carried out for samples of an In_2O_3 material prepared by a conventional sol-gel method:

A solution of 5 g InCl_3 (98%, Aldrich) in 100 ml water was added to 10 ml ammonia solution (25 %). The resulting mixture was stirred for 3 hours at room temperature. The solid product was then filtered off and dried at ambient temperature. The resulting powder was washed three times with water and dried at 50 °C for 2 days.

The freshly prepared material exhibited a specific BET surface area of 121 $\text{m}^2\cdot\text{g}^{-1}$. This value is higher than that of the sample prepared by structure replication, but the decrease due to thermal treatment is much more pronounced and takes place at lower temperature.

At 450 °C the BET surface area of the sol-gel prepared materials is already diminished by 62 % to 46 m²·g⁻¹. The data are shown in *Figure 48* for both materials.

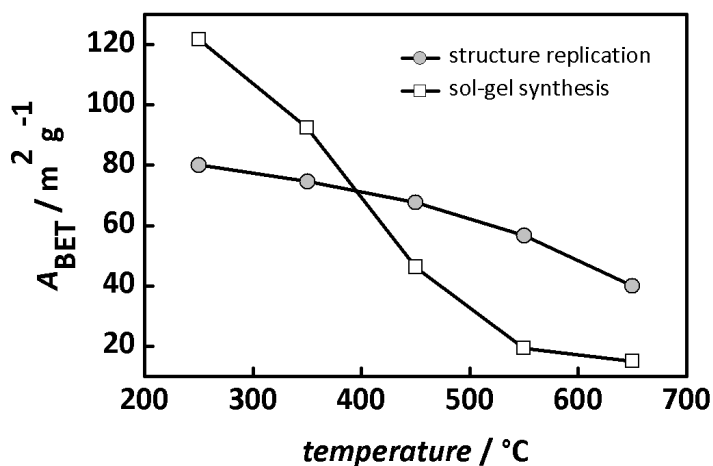


Figure 48. Evolution of the specific surface area of mesoporous In₂O₃ synthesized by structure replication compared to conventional sol-gel method.

These results reveal that a prolonged usage of mesoporous In₂O₃ as catalyst or gas sensor at elevated temperature is possible without substantial structural changes by sintering effects or grain growth due to ripening phenomena, a problem which is frequently encountered with conventional materials. All structural data are summarized in *Table 16*.

	<i>d</i> ₂₁₁ [nm]	average pore width <i>D_h</i> (NLDFT) [nm]	average pore wall thickness <i>h</i> [nm]	specific surface area <i>A_{BET}</i> [m ² ·g ⁻¹]	pore volume [cm ³ ·g ⁻¹]
In ₂ O ₃ as prepared	9.1	5.5	5.7	80	0.20
In ₂ O ₃ 250 °C	9.0	5.5	5.6	75	0.20
In ₂ O ₃ 350 °C	9.0	5.5	5.6	74	0.18
In ₂ O ₃ 450 °C	9.0	5.6	5.4	68	0.16
In ₂ O ₃ 550 °C	-	(6.3)	-	57	0.19
In ₂ O ₃ 650 °C	-	(9.0)	-	40	0.15

Table 16. Structural parameters from P-XRD and nitrogen physisorption data for In₂O₃ replicas after thermal treatment at various temperatures.

5.5 Synthesis and characterization of mesoporous In_2O_3 with carbon as template

As an alternative to mesoporous silica, mesoporous carbon may also be suitable as structure matrix for the synthesis of mesoporous In_2O_3 (see section 1.2.2.2). The utilization of mesoporous carbon will be expedient when cylindrical mesopores are desired, since the replica of a cylindrical pore arrangement, present in SBA-15 for example, consist rather of slit-like pores.

In a typical synthesis procedure a CMK-3 carbon matrix was impregnated with a saturated solution of $\text{In}(\text{NO}_3)_3 \cdot 5\text{H}_2\text{O}$ in THF to improve the wettability of the carbon sample (see section 1.2.3). After filtration by the incipient wetness technique the impregnated sample was dried at ambient temperature, heated for one hour to 250 °C under air atmosphere at a constant rate of 1 °C·min⁻¹, and kept at that temperature for one hour to convert indium nitrate quantitatively to indium oxide, according to the results of section 5.3. This procedure was repeated several times to achieve a complete pore filling. The carbon matrix was finally removed by heating the sample under air flow to 600 °C at a constant rate of 2 °C·min⁻¹ and keeping the sample at that temperature for two hours.

P-XRD pattern and nitrogen physisorption data of CMK-3 carbon and the resultant In_2O_3 material are shown in Figure 49.

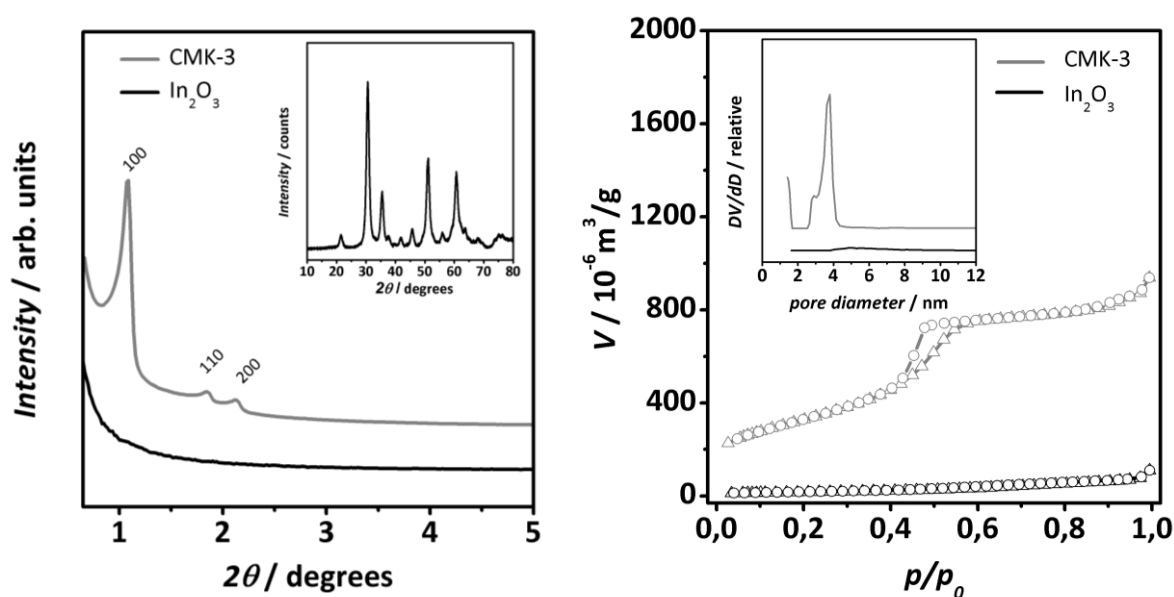


Figure 49. P-XRD pattern (left), and nitrogen physisorption measurements (right) of mesoporous CMK-3 template and the resulting In_2O_3 product.

The P-XRD pattern (left) of the resulting product reveal that the periodically ordered porosity of the structure matrix is not retained in the final product, also confirmed by analysis of the physisorption data (right). Regardless, the specific surface area still amounts to $60 \text{ m}^2 \cdot \text{g}^{-1}$, indicating a certain degree of textural porosity. The resulting material consists of loosely agglomerated small In_2O_3 crystals, as confirmed by TEM, but the mesostructure of CMK-3 carbon is not replicated (see *Figure 50*).

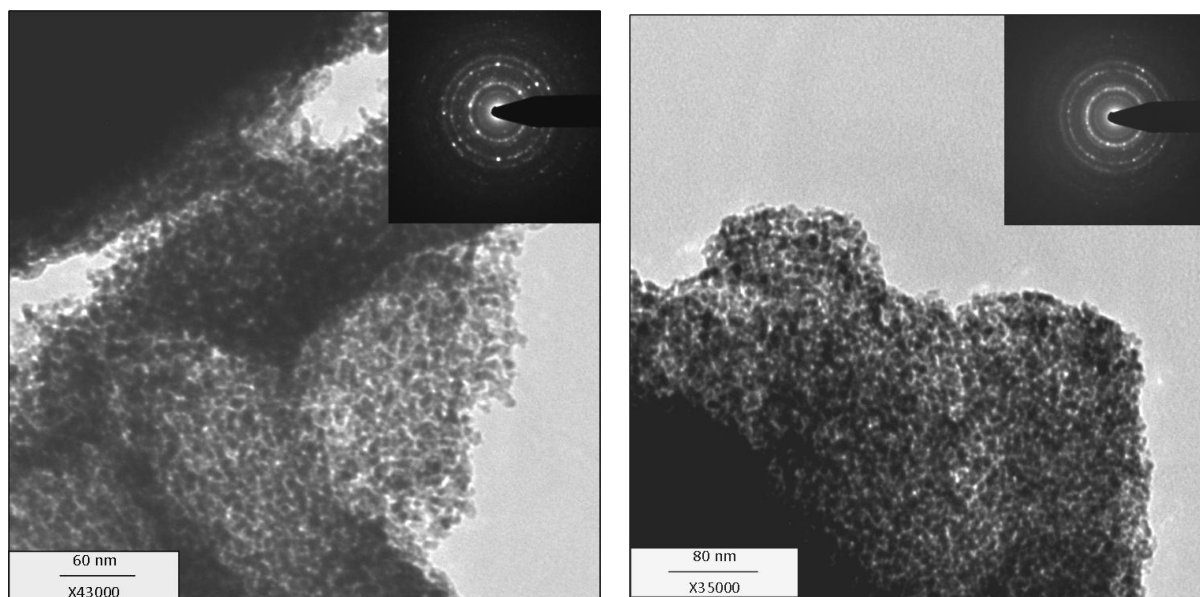


Figure 50. Representative TEM images of In_2O_3 products synthesized using CMK-3 carbon as template. Insets: SAED pattern of the corresponding spots.

The reason why mesoporous carbon fails to serve as a structure matrix in this particular case is most likely associated with the fairly high temperature of ca. 600°C needed for its final thermal combustion in air, as apparent from the TG/MS profile for a $\text{In}(\text{NO}_3)_3/\text{CMK-3}$ composite material (see *section 5.3*). Given the fact that the stability of mesoporous In_2O_3 samples at temperatures around 600°C was found to be rather limited, it is no surprise that the combustion of the carbon matrix in this temperature range is obviously harmful to the structural integrity of the In_2O_3 product (see *section 5.4.6*).

Further experiments intending a reduction of the template removal temperature reveal, that the CMK-3 carbon template can be removed indeed at a lower temperature of 350°C (heating rate $2^\circ\text{C} \cdot \text{min}^{-1}$ and holding the sample for two hours) in pure oxygen atmosphere (see *Figure 51*).

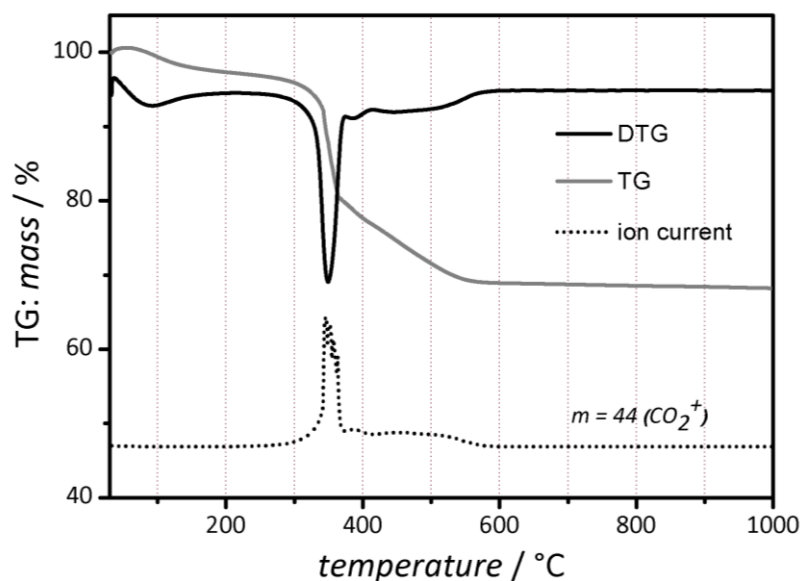


Figure 51. Coupled thermogravimetry and mass ion detection for a $\text{In}_2\text{O}_3/\text{CMK-3}$ composite material in pure oxygen atmosphere.

However, even with this procedure a non-structured product (confirmed by P-XRD and nitrogen physisorption, not shown) with a surface area as low as $65 \text{ m}^2\cdot\text{g}^{-1}$ was obtained. The failing of this synthesis strategy might be due to the combustion enthalpy of carbon, creating high local heat, which obviously leads to a structural loss. Another potential reason becomes apparent by considering of the crystallite sizes of the sample. In contrast to the In_2O_3 replica obtained by silica nanocasting, the crystalline domains in the present product are comparably small (ca. 10 nm, as compared to ca. 40 nm for In_2O_3 with silica as structure matrix), confirmed by the broad reflections in the P-XRD pattern (*Figure 49*, left) and the SAED pattern (*Figure 50*, insets) consisting of diffuse rings and spots. The small domains might be a result of the poor wettability of the non-polar carbon matrix with the highly polar In_2O_3 precursor ($\text{In}(\text{NO}_3)_3$) after the solvent (THF) evaporation. This poor wettability seems to cause a spreading of the precursor inside the matrix, instead of an island formation as in case of silica. This spreading leads consequentially to the formation of small particles, which are not sufficiently interconnected to stabilize the mesostructure after template removal. Hence, it can be concluded that mesoporous carbon is not suitable as structure matrix for In_2O_3 .

5.6 Gas sensing properties of mesoporous In_2O_3

5.6.1 Methane sensing properties of mesoporous In_2O_3

By utilization of templates with different sizes, the nanocasting strategy facilitates the manufacturing of mesoporous metal oxides with varying structural parameters. In addition, nanocast materials like In_2O_3 exhibit a mesostructure with high thermal stability (up to 450 °C) without loss of porosity due to sintering effects or grain growth by thermally induced ripening phenomena. These features make mesoporous In_2O_3 a promising material for the detection of gases that combust at high temperature, like methane. Furthermore the detection of methane plays an important role for explosion prevention, *e.g.* in domestic environment or factory plants. The lower explosion limit threshold is about 4 %; a gas warning system is required to trigger a pre-alarm between 0.13 % and 0.66 %.^[116]

The aim of the following study is to evaluate the relation between methane gas sensing properties and some structural parameters of In_2O_3 sensors, *i.e.* specific surface area, average pore width and average pore wall thickness. In order to exclude any differences in the gas sensing properties that might originate from differences in shape and symmetry of the pores, only In_2O_3 samples prepared from cubic KIT-6 silica are considered for this study. In addition, all In_2O_3 samples were prepared under identical conditions, such as temperature, precursor and conditions during etching of the matrices. The structural data of the materials are shown in Table 17.

	d_{211} [nm]	average pore width D_h (NLDFT) [nm]	average pore wall thickness h [nm]	specific surface area A_{BET} [m ² ·g ⁻¹]	pore volume [cm ³ ·g ⁻¹]
In_2O_3 (a)	7.8	6.0	3.2	90	0.23
In_2O_3 (b)	9.0	5.4	4.4	75	0.16
In_2O_3 (c)	9.0	5.6	4.3	70	0.12
In_2O_3 (d)	9.3	5.4	4.6	52	0.08
In_2O_3 (e)	8.0	5.0	3.8	38	0.07

Table 17. Overview of the structural data of mesoporous In_2O_3 materials with varying pore sizes and wall thicknesses utilized for gas sensing experiments.

Figure 52 shows time-resolved measurements for CH₄ in synthetic air with a relative humidity of 50 % in concentrations between 1300 and 6600 ppm - technically relevant for explosion prevention - and a sensor operating temperature of 350 °C. The sensors exhibit different specific BET surface areas ranging from 38 m²·g⁻¹ (e) to 90 m²·g⁻¹. (a) The sensitivity was chosen as measured variable for the sensor behavior (see section 4.6). Upon increasing the methane concentration, the sensitivity increases for all sensors, whereas the sensor response is more pronounced for sensors with a high surface area.

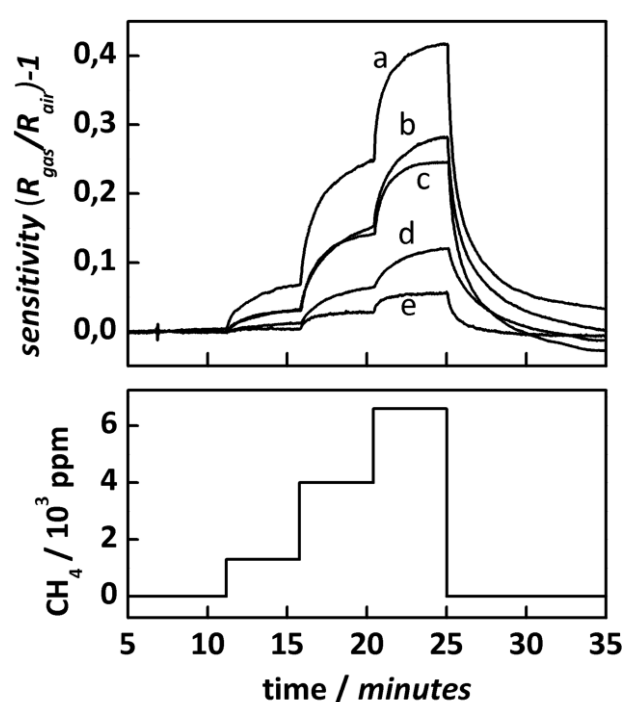


Figure 52. Time-resolved sensitivities (top) of a series of mesoporous In₂O₃ materials to methane gas in technically relevant concentrations (bottom). The sensors exhibit different surface areas, pore sizes and wall thicknesses (see Table 17).

Figure 53 shows the dependency between sensitivity and specific surface area of the sensor material after signal saturation at a CH₄ concentration of 6600 ppm. A linear fit to the data delivers a very good match (correlation coefficient $R^2 = 0.953$). Similar results were observed by Kawi et al. for nanoporous SnO₂ materials with specific surface areas between 50 and 160 m²·g⁻¹ to H₂ and CO at concentrations of 500 ppm.^[117, 118] The series of the respective SnO₂ samples had been prepared at different pH values, which is why differences in the sensitivity might also be attributable to potential differences in the surface-chemical

properties of the samples. However, it is reasonable to assume *a priori* a near-(linear) correlation between the sensitivity and the specific BET surface area, taking into account that the sensor signal is the result of surface-chemical reactions.

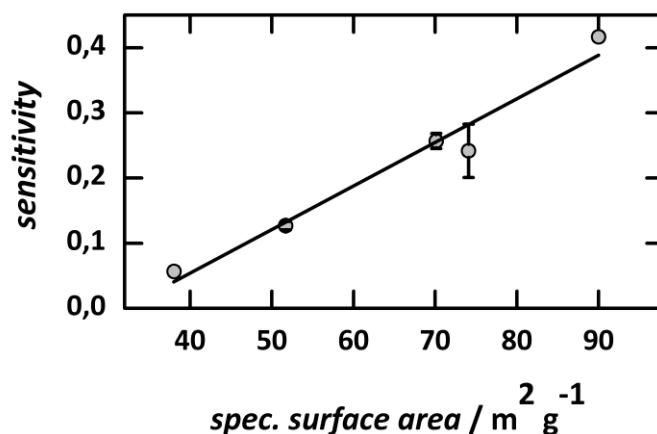


Figure 53. Correlation between the sensor sensitivity and specific surface area at a CH₄ concentration of 6600 ppm.

Apart from the impact of the specific surface area, another interesting question is whether or not the sensitivity is also dependant on the average pore width and/or average pore wall thickness. For this purpose it has to be taken into account that all three parameters are coupled with each other to some degree: due to the synthesis procedure the pores tend to be narrower when the pore walls are thicker; consequently, the surface-to-volume ratio follows the same trend, *i.e.* lower specific BET surface areas are found for thicker walls/narrower pore widths (see *section 5.4.3*). This means that it is not possible in a straightforward way to distinguish between the individual impacts of the three parameters on the sensitivity. Therefore it is reasonable to de-couple pore width and pore wall thickness from the BET surface area, which can be regarded as a true causal correlation in order to develop an impression of their individual impact on the sensitivity. For this purpose the measured sensitivity was divided by the BET area, resulting in a 'surface-normalized' sensitivity. *Figure 54* shows this normalized sensitivity versus the average pore width varying between 5.0 and 6.0 nm (left) and versus the average pore wall thickness between 3.5 and 5.9 nm (right), respectively. In both cases a correlation is observed; the normalized sensitivity tends to be higher for wider pores and thinner pore walls, the correlation being less stringent for the wall thickness than for the pore width. Owing to the above-mentioned

correlation between the two structural parameters (wider pores go along with thinner pore walls), it is impossible to decide analytically which of the two (or both) are responsible for the different normalized sensitivities.

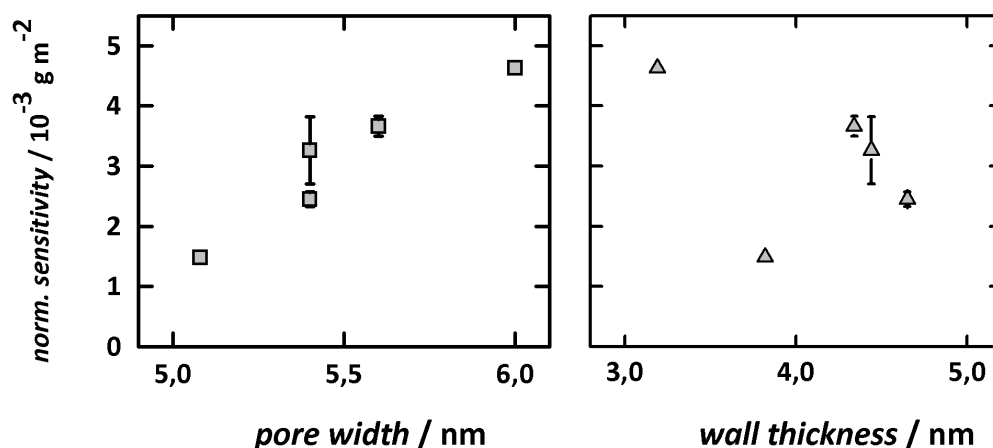


Figure 54. Correlation between the surface-normalized sensitivity and average pore width (left) and average pore wall thickness (right).

However, theoretical considerations suggest that the wall thickness rather than the pore width is likely to be the determining factor, for the following reasons. If the trends observed in *Figure 54* were attributable to the differences in the pore width, then this would most likely point toward an effect originating from pore size-dependant diffusion of the gas molecules through the pores. For pore sizes in the region of a few nanometers (2 - 50 nm), the mean free path of gas molecules is larger than the pore size, which means, that the gas molecules collide with the pore wall much more frequently than they collide with other gas molecules which affects the diffusion of the gas molecules. This kind of transport is called KNUDSEN diffusion, with the diffusion coefficient (D_K) depending linearly on the pore width (see eq. 10).

$$D_K = \frac{2}{3} r \sqrt{\frac{8RT}{\pi M}} \quad (10)$$

D_K = diffusion coefficient
 R = universal gas constant
 T = temperature
 M = molar mass of the gas

According to a model suggested by Sakai et al. the gas sensitivity of a porous semiconducting metal oxide may indeed increase with the KNUDSEN diffusion coefficient and, thus, with the pore size.^[119] However, according to this model, such a pore size dependency is negligible here, since the reaction rate of methane under these experimental conditions is very low and no significant concentration gradient within this sensing layer may be expected in the first place. It is therefore much more likely that the pore wall thickness is the structural parameter responsible for the trends observed in *Figure 54* and that the correlation with the pore width is just an indirect effect (since the pore width is coupled with the wall thickness). Strong correlations between the size of crystalline structures in the nanometer range and the sensitivity are well known in the literature for granular materials such as SnO₂ prepared by sol-gel methods, as discussed, for example, by Yamazoe et al.^[120] However, such standard models are not applicable here, because the respective In₂O₃ materials are not granular. In particular, the pore wall thickness is below the DEBYE length (which corresponds to the depletion layer thickness in a granular system), which leads to the important consequence that, contrary to classical models, no band bending will be caused by the surface adsorbates; instead, a general shift of the FERMİ level will occur.^[121, 122] It can be proposed that a model based on electrically active surface states (called 'surface traps' in case of electron-entrapment), similar to the one described by McAleer for thin films, is more appropriate here.^[123] In this model the traps cause a homogeneous decrease in charge carrier density rather than a localized decrease as in the classical model of grain boundaries. In effect homogenous doping of the porous solid occurs by charge transfer adsorbates (surface donors). This effect is stronger when the pore walls are thinner.^[120]

5.6.2 Ozone sensing properties of mesoporous In₂O₃

Crystalline indium oxide is frequently used as a selective and sensitive material for the detection of ozone (O₃) in fields of environmental monitoring of the ozone exposure which for example, originates from laser printers, photocopiers or UV irradiation as part of the sunlight.^[89-91] The utilization of ordered mesoporous In₂O₃ as ozone gas sensor, however, has not been reported yet. In this study the ozone sensing properties of cubic mesoporous In₂O₃ are investigated in comparison to commercially available bulk In₂O₃ material (Sigma) with a surface area of ca. 20 m²·g⁻¹. The structural data of the mesoporous In₂O₃ material have

already been listed in *Table 13* (KIT-6-140 as template). In order to ensure comparable surface chemical properties, the bulk material was pre-treated according to synthesis conditions used for the fabrication of the mesoporous In_2O_3 material, *e.g.* dispersion in 2 M NaOH two times for four hours, followed by washing and drying. Furthermore, the sensors were manufactured under likewise identical conditions (see *section 5.2.1*). As an ozone source a SIEMENS-type device was applied: A mixture of oxygen in argon (20.5 %) was utilized to avoid the formation of nitric oxides expected by the use of synthetic air. The fabricated ozone concentration was determined by an ozone analyzer (Thermo Electron Corporation, *Model 49C O3 Analyzer*). The first measurements were carried out at a sensor working temperature of 200 °C and an ozone concentration of 1.2 ppm. *Figure 55* displays the time-resolved measurements of the electric resistance of the mesoporous and non-porous In_2O_3 sensors on repeated exposure cycles towards ozone. Both sensors reveal a highly reproducible sensor signal, but the mesoporous sensor exhibits a faster and stronger change in resistance than the non-porous sensor. In case of the mesoporous sensor saturation is observed within ca. 5 minutes, contrary to the non-porous sensor.

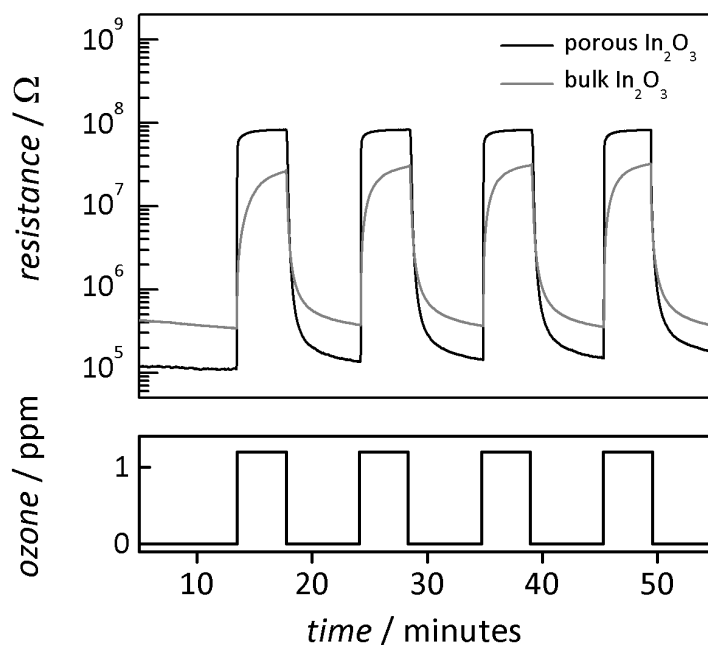


Figure 55. Time-resolved ozone sensing measurements (change in resistance) for mesoporous and non-porous In_2O_3 at 200 °C towards ozone gas in 1.2 ppm concentration (bottom).

An empirical analysis concerning the sensor response reveal, that the mesoporous sensor is significantly faster. The time constant of the sensor response during ozone exposure was determined by an *exponential decay*

$$y = y_0 + Ae^{-\frac{x}{t}} \quad (11)$$

to $t = 338 \pm 3$ s for the non-porous sensor. For the porous sensor a *exponential decay*

$$y = y_0 + A_1e^{-\frac{x}{t_1}} + A_2e^{-\frac{x}{t_2}} \quad (12)$$

was fitted resulting in two different time constants, whereas the first was determined as $t_1 = 5 \pm 0.1$ s and the second to $t_2 = 99 \pm 3.0$ s. The same trend is observed for the recovery time after termination of the ozone exposure which is apparently faster for the mesoporous In_2O_3 sensor. With regard to the sensitivities towards 1.2 ppm ozone the porous sensor exhibits a sensitivity about 9.5 times higher than the non-porous sensor.

Because of the high and fast change in the resistance by about three orders of magnitude at 200 °C, further experiments were carried out at room temperature. *Figure 56* displays the measurements of two ozone exposure cycles (1.2 ppm) with mesoporous and non-porous In_2O_3 at room temperature.

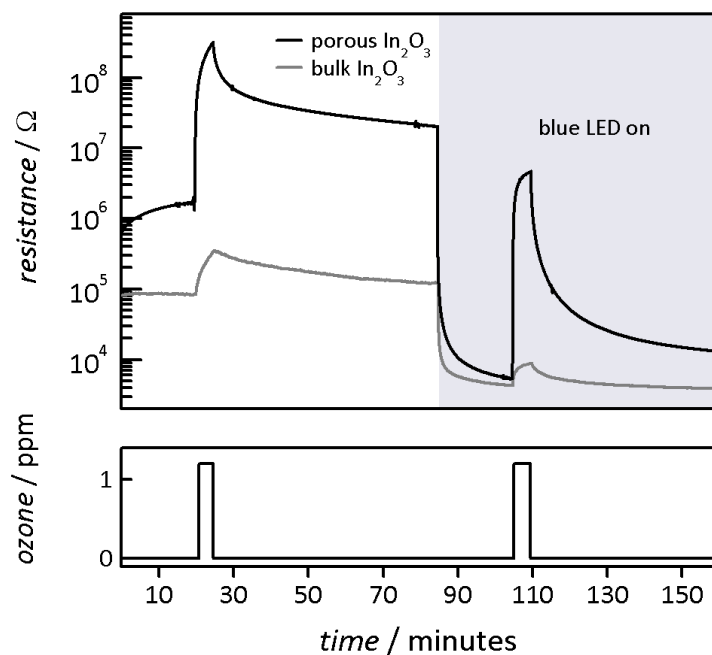


Figure 56. Time-resolved ozone sensing measurements (change in resistance) for mesoporous and non-porous In_2O_3 at room temperature to ozone gas in 1.2 ppm concentration (bottom).

In the first cycle, the porous sensor possess a significantly stronger change in resistance (more than 2 orders of magnitude) in comparison to the non-porous sensor. In contrast, after termination of the ozone exposure, the non-porous sensor decays nearly to its ground resistance, not achieved for the porous sensor during the measuring time. Due to the comparable long recovery time for both sensors at room temperature, the sensors were irradiated with blue light prior to the second ozone exposure. The influence of UV light irradiation, investigated by Comini et al., has turned out to be beneficial for the overall sensor performance of SnO_2 and In_2O_3 sensors operated at room temperature (see below). The blue irradiation causes a steep decrease in the sensor resistance for both sensors. A further ozone exposure during the irradiation with the blue light leads to an increase in the resistance for both sensors, which is about three orders of magnitude larger in case of the mesoporous In_2O_3 sensor. After termination of the ozone exposure, the recovery time could apparently be reduced in comparison to the first experiment without irradiation.

An exhaustive elucidation of these observations are not possible in a straightforward way in the present work, since the underlying principles are complex and not understood in detail; hence only a short overview of presumably involved effects is presented: In the last few years, a lot of research activity has been focused on the enhancement of gas sensing properties of granular systems at room temperature by light irradiation. When the surface of such a semiconducting metal oxide is been in contact with ambient air, the adsorption of oxygen and the subsequent creation of ionosorbed species are initiated (see *section 3.3*). These processes can substantially be influenced by illumination, either negative or positive, resulting in a decrease or increase of the adsorption rate. Furthermore the time dependency of the adsorption rate and the activation energy can be changed by irradiation, too. The most trivial origin for an improved conductivity may be due to heating of the sensing layer by light absorption. Another conceivable effect, described by Comini et al.^[124, 125] deals with photosorption/photoreduction phenomena, used as an explanation model for the increase of conductance by irradiation with UV light on SnO_2 and In_2O_3 grains: When light is absorbed by the semiconductor, a hole-electron pair is generated in the near surface region. The hole is pulled to the surface, recombining there with the adsorbed oxygen species; the oxygen species desorb from the surface which leads to a decrease in the intergrain barrier height. The electron instead enhances the conductivity by occupying an energy level in the conduction band which leads also to an increase of the conductivity. For this model, it has to be taken into

account that the light energy must suffice to promote the electron in the conduction band. In case of In_2O_3 as sensitive layer the direct band gap is ca. 3.0 eV^[113] which can be transcended by UV-light (3.3 ... 6.2 eV). The mentioned effect, however, considers only granular systems, with much larger crystallites contrary to this thesis. Here, the mesoporous In_2O_3 samples possess large single-crystalline domains with (presumably complete depleted) small pore walls, thus the above explanations, can not be directly transferred. Moreover for the present experiments, lower energy light (2.8 eV) was used. Despite the larger expected band gap, an enhancement of the sensing properties was observed. That might be due to additionally created acceptor states in the band gap, or a raise of the donor level due to additional oxygen vacancies. Thus the energy required for excitation of an electron is reduced. This effect was already described by Faglia et al. as 'photoinduced desorption by subbandgap light' for nanocrystals.^[126] Even though the phenomena involved in the photoactivation processes are not exhaustively understood, the results obtained are quite promising. With the employment of light, it might become possible to produce gas sensors that can be used at room temperature with decreased risk of explosion of hazardous gases.

6. Synthesis and characterization of mesoporous tin(IV) oxide

6.1 Tin oxide

Tin(IV) oxide (SnO_2) appears mostly as cassiterite (Zinnstein) and crystallizes in the tetragonal rutile structure. SnO_2 is widely used as an *n*-type semiconductor in the field of gas sensing due to its high sensitivity and fast response. SnO_2 is further employed as a transparent conductive oxide (TCO) in LCD displays or as an electrode material in photovoltaics.

6.2 Synthesis of mesoporous templates

For the synthesis of mesoporous SnO_2 KIT-6-80 silica was utilized as the template. The synthesis and characterization have already been described in *section 5.2.1*.

6.3 Conversion of SnO_2 precursor in mesoporous silica

In contrast to the metal oxide systems discussed before, the utilization of tin nitrate ($\text{Sn}(\text{NO}_3)_4$) was not suitable as precursor since aqueous Sn(IV) solutions are generally unstable and precipitate as $\text{Sn}(\text{OH})_4$.^[127] For this reason, tin(II)chloride ($\text{SnCl}_2 \cdot 2\text{H}_2\text{O}$, Sigma) was used as an alternative due to its high solubility and stability in polar solvents like water and ethanol. More important, a thermal decomposition of SnCl_2 into SnO_2 is feasible applying an appropriate temperature under atmospheric conditions.^[46, 128]

Figure 57 shows the thermogravimetric analysis of SnCl_2 in a mesoporous KIT-6 host matrix. The main mass loss (31 %) occurs between 60 and 200 °C in two steps which overlap to some degree and another slight one of ca. 0.7 % between 200 and 450 °C. The first step of the main mass loss is attributed to the release of residual water, the second one can be explained by the evolution of various chlorine species. This shows that the decomposition of SnCl_2 is almost completed at ca. 160 °C which is significantly lower than the oxide formation temperature for a pure SnCl_2 sample determined to ca. 450 °C.

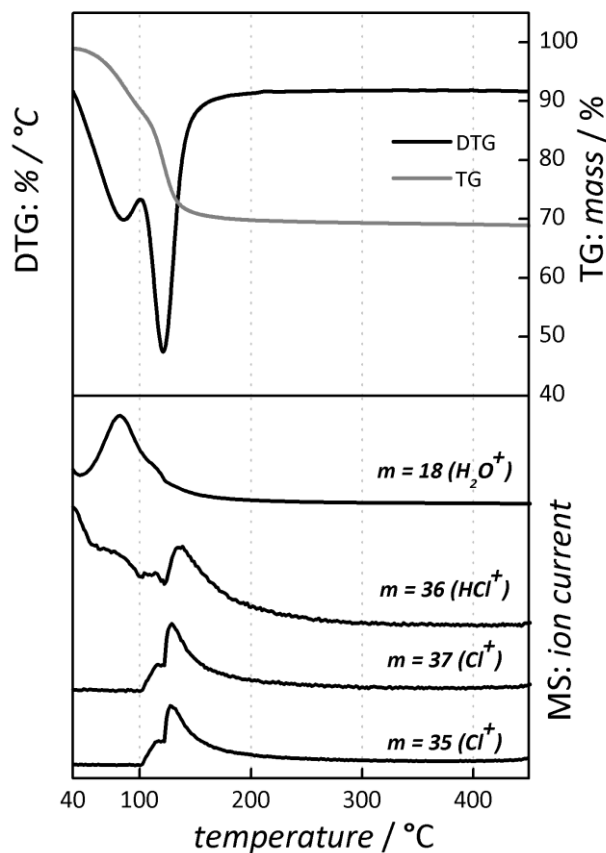


Figure 57. Coupled thermogravimetry (TG) and mass ion detection (MS) for KIT-6 silica impregnated with a saturated SnCl_2 solution in water.

6.4 Synthesis and characterization of mesoporous tin oxide

6.4.1 Synthesis of mesoporous SnO_2

For the synthesis of mesoporous SnO_2 a KIT-6 host structure was impregnated by the incipient wetness technique with a saturated solution of $\text{SnCl}_2 \cdot 2\text{H}_2\text{O}$ (98 %, Merck). After drying in an oven at 60 °C for 24 hours, the sample was treated at 450 °C for two hours in air with a heating rate of 2 °C·min⁻¹ to convert the SnCl_2 precursor quantitatively into SnO_2 , according to the results of *section 6.3*. To analyze the influence of the cycles on the resulting particle morphology and size, three cycles of impregnation and oxide formation were accomplished according to *section 5.4.4*; after each cycle the silica matrix was removed by stirring the composites in an aqueous solution of 2 M NaOH for 24 hours at room temperature.

6.4.2 Characterization of composite materials

Figure 58 (left) shows the low-angle P-XRD pattern of KIT-6 silica and the respective $\text{SnO}_2/\text{KIT-6-80}$ composite materials after several cycles of impregnation and conversion into the oxide. No significant shift of the d-values ($d_{211} = 7.9 \dots 8.2$) due to the impregnation and oxide formation procedures is observed, but the reflection intensities decrease with every cycle indicating an increased filling of the pores with SnO_2 , that lowers the scattering contrast, also observed for the other composite systems of that work.

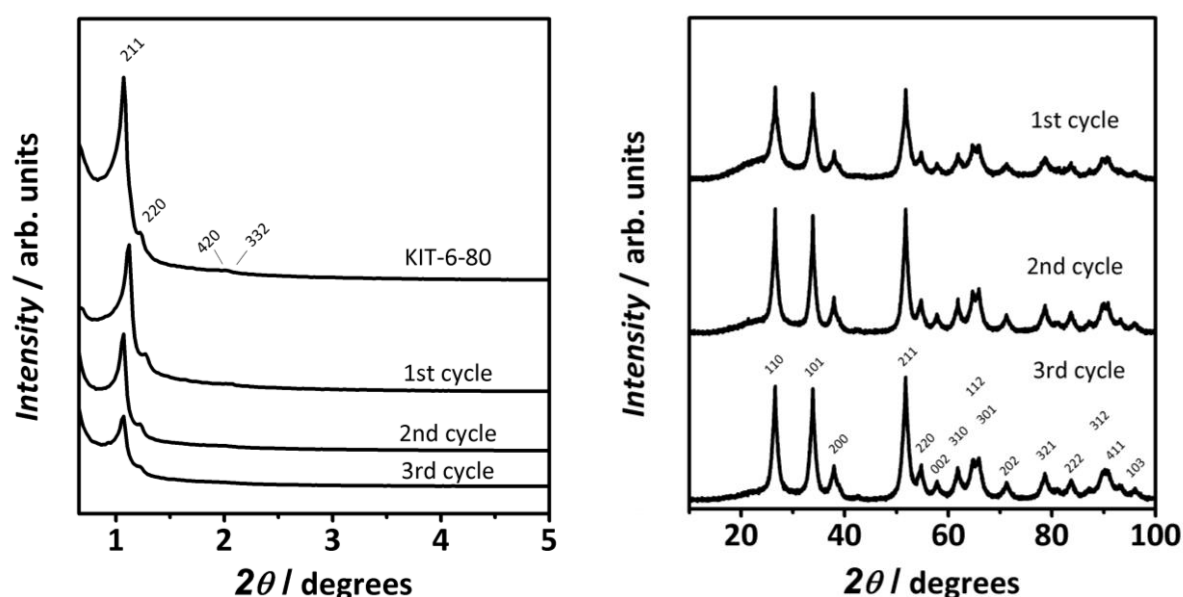


Figure 58. Low-angle P-XRD pattern of mesoporous KIT-6 silica and the corresponding $\text{SnO}_2/\text{KIT-6}$ composite materials obtained after several cycles of impregnation and oxide formation.

Furthermore the filling of the pores with SnO_2 is confirmed by the wide-angle diffraction pattern. Figure 58 (right) displays the diffractograms recorded after each cycle; the reflections can be indexed according to the tetragonal rutile structure, characteristic for crystalline SnO_2 . With application of the SCHERRER formula (see eq. 7) the average size of the crystalline domains is calculated as ca. 6 nm for SnO_2 in the KIT-6 silica matrix.

Figure 59 shows the physisorption isotherms (left) of the silica matrix and the corresponding $\text{SnO}_2/\text{KIT-6}$ composites. All materials show a type IV isotherm with H1 hysteresis.

The gradual filling of the pores with SnO₂ is confirmed by a significant decrease in the amount of the adsorbed nitrogen volume. The structural data, including the corresponding specific surface area and pore volume of the samples are listed in *Table 18*.

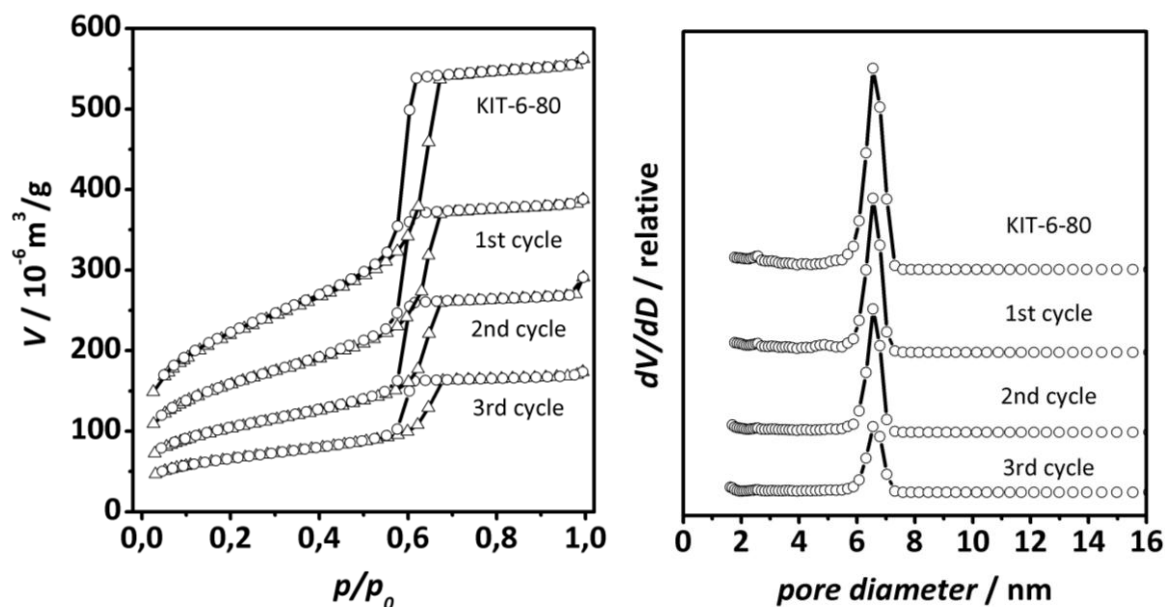


Figure 59. Nitrogen physisorption isotherms of KIT-6 and SnO₂/KIT-6 composite materials obtained after several cycles of impregnation and oxide formation (left) and the corresponding NLDFT pore size distribution (right).

The pore size distributions of the silica template and the composite materials calculated by the NLDFT model are shown in *Figure 59* (right). The peak maxima do not significantly shift from cycle to cycle, indicating that the growth of SnO₂ crystals occurs predominantly along the pore axis according to the previously proposed schematic drawing concerning the growth direction (see *section 5.4.4*).

	d_{211} [nm]	average pore width D_h (NLDFT) [nm]	average pore wall thickness h [nm]	specific surface area A_{BET} [m ² ·g ⁻¹]	pore volume [cm ³ ·g ⁻¹]	$FWHM_{110}$ [°]
KIT-6-80	8.2	6.5	3.5	751	0.86	
1 st cycle	7.9	6.5	3.2	544	0.58	1.4
2 nd cycle	8.2	6.5	3.5	355	0.41	1.1
3 rd cycle	8.2	6.5	3.5	223	0.26	1.1

Table 18. Overview of the structural data of mesoporous KIT-6-80 silica and the respective composite materials obtained after several cycles of impregnation and oxide formation.

6.4.3 Characterization of mesoporous SnO₂

Figure 60 depicts the P-XRD measurements of mesoporous silica-free SnO₂ obtained after each cycle of impregnation and oxide formation. The low-angle pattern of SnO₂ material (left) obtained after the first cycle shows only a small shoulder in the region of $2\theta \approx 1.1^\circ$ which is attributable to the intensive 211 reflection of the parental silica structure. However, ordered regions can be observed in TEM analysis, depicted in a representative image in Figure 61 (left). In contrast, SnO₂ materials after the second and third cycle show two well resolved reflections (211, 220). Also TEM analysis confirm a long range order of the mesostructure depicted for SnO₂ yield after the second cycle (see Figure 61, right).

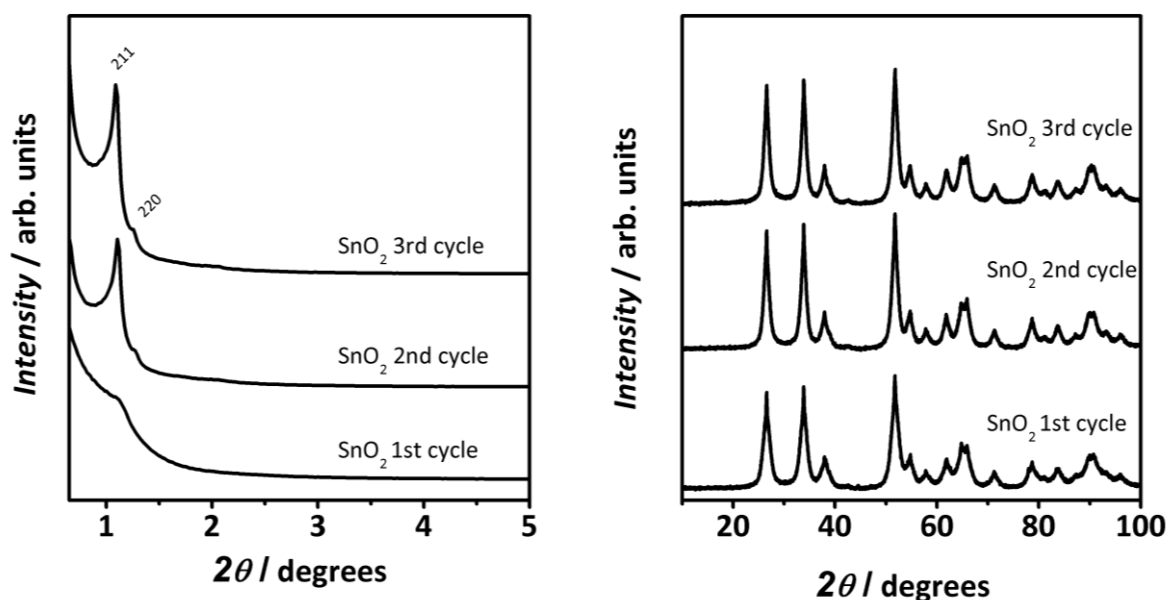


Figure 60. Low-angle P-XRD pattern of mesoporous SnO₂ samples obtained after one, two and three cycles of impregnation and conversion into the oxide.

The wide-angle P-XRD pattern of mesoporous SnO₂ shows well-resolved reflections for all SnO₂ materials confirming that the removal of the host matrix with NaOH does not influence the crystal structure of the material; the domain size was the same as determined for the composites.

The crystalline structure of the material was also confirmed by SAED. The corresponding diffraction images are displayed in *Figure 61* as insets. The patterns, consisting of diffuse rings and spots, reveal that the materials consist of only small crystalline domains. EDX analysis on 5 spots results in a Sn : Si atomic ratio of 90 : 10.

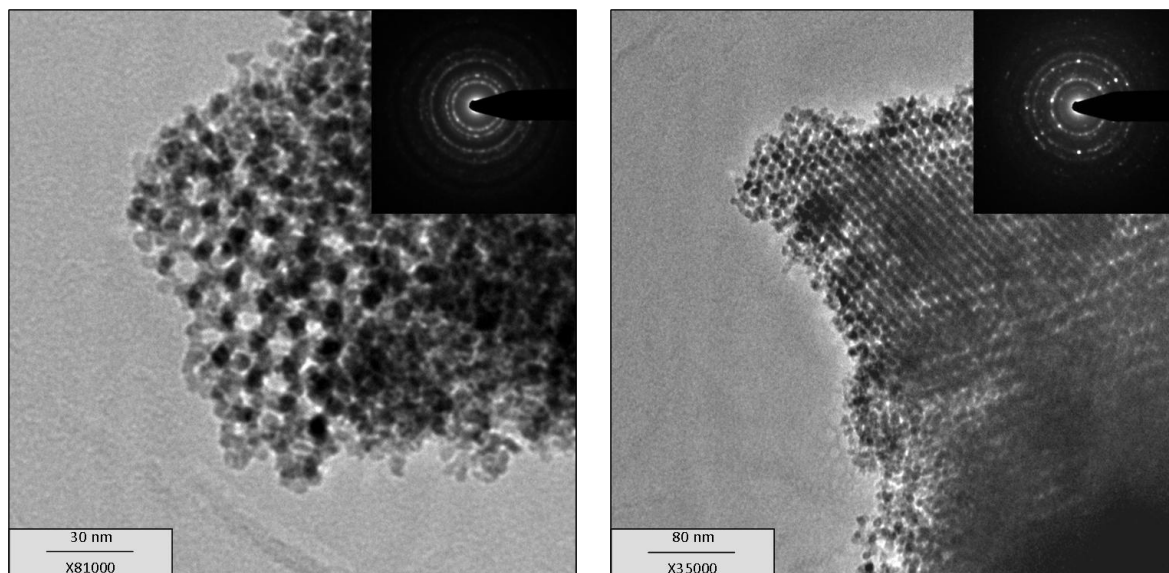


Figure 61. Representative TEM images of mesoporous SnO₂ yield after the first (left) and the second (right) cycle of impregnation and oxide formation.

The data of the physisorption measurements are depicted in *Figure 62*. All materials exhibit type IV isotherms with two capillary condensation steps at $p/p_0 \approx 0.4$ and at $p/p_0 \approx 0.8$ respectively. The hysteresis loops in the low pressure region are weakly pronounced, which is caused either by small micropores or short pore channels that indicates the presence of small particle sizes. However, the presence of small particles seems more likely with regard to the wall thicknesses of the KIT-6 template. The corresponding pore size distributions obtained from NLDFT calculations reveal nearly the same maximum of ca. 4.5 nm which is about 1 nm larger than the wall thickness of the respective silica template. The differences $D_h(\text{silica}) > h(\text{SnO}_2)$ and $D_h(\text{SnO}_2) > h(\text{Silica})$ can be explained with a incomplete pore filling during the synthesis already mentioned (see *section 5.4.4*). A further peak in the pore size distribution in the range between 9 and 14 nm as well as the second hysteresis loop in the isotherms, present in all samples, indicate that the mesoporous SnO₂ materials consist of small primary particles forming additional interparticular porosity, which is also confirmed by SEM analysis (see below). The complete structural data of the samples discussed are listed in *Table 19*.

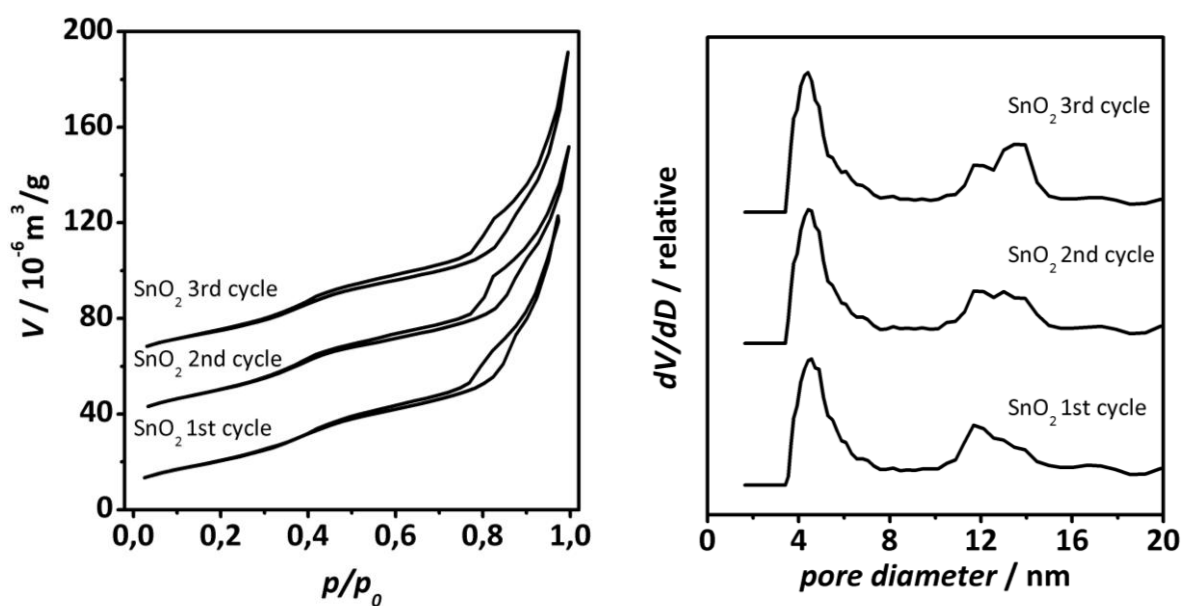


Figure 62. Nitrogen physisorption isotherms of mesoporous SnO_2 materials obtained after several cycles of impregnation and oxide formation.

As already observed for the composite materials as well as for the In_2O_3 materials (see section 5.4.4), no shifting of the pore size maxima is obtained, which confirms that the formation of SnO_2 crystals occurs predominantly along the pore axis.

	d_{211} [nm]	average pore width D_h (NLDFT) [nm]	average pore wall thickness h [nm]	specific surface area A_{BET} [$\text{m}^2 \cdot \text{g}^{-1}$]	pore volume [$\text{cm}^3 \cdot \text{g}^{-1}$]	FWHM_{110} [°]
KIT-6-80	8.2	6.5	3.5	751	0.86	
SnO_2 1 st cycle	-	4.4	-	76	0.18	1.4
SnO_2 2 nd cycle	8.0	4.4	5.4	80	0.16	1.0
SnO_2 3 rd cycle	8.1	4.6	5.3	80	0.18	1.0

Table 19. Overview of the structural data of mesoporous SnO_2 materials obtained after several cycles of impregnation and oxide formation.

Figure 63 shows representative SEM images of silica-free mesoporous SnO_2 obtained after the first (a, b) and the third (c, d) cycle. Interestingly, the particle size and morphology of SnO_2 obtained after each cycle, delivers similar values ($9.5 \mu\text{m} \pm 4.3 \mu\text{m}$) on the μm scale. With regard to the average particle size of the KIT-6 structure matrix, SnO_2 particles are obviously

larger, which can be explained by agglomeration. To determine the size of the primary particles, SnO_2 samples of the first and third cycle were dispersed in a more diluted concentration ($5 \text{ mg}\cdot\text{ml}^{-1}$). *Figure 63* (b) and (c) display SEM images of the respective SnO_2 particles. In contrast to previously presented In_2O_3 materials, mesoporous SnO_2 particles are significantly smaller and do not strongly differ in their sizes from cycle to cycle. The material obtained after the first cycle consists of particles of an irregular shape and an average size of $57 \pm 15 \text{ nm}$, which is similar for the particles after the second ($57 \pm 26 \text{ nm}$; not shown) and the third cycle ($63 \pm 23 \text{ nm}$). Thus, in contrast to the previously described growth model proposed for In_2O_3 , in case of SnO_2 additional cycles lead predominantly to the creation of new particles rather than to growth of already existing ones. This might be a result of a lower precursor mobility in the pores, caused by distinct physical properties, *e.g.* viscosity and polarity, of the SnCl_2 precursor compared to $\text{In}(\text{NO}_3)_3$. In *Figure 63* (d), the resolution is sufficient to show the nanometer-scaled periodicity of the mesopore systems at the particles' outer surfaces (inset). Furthermore, a high degree of interparticular porosity can be observed which explains the additional peak between 9 and 14 nm in the pore size distribution already mentioned (see *Figure 62*, right).

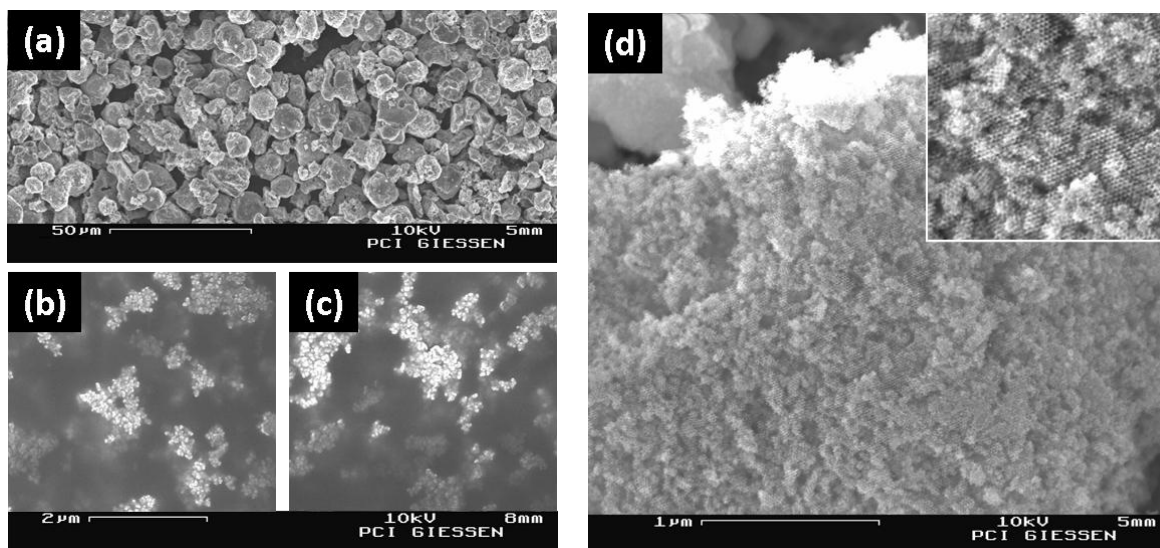


Figure 63. SEM images of mesoporous SnO_2 particles obtained after the first (a, b) and the third cycle of impregnation and oxide formation (c, d). Inset of (d) displays a close-up view of a representative part of the sample.

6.4.4 Temperature stability of mesoporous SnO₂

With regard to potential applications of mesoporous SnO₂ in fields of gas sensing or catalysis, temperature stability experiments were carried out similar to those described in *section 5.4.6*. To investigate the thermal stability, samples of mesoporous SnO₂ were placed in a furnace at distinct temperatures between 200 °C and 800 °C for four hours with a heating rate of 10 °C·min⁻¹ under air atmosphere, followed by cooling to room temperature. For each temperature a previously non-heated sample was chosen. For the treatment at 200 and 400 °C, the SnO₂ sample obtained after the second cycle was utilized, for the treatment at 600 °C and 800 °C SnO₂ of the third cycle was employed (the respective structural data of the materials are listed in *Table 19*). *Figure 64* displays the P-XRD pattern (left) and the data obtained from nitrogen physisorption measurements (right) after the thermal treatment.

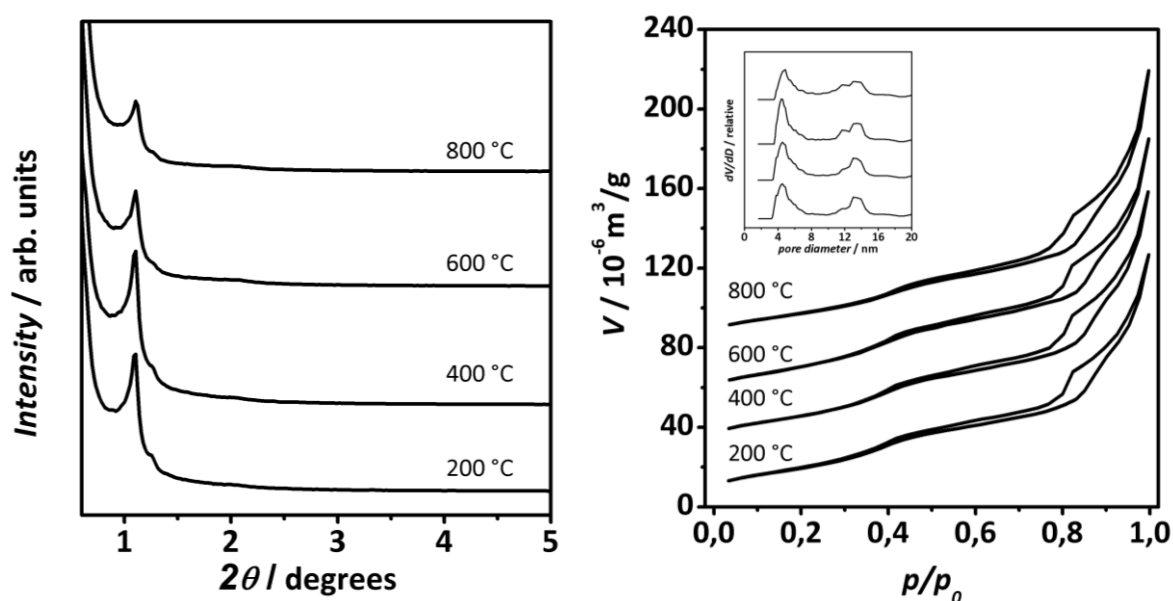


Figure 64. Low-angle P-XRD pattern (left) and nitrogen physisorption isotherms (right) with the corresponding pore size distribution (NLDFT; inset) of mesoporous SnO₂ samples after thermal treatment at distinct temperatures.

The position of the low-angle P-XRD reflections and the shape of the physisorption isotherms remain almost the same up to 800 °C, which confirms that no significant loss in mesostructural order and porosity takes place. The BET surface areas are mostly constant for temperatures up to 600 °C, anyway a loss of ca. 18 % is observed for the sample treated at 800 °C. The structural data of the thermal treated samples are listed in *Table 20*.

	d_{211} [nm]	average pore width D_h (NLDFT) [nm]	average pore wall thickness h [nm]	specific surface area A_{BET} [m ² ·g ⁻¹]	pore volume [cm ³ ·g ⁻¹]
(SnO ₂) as prepared	8.0	4.4	5.4	80	0.16
SnO ₂ 200 °C	8.0	4.4	5.4	78	0.16
SnO ₂ 400 °C	8.0	4.4	5.4	80	0.17
(SnO ₂) as prepared	8.1	4.6	5.3	80	0.18
SnO ₂ 600 °C	8.0	4.6	5.2	80	0.16
SnO ₂ 800 °C	7.9	4.8	4.9	66	0.16

Table 20. Overview of the structural data of mesoporous SnO₂ materials after thermal treatment at distinct temperatures.

6.5 Gas sensing properties of mesoporous SnO₂

For the detection of gases that combust at high temperatures, like methane, the materials employed as gas sensors must possess a high thermal stability without structural loss.^[129] As it was shown in the previous section, mesoporous nanocast SnO₂ exhibits that desired feature making it a promising candidate for methane gas detection in contrast to conventional synthesized sol-gel SnO₂, whose thermal stability is rather limited. In the latter case elevated temperatures generally lead to the growth of crystalline SnO₂ particles due to ripening processes, for example caused by grain-rotation-induced grain coalescence.^[130] This lowers the surface-to-volume ratio and finally results in a decrease of the sensitivity.

In order to investigate the gas sensing properties of nanocast SnO₂, sensors of cubic mesoporous SnO₂ obtained after the third cycle of impregnation and oxide formation (see Table 19) were fabricated according to section 6.4.1. The gas sensing experiments were carried out at distinct sensor operation temperatures in technically relevant methane concentrations of 4000 ppm (explosion prevention, see section 5.6.1) and a relative humidity of 50 %. Figure 65 shows the sensor sensitivity at 500 °C and 600 °C.

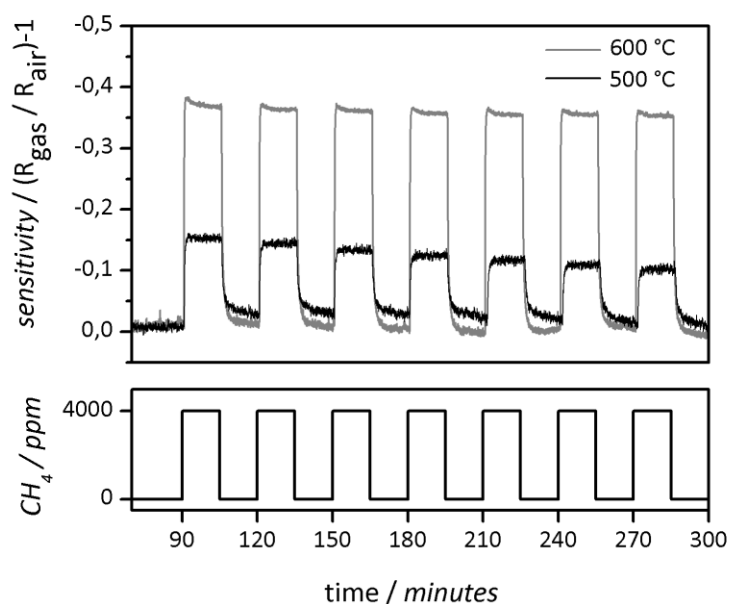


Figure 65. Gas sensing measurements of mesoporous SnO_2 towards methane (4000 ppm) at 500 and 600 °C.

The sensor shows a fast response and decay for both temperatures during repeated cycles of methane exposure and release at intervals of 15 minutes. The response time (t_{90}) was calculated as ca. 1.1 s for the sensor at a working temperature of 600 °C and as ca. 1.3 s for a temperature of 500 °C. At an operation temperature of 600 °C, the sensitivity is about 2.4 times higher in comparison to the experiment carried out at 500 °C. For both working temperatures a slight decrease in sensitivity is observed from cycle to cycle.

Further experiments were carried out with CO as test gas in technically relevant concentrations between 3 and 7 ppm (workplace exposure limit: 35 ppm) at intervals of 15 minutes with a sensor working temperature of 300 °C. *Figure 66* displays the results of the measurements.

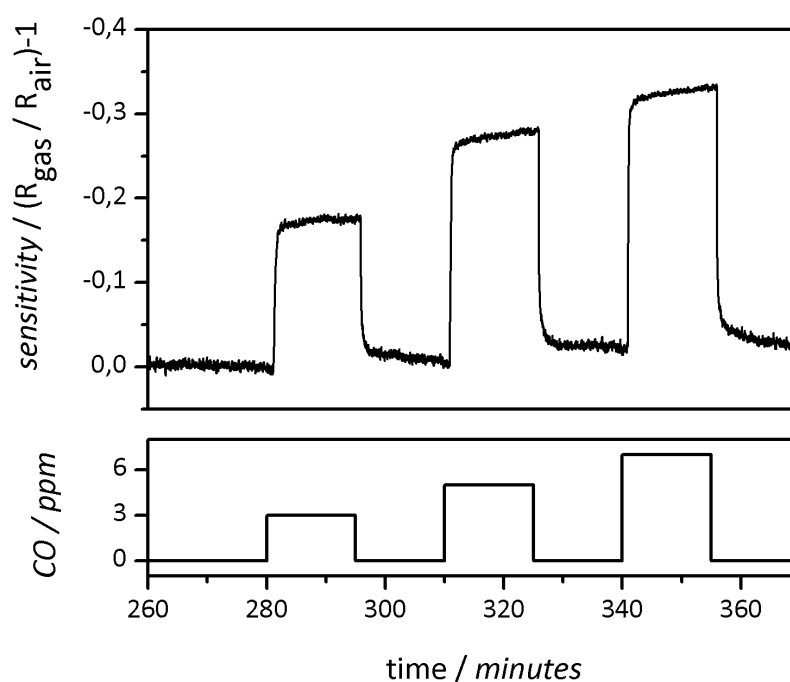


Figure 66. Gas sensing measurements of mesoporous SnO_2 towards CO with varying concentrations at 300 °C.

The sensor shows a fast response and decay towards the CO exposure and release for all concentrations; the t_{90} response time was estimated to ca. 1.7 s for 3 ppm CO, since a complete saturation was not obtained during the measure interval. Also for 5 and 7 ppm CO no complete saturation was observed, but the sensitivity of the sensor increases with higher CO concentration.

The high sensitivity towards methane as well as CO combined with the high thermal stability make mesoporous SnO_2 a promising material for high temperature gas detection.

7. Summary

The present thesis concerns the synthesis and characterization of three mesoporous semiconducting metal oxides ZnO, In_2O_3 and SnO_2 which possess large specific surface areas and ordered pore systems. Such systems are, due to their high surface-to-volume ratios, particularly of great interest in fields of catalysis, gas sensing and electrochemistry.

Generally two synthesis strategies are described in the recent literature which facilitate the approach to those systems by the utilization of templates. The application of supramolecular aggregates of amphiphilic molecules as structure-directing agents in the liquid phase enable primarily the synthesis of mesoporous silica materials, inorganic/organic hybrid materials as well as the fabrication of a few metal oxides. Owing to low synthesis temperatures and the low rigidity of these structure directors, that synthesis route is not transferable to the most metal oxide systems. Furthermore, the resulting materials are often amorphous and possess only a low temperature stability, which limit potential applications. The second synthesis strategy, nanocasting, avoid these disadvantages, originated from low synthesis temperatures, by the employment of rigid structure matrices with higher temperature stability. In case of the 'one-step nanocasting', the pores of a 3-D highly interconnected silica matrix are initially filled with a suitable metal oxide precursor species (frequently used: metal nitrates), followed by a thermal *in situ* conversion into the respective metal oxide. Finally, the structure matrix is removed by etching with HF or NaOH solution. Hence this route enables the synthesis of only those metal oxides, which withstand the template removal procedure. For those metal oxides which are not stable towards NaOH and HF, the utilization of mesoporous carbon as template represents a promising alternative, since they can easily be removed by combustion. The carbon matrices are generally synthesized using mesoporous silica as templates. In case of that 'two-step nanocasting' three problems become apparent: (i) impregnation of the highly hydrophobic carbon matrix with polar precursor species, (ii) the conversion into the oxide without structural loss of the carbon matrix and (iii) removal of the carbon template at high temperatures still retaining the structural integrity of the resultant metal oxide.

Within this thesis three distinct systems of mesoporous metal oxides were synthesized by nanocasting. Starting with ZnO, this system has been fabricated successfully by utilization of CMK-3 carbon as a template. Concerning the impregnation efficiency of the carbon matrix, a

microwave assisted surface modification of the template and the utilization of THF as solvent for the precursor ($\text{Zn}(\text{NO}_3)_2$) have been turned out to be beneficial. Optimum conditions for the conversion into the oxide as well as for the template removal were evaluated by TG-MS measurements. The yielded products possess an ordered pore system, a uniform pore size distribution and a specific surface area of $60 \text{ m}^2\cdot\text{g}^{-1}$, determined by nitrogen physisorption measurements. The mesostructure was additionally examined by low-angle P-XRD and TEM-analysis; the crystallinity (wurtzite) of the material was confirmed by wide-angle P-XRD and SAED. Furthermore, Raman- and PL-measurements were carried out for this system which also approved the crystallinity and the high surface-to-volume ratio. The material is polycrystalline with a domain size of ca. 7 nm. With regard to potential application as gas sensor this material exhibit promising properties. Experiments with oxidizing (NO_2) as well as reducing (CO) gases were accomplished in comparison to ZnO in the bulk phase. In both cases, the mesoporous material reveals a higher sensitivity.

The second successfully synthesized system concerns mesoporous In_2O_3 which was obtained with a hexagonal ($p6mm$) as well as a cubic ($la3d$) mesostructure dependent on the respective silica phases used as template. It was shown, that by utilization of templates with different topologies materials with distinct pore sizes, wall thicknesses and specific surface areas were yielded. All synthesized materials possess ordered pore systems, narrow pore size distributions and specific surface areas between 40 and $100 \text{ m}^2\cdot\text{g}^{-1}$ determined by nitrogen physisorption measurements. The mesoscopic order was further confirmed by low-angle P-XRD as well as TEM analysis. Concerning the crystalline nature of the material, the cubic bixbyite structure was identified by wide-angle P-XRD measurements with single-crystalline domains of ca. 30 – 40 nm, extending over several repeat distances of the pore size. The presence of such large single-crystalline domains was also confirmed by SAED experiments. Investigations concerning the temperature stability reveal that mesoporous In_2O_3 possess a high thermal stability without loss in mesostructure and specific surface area up to 450 °C. However, the synthesis of mesoporous In_2O_3 by utilization of mesoporous carbon serving as template was not successful since the temperature required for a complete template removal was evaluated by TG-MS to be significantly higher than 450 °C. The growth of In_2O_3 particles in mesoporous silica matrices was investigated by characterization of silica-free products after consecutive cycles of impregnation and oxide formation. This study revealed by analysis of low-angle P-XRD, physisorption and SEM that (i) the size of the obtained In_2O_3 particles differs

definitely from the templates' size even after several impregnations (the respective metal oxide particles are substantially smaller), (ii) the growth of the metal oxides inside the mesoporous matrix occurs predominantly along the pore axis rather than from pore wall to the center or vice versa and (iii) the morphology of the metal oxide particles differs substantially from those of the templates, which is basically a result of distinct interconnectivity of the pore channels. Highly branched KIT-6 silica as a template with an irregular morphology yield nearly spherical shaped metal oxide particles of uniform sizes. With SBA-15 silica as a template, characterized by a lower interconnectivity of the pore channels, In_2O_3 particles of ellipsoidal shape are obtained. It was shown, that (iv) in highly branched systems consecutive cycles of impregnation and oxide formation rather lead to the growth of already existing particles than to the formation of new particles and (v) the particle morphology as well as the growth of the particles are based on the presence of a liquid phase during the synthesis (metal nitrate solution or in the molten phase). Gas sensing measurements of the mesoporous In_2O_3 sensor material with distinct structural parameters (h , D_{lv} , A_{BET}) towards methane reveal a linear correlation between the specific surface area and the sensitivity, that increases significantly with increasing surface area. Further correlations were found between the surface area-normalized sensitivity and the pore size and the pore wall thickness, respectively. Further gas sensing experiments offered strong changes in resistance towards ozone. At a sensor working temperature of ca. 200 °C mesoporous In_2O_3 exhibit a significantly faster response time as well as a higher sensitivity towards ozone compared to non-porous In_2O_3 (bulk). Experiments carried out at room temperature also reveal that an ozone exposure causes a stronger change in resistance for the mesoporous sensor in comparison to the non-porous. However, the recovery time in case of the mesoporous sensor are substantially longer than those of the non-porous sensor. Finally, for both sensor materials an enhancement of the sensitivity and the recovery time could be obtained by irradiation of the sensor with a blue light during the detection process.

In case of mesoporous SnO_2 , the third successfully synthesized metal oxide system, cubic KIT-6 silica with small pores (7 nm) served as a template and SnCl_2 was used as SnO_2 precursor. Also here, the silica-free materials after consecutive cycles of impregnation and oxide formation were characterized by nitrogen physisorption, P-XRD, SEM and TEM. The obtained materials possess an ordered pore system with polycrystalline pore walls, which can be assigned to the tetragonal rutile structure (cassiterite). The specific surface areas of the respective mesoporous

materials are about $80 \text{ m}^2 \cdot \text{g}^{-1}$. In contrast to the above proposed model for the particle's growth (In_2O_3), in this case consecutive cycles of impregnation and oxide formation rather cause the formation of new SnO_2 particles inside the structure matrix, than a growth of already existing ones, which might be a result of a lower mobility of SnCl_2 precursor inside the pores. Moreover, mesoporous SnO_2 exhibit a high thermal stability up to 800°C without a substantially loss in structure. Due to that feature mesoporous SnO_2 is interesting for gas sensing, especially for the detection of those gases that combust at high temperatures. Concerning this matter, first experiments at high temperatures were accomplished with methane as test gas in technically relevant concentrations revealing that mesoporous SnO_2 is a promising candidate as a high-temperature gas sensor.

8. Outlook

Within this present thesis ordered mesoporous In_2O_3 and SnO_2 were successfully fabricated by the 'one-step nanocasting' under utilization of mesoporous SBA-15 and KIT-6 silica serving as rigid templates. Concerning the synthesis of mesoporous In_2O_3 detailed investigations revealed that a systematic variation of structural parameters like wall thickness, pore size, mesostructure, particle morphology and particle size is possible to some degree, *i.e.* by the choice of a definite silica template. Hence, future research activity might focus on the question, whether such a variation of structural parameters could be also transferred to further metal oxide systems finally resulting in a control of particle design. In this context it has to be clarified in detail, which parameters particularly influence the final features of the resultant metal oxide particles (precursor species, template etc.).

Another field of investigations might be, apart from the fabrication of further new metal oxides, the employment of other silica phases, distinct from SBA-15 and KIT-6 serving as a template, *e.g.*, cubic SBA-16 silica.

A promising alternative to the silica-nanocasting is given by the 'two-step nanocasting' utilizing mesoporous carbon as a template, which basically facilitates the access to metal oxides, that do not withstand a HF or NaOH treatment, like the previously presented ZnO system. However this concept can not be transferred to all metal oxide systems so far; this becomes apparent in case of the described In_2O_3 /CMK-3 system, at which the removal of the carbon matrix inevitably lead to a loss of the metal oxide's mesostructure due to the high temperature required for the CMK-3 combustion. For that reason methods have to be found, which enable the removal of the carbon matrix under mild conditions, *e.g.* by combustion in a CO_2 atmosphere or in distinct oxygen concentrations. Another interesting possibility avoiding a high heat quantity could be the utilization of porous carbon templates possessing a lower amount of carbon in the mesostructure thus thin carbon walls; in this context porous carbon phases like CMK-5 and CMK-9 have to be taken into account. In addition, the applicability of alternative templates, *e.g.* the phenol-formaldehyd polymers FDU-14 and FDU-15 materials also represents an interesting object of future works. These materials were not concerned for nanocasting so far but they seem to be promising candidates as rigid templates due to their high thermal stability and interconnected pore channels.

Concerning the application of mesoporous semiconducting metal oxides for gas sensing, the influence of the mesostructure, particle morphology and particle size on the sensor performance still remains to be investigated. Furthermore the effect, responsible for the enhanced sensitivity of mesoporous In_2O_3 caused by irradiation with blue light have to be clarified.

9. Zusammenfassung

Die vorliegende Arbeit beschäftigt sich mit der Synthese und Charakterisierung mesoporöser halbleitender Metalloxide, ZnO, In₂O₃ und SnO₂ mit geordneten Porensystemen. Systeme dieser Art finden aufgrund ihrer großen Oberflächen zu Volumenverhältnissen häufig Anwendung in der Katalyse, Gassensorik und Elektrochemie.

Generell werden in der Literatur zwei Synthesestrategien beschrieben, die unter Verwendung von Templaten den Zugang zu solchen Systemen ermöglichen. Der Einsatz supramolekularer Aggregate amphipiler Moleküle als Strukturdirigenten in flüssiger Phase ermöglicht vor allem den Zugang zu mesoporösen Silica-Materialien, anorganisch/organischen Hybridmaterialien, sowie auch die Synthese einiger weniger Metalloxide. Aufgrund niedriger Synthesetemperaturen und der fehlenden Rigidität dieser Strukturdirigenten ist die Verwendung solcher weichen Template nicht auf alle Metalloxidsysteme übertragbar. Darüber hinaus sind die erhaltenen Materialien meist amorph und wenig temperaturstabil, was potentielle Anwendungen limitiert. Die zweite Synthesestrategie, die Nanocasting-Strategie, umgeht unter Verwendung rigider, temperaturstabiler Strukturmatrizes die Nachteile niedriger Synthesetemperaturen. Im so genannten 'one-step nanocasting' werden die Porenkanäle dreidimensional vernetzter Silica-Template mit einem Metalloxidpräcursor (meist Metallnitrat) gefüllt und anschließend in einem thermischen Prozess *in situ* in das Metalloxid überführt. Das Templat wird abschließend mit HF oder NaOH aufgelöst. Für diese Synthesestrategie kommen daher nur Metalloxide in Frage, welche die Prozedur zur Templatentfernung überstehen. Für Materialien, welche diesen chemisch harschen Bedingungen nicht widerstehen, bietet sich die Synthese über Kohlenstofftemplate an, die ihrerseits negative Replika von Silicatemplaten sind. Nach Imprägnierung und Oxidbildung kann der Kohlenstoff durch Verbrennung entfernt werden, so dass ein Positivabdruck der originären Silica-Matrix entsteht (so genanntes 'two step nanocasting'). Bei dieser Syntheseroute ergeben sich *a priori* drei Herausforderungen: (i) Die Imprägnierung der stark hydrophoben Kohlenstoffmatrix mit polaren Metalloxidprecursoren, (ii) die Überführung in das Oxid ohne Strukturverlust der Kohlenstoffmatrix und (iii) die Entfernung der Kohlenstoffmatrix (bei hohen Temperaturen) ohne Strukturverlust der Metalloxidmatrix.

Im Rahmen dieser Arbeit wurden drei mesoporöse Metalloxide über die Nanocasting-Strategie hergestellt. Das erste System, ZnO, wurde erfolgreich über die Verwendung von mesoporösem CMK-3 Kohlenstoff als Templat hergestellt. Im Hinblick auf die Imprägnierung der Kohlenstoffmatrix hat sich eine mikrowellenunterstützte Oberflächenmodifizierung des Templates und die Verwendung von THF als Lösungsmittel für den Präcursor ($\text{Zn}(\text{NO}_3)_2$) als günstig erwiesen. Optimale Bedingungen für die Oxidbildung und die Templatentfernung wurden mittels TG-MS Messungen ermittelt. Das schließlich erhaltene Material verfügt über geordnete Porenkanäle, eine einheitliche Porengrößenverteilung und eine spezifische Oberfläche von $60 \text{ m}^2\cdot\text{g}^{-1}$, was mittels Stickstoffphysisorption ermittelt wurde. Die mesoskopische Ordnung wurde weiterhin durch Kleinwinkel P-XRD und durch TEM-Analysen nachgewiesen. Die Kristallinität (Wurtzit) des Materials wurde standardmäßig mittels Weitwinkel P-XRD und SAED bestätigt. Zusätzlich wurden für dieses System Raman- und PL-Messungen durchgeführt, welche die Kristallinität sowie das große Oberflächen zu Volumenverhältnis bestätigten. Der Aufbau des Materials kann als polykristallin beschrieben werden, mit Kristallitgrößen von etwa 7 nm. Im Hinblick auf potentielle Anwendungen als Gassensor zeigt das Material viel versprechende Eigenschaften. Hierzu wurden, vergleichend mit ZnO in der Volumenphase („bulk“), Messungen in oxidierender (NO_2) und reduzierender Gasatmosphäre (CO) durchgeführt. In beiden Fällen zeigt das mesoporöse Material eine höhere Sensitivität.

Das zweite erfolgreich synthetisierte System ist In_2O_3 . Hierbei konnten durch verschiedene Silica-Phasen Materialien mit unterschiedlicher Mesostruktur, hexagonal ($p6mm$) und kubisch ($la3d$), hergestellt werden. Es konnte gezeigt werden, dass die Verwendung unterschiedlicher Topologien der Template Materialien mit variierenden Porendurchmessern, Wandstärken und Oberflächen liefert. Alle synthetisierten Materialien verfügen über geordnete Porenkanäle, enge Porenradienverteilungen und spezifische Oberflächen zwischen 40 und $100 \text{ m}^2\cdot\text{g}^{-1}$, was mittels Stickstoffphysisorption nachgewiesen wurde. Die mesoskopische Ordnung konnte weiterhin durch Kleinwinkel P-XRD sowie TEM-Analysen bestätigt werden. Bezüglich des kristallinen Aufbaus der Materialien konnte die kubische Bixbyite-Struktur mittels P-XRD Messungen nachgewiesen werden, wobei einkristalline Domänen von etwa 30 - 40 nm Größe berechnet wurden und sich somit über ein Vielfaches des Porendurchmessers erstrecken. Das Vorhandensein größerer einkristalliner Domänen, wurde weiterhin durch SAED Experimente bestätigt. Zusätzlich wurden Experimente zur Temperaturstabilität von mesoporösem In_2O_3

durchgeführt. Hierbei wurde festgestellt, dass das Material über eine vergleichsweise hohe thermische Stabilität verfügt; es wurden keine deutlichen Änderungen der Mesostruktur und der Größe der spezifischen Oberflächen unterhalb von 450 °C beobachtet. Trotz dieser relativ hohen Temperaturstabilität konnte In_2O_3 in mesostrukturierter Form nicht über das Kohlenstoff-Nanocasting hergestellt werden, da die zur Templatentfernung ermittelten Temperaturen (TG-MS), deutlich über 450 °C liegen. Das Wachstum von In_2O_3 Partikeln in porösen Silica-Matrizes wurde durch Charakterisierung der Silica-freien Produkte nach jedem Zyklus von Imprägnierung und anschließender Oxidbildung näher untersucht. Hierbei konnte mittels Kleinwinkel P-XRD, Physisorption und REM-Untersuchungen festgestellt werden, dass:

- (i) Die Größe der resultierenden Partikel, auch nach mehrfachen Imprägnierungen, sich deutlich von der der Template unterscheidet (die resultierenden Metalloxidpartikel sind in allen Fällen signifikant kleiner),
- (ii) die Metall-oxide in den porösen Matrizes eher entlang der Porenachse wachsen anstatt von der Porenwand zur Porenmitte und umgekehrt und
- (iii) die Morphologie der Metalloxidpartikel stark von der der Template abweicht und vor allem durch den Verzweigungsgrad und die Interkonnektivität beeinflusst wird.

Hoch verzweigtes KIT-6 Silica mit irregulärer Partikelmorphologie führt zu annähernd sphärischen Metalloxidpartikeln einheitlicher Größe, unverzweigte und schwach interkonnektierte Porenkanäle des SBA-15 Silica hingegen zu Partikeln mit ellipsoidaler Form. Weiterhin führen (iv) in hoch verzweigten Systemen aufeinander folgende Zyklen von Imprägnierung und Oxidbildung eher zum Wachstum bereits bestehender Metalloxidpartikel als zur Bildung neuer und (v) die Partikelmorphologien, sowie das Wachstum der Partikel sind auf das Vorliegen einer flüssigen Phase (Nitratlösung oder geschmolzenes Nitrat) während der Synthese zurückzuführen. Weiterhin durchgeführte gassensorische Messungen mit Materialien variierender struktureller Parameter (h , D_h , A_{BET}) gegenüber Methan ergaben eine lineare Abhängigkeit der Sensitivität von der Größe der spezifischen Oberfläche des Sensormaterials; diese steigt signifikant mit Zunahme der Oberfläche an. Darüber hinaus konnten sowohl Korrelationen zwischen der oberflächennormierten Sensitivität und dem Porendurchmesser, als auch mit der Wandstärke beobachtet werden. Des Weiteren konnten sehr starke Änderungen des Sensorwiderstands gegenüber Ozon festgestellt werden. Mesoporöses In_2O_3 zeigt bei einer Arbeitstemperatur von etwa 200 °C deutlich schnellere Ansprechzeiten und eine höhere Sensitivität gegenüber Ozon in einer Konzentration von 1.2 ppm als das getestete Referenzmaterial (In_2O_3 , Bulk). Experimente bei Raumtemperatur weisen ebenfalls eine stärkere Widerstandsänderung des

mesoporösen Sensors gegenüber Ozon auf als der des unporösen. Die Erholungszeiten des porösen Sensors sind im Vergleich zum unporösen jedoch deutlich länger. Sowohl die Sensitivität als auch die Erholungszeiten konnten durch Bestrahlung der Sensorfläche mit blauem Licht während des Detektionsvorganges bei beiden Materialien verbessert werden.

Mesoporöses SnO_2 ist das dritte erfolgreich synthetisierte System. Als Templat diente kubisches KIT-6 Silica mit kleinen Poren (7 nm) und SnCl_2 als SnO_2 Präcursor. Auch bei diesem System wurden die Silica-freien Materialien nach jedem Zyklus von Imprägnierung und anschließender Oxidbildung mittels Stickstoffphysisorption, P-XRD, REM und SEM charakterisiert. Alle Materialien verfügen über ein geordnetes Porensystem mit polykristallinen Porenwänden, die der SnO_2 typischen tetragonalen Rutil-Struktur (Cassiterite) zugeordnet werden können. Die Oberflächen der erhaltenen mesoporösen Materialien betragen ca. $80 \text{ m}^2 \cdot \text{g}^{-1}$. Im Gegensatz zum zuvor beschriebenen Partikelwachstumsmodell (In_2O_3) erfolgt bei aufeinander folgenden Zyklen von Imprägnierung und Oxidbildung eher eine Bildung neuer SnO_2 Partikel in den Strukturmatrices, als ein Wachstum bereits bestehender Partikel, was auf eine geringere Mobilität, des SnCl_2 -Präcursors in den Poren zurückzuführen sein könnte. Des Weiteren verfügt mesoporöses SnO_2 über eine hohe thermische Stabilität, so dass bei durchgeführten Temperaturstabilitätsexperimenten bis 800°C kein deutlicher Verlust der strukturellen zu verzeichnen war. Diese Eigenschaft macht mesoporöses SnO_2 für Anwendungen in der Gassensorik interessant, insbesondere zur Detektion von Gasen, die bei hohen Temperaturen verbrennen. Diesbezüglich wurden u. a. erste Hochtemperaturmessungen mit Methan als Analytgas in technisch relevanten Konzentrationen durchgeführt, die eine viel versprechende Eignung dieses Material als Hochtemperatur-Gassensor erkennen lassen.

10. Literature

- [1] K. S. W. Sing, D. H. Everett, R. A. W. Haul, L. Moscou, R. A. Pierotti, J. Rouquerol, T. Siemieniewska, *Pure & Appl. Chem.* **1985**, *57*, 603.
- [2] C. Baerlocher, W. M. Meier, D. H. Olsen, Elsevier, Amsterdam, **2001**.
- [3] M. Tiemann, *Chem. Mater.* **2008**, *20*, 961.
- [4] F. Schüth, *Angew. Chem. Int. Ed.* **2003**, *42*, 3604.
- [5] Y. Wan, D. Zhao, *Chem. Rev.* **2007**, *107*, 2821.
- [6] H. P. Lin, S. F. Cheng, C. Y. Mou, *Journal of the Chinese Chemical Society* **1996**, *43*, 375.
- [7] V. R. Choudhary, S. D. Sansare, *Proceedings of the Indian Academy of Sciences-Chemical Sciences* **1997**, *109*, 229.
- [8] K. Cassiers, T. Linssen, M. Mathieu, M. Benjelloun, K. Schrijnemakers, P. Van Der Voort, P. Cool, E. F. Vansant, *Chemistry of Materials* **2002**, *14*, 2317.
- [9] P. Selvam, S. K. Bhatia, C. G. Sonwane, *Ind. Eng. Chem. Res.* **2001**, *40*, 3237.
- [10] D. Y. Zhao, Q. S. Huo, J. L. Feng, B. F. Chmelka, G. D. Stucky, *J. Am. Chem. Soc.* **1998**, *120*, 6024.
- [11] F. Hoffmann, M. Cornelius, J. Morell, M. Fröba, *Angew. Chem. Int. Ed.* **2006**, *45*, 3216.
- [12] G. S. Attard, J. C. Glyde, C. G. Göltner, *Nature* **1995**, *378*, 366.
- [13] A. Monnier, F. Schuth, Q. Huo, D. Kumar, D. Margolese, R. S. Maxwell, G. D. Stucky, M. Krishnamurty, P. Petroff, A. Firouzi, M. Janicke, B. F. Chmelka, *Science* **1993**, *261*, 1299.
- [14] Y. Meng, D. Gu, F. Zhang, Y. Shi, H. Yang, Z. Li, C. Yu, B. Tu, D. Zhao, *Angew. Chem. Int. Ed.* **2005**, *44*, 7053.
- [15] Y. Meng, D. Gu, F. Zhang, Y. Shi, L. Cheng, D. Feng, Z. Wu, Z. Chen, Y. Wan, A. Stein, D. Zhao, *Chem. Mater.* **2006**, *18*, 4447.
- [16] F. Zhang, Y. Meng, D. Gu, Y. Yan, C. Yu, B. Tu, D. Zhao, *J. Am. Chem. Soc.* **2005**, *127*, 13508.
- [17] B. T. Holland, C. F. Blanford, T. Do, A. Stein, *Chem. Mater.* **1999**, *11*, 795.
- [18] K. Schwarz, M. Eppe, *Macromol. Rapid Commun.* **1998**, *19*, 613.
- [19] M. Eppe, L. Tröger, *J. Chem. Soc., Dalton Trans.* **1996**, 11.
- [20] M. Eppe, O. Herzberg, *J. Mater. Chem.* **1997**, *7*, 1037.
- [21] F. Schüth, *Chem. Mater.* **2001**, *13*, 3184.

- [22] P. Yang, D. Zhao, D. I. Margolese, B. F. Chmelka, G. D. Stucky, *Chem. Mater.* **1999**, *11*, 2813.
- [23] D. M. Antonelli, J. Y. Ying, *Angew. Chem. Int. Ed.* **1995**, *34*, 2014.
- [24] T. Brezesinski, J. Wang, J. Polleux, B. Dunn, S. H. Tolbert, *J. Am. Chem. Soc.* **2009**, *131*, 1802.
- [25] T. Wagner, C.-D. Kohl, M. Fröba, M. Tiemann, *Sensors* **2006**, *6*, 318.
- [26] D. M. Antonelli, J. Y. Ying, *Chem. Mater.* **1996**, *8*, 3126.
- [27] U. Ciesla, M. Fröba, G. Stucky, F. Schüth, *Chem. Mater.* **1999**, *11*, 227.
- [28] T. Katou, B. Lee, D. Lu, J. N. Kondo, M. Hara, K. Domen, *Angew. Chem. Int. Ed.* **2003**, *42*, 2382.
- [29] D. G. Shchukin, J. H. Schattka, M. Antonietti, R. A. Caruso, *Journal of Physical Chemistry B* **2003**, *107*, 952.
- [30] J. Roggenbuck, G. Koch, M. Tiemann, *Chem. Mater.* **2006**, *18*, 4151.
- [31] B. Z. Tian, S. N. Che, Z. Liu, X. Y. Liu, W. B. Fan, T. Tatsumi, O. Terasaki, D. Zhao, *Chem. Commun.* **2003**, 2726.
- [32] J. Parmentier, L. A. Solovyov, F. Ehrburger-Dolle, J. Werckmann, O. Ersen, F. Bley, J. Patarin, *Chem. Mater.* **2006**, *18*, 6316.
- [33] L. A. Solovyov, V. I. Zaikovskii, A. N. Shmakov, O. V. Belousov, R. Ryoo, *Journal of Physical Chemistry B* **2002**, *106*, 12198.
- [34] M. Kruk, M. Jaroniec, R. Ryoo, S. H. Joo, *Journal of Physical Chemistry B* **2000**, *104*, 7960.
- [35] A. Galarneau, H. Cambon, F. Di Renzo, R. Ryoo, M. Choib, F. Fajulaa, *New J. Chem.* **2003**, *27*, 73.
- [36] T.-W. Kim, F. Kleitz, B. Paul, R. Ryoo, *J. Am. Chem. Soc.* **2005**, *127*, 7601.
- [37] B. Tian, X. Liu, H. Yang, S. Xie, C. Yu, B. Tu, D. Zhao, *Adv. Mater.* **2003**, *15*, 1370.
- [38] S. C. Laha, R. Ryoo, *Chem. Commun.* **2003**, 2138.
- [39] E. Rossinyol, J. Arbiol, F. Peiro, A. Cornet, J. R. Morante, B. Tian, T. Bob, D. Zhao, *Sens. Actuators, B* **2005**, *109*, 57.
- [40] W. Yue, W. Zhou, *Chem. Mater.* **2007**, *19*, 2359.
- [41] T. Wagner, J. Roggenbuck, C.-D. Kohl, M. Fröba, M. Tiemann, *Stud. Surf. Sci. Catal.* **2007**, *165*, 347.

-
- [42] P. Shu, J. F. Ruan, C. B. Gao, H. C. Li, S. N. Che, *Microporous and Mesoporous Materials* **2009**, *123*, 314.
- [43] C. Dickinson, W. Zhou, R. P. Hodgkins, Y. Shi, D. Zhao, H. He, *Chem. Mater.* **2006**, *18*, 3088.
- [44] W. Zhou, K. Zhu, B. Yue, H. He, C. Dickinson, *Stud. Surf. Sci. Catal* **2004**, *154*, 924.
- [45] M. Imperor-Clerc, D. Bazin, M.-D. Appay, P. Beaunier, A. Davidson, *Chem. Mater.* **2004**, *16*, 1813.
- [46] J. K. Shon, S. S. Kong, Y. S. Kim, J.-H. Lee, W. K. Park, S. C. Park, J. M. Kim, *Microporous Mesoporous Mater.* **2009**, *120*, 441.
- [47] B. Liu, R. T. Baker, *Journal of Materials Chemistry* **2008**, *18*, 5200.
- [48] W. Shen, X. Dong, Y. Zhu, H. Chen, J. Shi, *Microporous Mesoporous Mater.* **2005**, *85*, 157.
- [49] Y. Q. Wang, C. M. Yang, W. Schmidt, B. Spliethoff, E. Bill, F. Schüth, *Adv. Mater.* **2005**, *17*, 53.
- [50] F. Jiao, A. Harrison, J. C. Jumas, A. V. Chadwick, W. Kockelmann, P. G. Bruce, *Journal of the American Chemical Society* **2006**, *128*, 5468.
- [51] H. Yang, Q. Shi, B. Tian, Q. Lu, F. Gao, S. Xie, J. Fan, C. Yu, B. Tu, D. Zhao, *J. Am. Chem. Soc.* **2003**, *125*, 4724.
- [52] T. Waitz, T. Wagner, T. Sauerwald, C.-D. Kohl, M. Tiemann, *Adv. Funct. Mater.* **2008** *19*, 653.
- [53] W. H. Shen, J. L. Shi, H. R. Chen, J. L. Gu, Y. F. Zhu, X. P. Dong, *Chem. Lett.* **2005**, *34*, 390.
- [54] J.-H. Smått, C. Weidenthaler, J. B. Rosenholm, M. Lindén, *Chem. Mater.* **2006**, *18*, 1443.
- [55] J. H. Smatt, N. Schuwer, M. Jarn, W. Lindner, M. Linden, *Microporous and Mesoporous Mater.* **2008**, *112*, 308.
- [56] X. Liu, B. Tian, C. Yu, B. Tu, Z. Liu, O. Terasaki, D. Zhao, *Chem. Lett.* **2003**, *32*, 824.
- [57] F. Gao, Q. Lu, D. Zhao, *Adv. Mater.* **2003**, *15*, 739.
- [58] Y. Shi, Y. Wan, R. Liu, B. Tu, D. Zhao, *J. Am. Chem. Soc.* **2007**, *129*, 9522.
- [59] Z. Yang, Y. Xia, R. Mokaya, *Chem. Mater.* **2004**, *16*, 3877.
- [60] Y. Shi, Y. Meng, D. Chen, S. Cheng, P. Chen, H. Yang, Y. Wan, D. Zhao, *Adv. Funct. Mater.* **2006**, *16*, 561.

- [61] Y. J. Han, J. M. Kim, G. D. Stucky, *Chem. Mater.* **2000**, *12*, 2068.
- [62] H. Kang, Y. W. Jun, J. I. Park, K. B. Lee, J. Cheon, *J. Chem. Mater.* **2000**, *12*, 3530.
- [63] R. Ryoo, C. H. Ko, M. Kruk, V. Antochshuk, M. Jaroniec, *J. Phys. Chem. B* **2000**, *104*, 11465.
- [64] R. Ryoo, S. H. Joo, S. Jun, *J. Phys. Chem. B* **1999**, *103*, 7743.
- [65] J. Lee, S. Yoon, T. Hyeon, O. S. M., K. B. Kimb, *Chem. Commun.* **1999**, 2177.
- [66] S. Jun, S. H. Joo, R. Ryoo, M. Kruk, M. Jaroniec, Z. Liu, T. Ohsuna, O. Terasaki, *J. Am. Chem. Soc.* **2000**, *122*, 10712.
- [67] F. Kleitz, S. H. Choi, R. Ryoo, *Chem. Commun.* **2003**, 2136.
- [68] R. Ryoo, S. H. Joo, M. Kruk, M. Jaroniec, *Adv. Mater.* **2001**, *13*, 677.
- [69] S. H. Joo, S. J. Choi, I. Oh, J. Kwak, Z. Liu, O. Terasaki, R. Ryoo, *Nature* **2001**, *414*, 470.
- [70] S. N. Che, K. Lund, T. Tatsumi, S. Iijima, S. H. Joo, R. Ryoo, O. Terasaki, *Angew. Chem. Int. Ed.* **2003**, *42*, 2182.
- [71] F. Kleitz, S. H. Choi, R. Ryoo, *Chem. Commun.* **2003**, 2136.
- [72] J. Lee, J. Kim, T. Hyeon, *Adv. Mater.* **2006**, *18*, 2073.
- [73] A.-H. Lu, W. Schmidt, A. Taguchi, B. Spliethoff, B. Tesche, F. Schüth, *Angew. Chem. Int. Ed.* **2002**, *41*, 3489.
- [74] M. Kang, S. H. Yi, H. I. Lee, J. E. Yie, J. M. Kim, *Chem. Commun.* **2002**, 1944.
- [75] J. Roggenbuck, M. Tiemann, *J. Am. Chem. Soc.* **2005**, *127*, 1096.
- [76] Q. Liu, A. Wang, X. Wang, T. Zhang, *Chem. Mater.* **2006**, *18*, 5153.
- [77] Q. Liu, A. Q. Wang, J. M. Xu, Y. H. Zhang, X. D. Wang, T. Zhang, *Microporous and Mesoporous Mater.* **2008**, *116*, 461.
- [78] T. Tsoncheva, J. Roggenbuck, M. Tiemann, L. Ivanova, D. Paneva, I. Mitov, C. Minchev, *Microporous Mesoporous Mater.* **2008**, *110*, 339.
- [79] J. Roggenbuck, H. Schäfer, T. Tsoncheva, C. Minchev, J. Hanss, M. Tiemann, *Microporous Mesoporous Mater.* **2007**, *101*, 335.
- [80] X. Lai, X. Li, W. Geng, J. Tu, J. Li, S. Qiu, *Angew. Chem. Int. Ed.* **2007**, *46*, 738.
- [81] A.-H. Lu, W. Schmidt, B. Spliethoff, F. Schüth, *Chem. Eur. J.* **2004**, *10*, 6085.
- [82] L. Wang, K. Lin, Y. Di, D. Zhang, C. Li, Q. Yang, C. Yin, Z. Sun, D. Jiang, F.-S. Xiao, *Microporous Mesoporous Mater.* **2005**, *86*, 81.
- [83] T. Waitz, M. Tiemann, P. J. Klar, J. Sann, J. Stehr, B. K. Meyer, *Appl. Phys. Lett.* **2007**, *90*, 123108.

- [84] T. Wagner, T. Waitz, J. Roggenbuck, M. Fröba, C.-D. Kohl, M. Tiemann, *Thin Solid Films* **2007**, *515*, 8360.
- [85] S. Polarz, A. V. Orlov, F. Schüth, A.-H. Lu, *Chem. Eur. J.* **2007**, *13*, 592.
- [86] A.-H. Lu, W. C. Li, W. Schmidt, F. Schüth, *Microporous Mesoporous Mater.* **2006**, *95*, 187.
- [87] J. Roggenbuck, T. Waitz, M. Tiemann, *Microporous Mesoporous Mater.* **2008**, *113*, 575.
- [88] P. G. Bruce, B. Scrosati, J. M. Tarascon, *Angew. Chem. Int. Ed.* **2008**, *47*, 2930.
- [89] M. Tiemann, *Chem. Eur. J.* **2007**, *13*, 8376.
- [90] J. Q. Xu, Q. Y. Pan, Y. A. Shun, Z. Z. Tian, *Sensors and Actuators B* **2000**, *66*, 277.
- [91] C. Y. Lu, S. P. Chang, S. J. Chang, T. J. Hsueh, C. L. Hsu, Y. Z. Chiou, C. Chen, *Ieee Sensors Journal* **2009**, *9*, 485.
- [92] P. C. Xu, Z. X. Cheng, Q. Y. Pan, J. Q. Xu, Q. Xiang, W. J. Yu, Y. L. Chu, *Sensors and Actuators B* **2008**, *130*, 802.
- [93] C. Y. Wang, V. Cimalla, T. Kups, C.-C. Röhlig, T. Stauden, O. Ambacher, M. Kunzer, T. Passow, W. Schirmacher, W. Pletschen, K. Köhler, J. Wagner, *Appl. Phys. Lett.* **2007**, *91*, 103509.
- [94] C. Y. Wang, M. Ali, T. Kups, C. C. Rohlig, V. Cimalla, T. Stauden, O. Ambacher, *Sensors and Actuators B* **2008**, *130*, 589.
- [95] H. C. Chiu, C. S. Yeh, *Journal of Physical Chemistry C* **2007**, *111*, 7256.
- [96] K. S. W. Sing, R. T. Williams, *Adsorption Science & Technology* **2004**, *22*, 773.
- [97] K. S. W. Sing, *Journal of Porous Materials* **1995**, *2*, 5.
- [98] S. Brunauer, P. H. Emmet, E. Teller, *J. Am. Chem. Soc.* **1938**, *60*, 309.
- [99] E. P. Barrett, L. G. Joyner, P. P. Halenda, *J. Am. Chem. Soc.* **1951**, *73*, 373.
- [100] P. I. Ravikovitch, A. V. Neimark, *Journal of Physical Chemistry B* **2001**, *105*, 6817.
- [101] A. V. Neimark, P. I. Ravikovitch, in *2nd International Symposium on Mesoporous Molecular Sieves (ISMMS)*, Elsevier Science Bv, Quebec City, Canada, **2000**, pp. 697.
- [102] C.-D. Kohl, *J. Phys. D: Appl. Phys.* **2001**, *34*, R125.
- [103] A. Gurlo, R. Riedel, *Angew. Chem. Int. Ed.* **2007**, *46*, 3826.
- [104] C. Xu, J. Tamaki, N. Miura, N. Yamazoe, *Sensors and Actuators B-Chemical* **1991**, *3*, 147.
- [105] A. Rothschild, Y. Komem, *Journal of Applied Physics* **2004**, *95*, 6374.
- [106] C. Klingshirn, *Chemphyschem* **2007**, *8*, 782.

-
- [107] D. Zhao, J. Feng, Q. Huo, N. Melosh, G. H. Fredrickson, B. F. Chmelka, G. D. Stucky, *Science* **1998**, 279, 548.
- [108] F. F. Pasquale, P. Stanislaw, J. Mietek, *J. Mater. Chem.* **2005**, 15, 5049.
- [109] A. B. Fuertes, *Microporous Mesoporous Mater.* **2004**, 67, 273.
- [110] *Handbook of Chemistry and Physics*, 87 ed., CRC Press, Boca Raton, **2006**.
- [111] L. F. Wang, S. Lin, K. F. Lin, C. Y. Yin, D. S. Liang, Y. Di, P. W. Fan, D. Z. Jiang, F. S. Xiao, *Microporous and Mesoporous Mater.* **2005**, 85, 136.
- [112] A. Vinu, P. Srinivasu, M. Takahashi, T. Mori, V. V. Balasubramanian, K. Ariga, *Microporous and Mesoporous Mater.* **2007**, 100, 20.
- [113] P. D. C. King, T. D. Veal, F. Fuchs, C. Y. Wang, D. J. Payne, A. Bourlange, H. Zhang, G. R. Bell, V. Cimalla, O. Ambacher, R. G. Egdell, F. Bechstedt, C. F. McConville, *Physical Review B* **2009**, 79, 10.
- [114] A. Ruplecker, F. Kleitz, E. L. Elena-Lorena Salabas, F. Schüth, *Chem. Mater.* **2007**, 19, 485.
- [115] J. C. Groen, P. L. A. A., J. Perez-Raimirez, *Microporous Mesoporous Mater.* **2003**, 60, 1.
- [116] *Handbook of Biosensors and Electronic Noses: Medicine, Food & the Environment*, CRC Press, Boca Raton, **1996**.
- [117] G. J. Li, X. H. Zhang, S. Kawi, *Sensors and Actuators B* **1999**, 60, 64.
- [118] G. J. Li, S. Kawi, *Materials Letters* **1998**, 34, 99.
- [119] G. Sakai, N. Matsunaga, K. Shimano, N. Yamazoe, *Sensors and Actuators B* **2001**, 80, 125.
- [120] N. Yamazoe, *Sensors and Actuators B-Chemical* **1991**, 5, 7.
- [121] P. P. Zhang, E. Tevaarwerk, B. N. Park, D. E. Savage, G. K. Celler, I. Knezevic, P. G. Evans, M. A. Eriksson, M. G. Lagally, *Nature* **2006**, 439, 703.
- [122] K. D. Schierbaum, U. Weimar, W. Gopel, R. Kowalkowski, *Sens. Actuators B* **1990**, 3, 205.
- [123] J. F. McAleer, P. T. Moseley, J. O. W. Norris, D. E. Williams, *Journal of the Chemical Society-Faraday Transactions I* **1987**, 83, 1323.
- [124] E. Comini, G. Faglia, G. Sberveglieri, *Sens. Actuators B* **2001**, 78, 73.
- [125] E. Comini, A. Cristalli, G. Faglia, G. Sberveglieri, *Sens. Actuators B* **2000**, 65, 260.

-
- [126] G. Faglia, C. Baratto, E. Comini, G. Sberveglieri, M. Zha, A. Zappettini, in *IEEE Sensors 2004 Conference* (Eds.: D. Rocha, P. M. Sarro, M. J. Vellekoop), Ieee, Vienna, AUSTRIA, **2004**, pp. 182.
- [127] M. E. Bowden, *J. Mater. Sci. Lett.* **1990**, *9*, 735.
- [128] B. Ceric, P. Bukovec, *Thermochimica Acta* **1992**, *195*, 73.
- [129] B. K. Min, S. D. Choi, in *10th International Meeting on Chemical Sensors*, Elsevier Science Sa, Tsukuba, JAPAN, **2004**, pp. 119.
- [130] E. R. Leite, T. R. Giraldi, F. M. Pontes, E. Longo, A. Beltran, J. Andres, *Applied Physics Letters* **2003**, *83*, 1566.

Part IV – Appendix

Chemiekalienverzeichnis

SUBSTANZ	GEFAHRENSYMBOL	R-SÄTZE	S-SÄTZE
1-Butanol	Xn	10-22-37/38-41-67	7/9-13-26-37/39-46
Ethanol	F	11	7-16
Flusssäure	T+, C	26/27/28-35	7/9-26-28.1-36/37/39-45
Indium(III)-nitrat-Pentahydrat (p.a.)	O, Xn	8-20/21/22	17-26-27-36/37/39
Pluronic-P123©	-	-	23-24/25
Saccharose			
Salpetersäure 65 % (p.a.)	C	35	23-26-36/37/39-45
Salzsäure 32 % (p.a.)	C	34-37	26-36/37/39-45
Schwefelsäure (96 %)	C	35	26-30-45
Tetraethylorthosilicat (zur Synthese)	Xn	10-20-36/37	-
Tetrahydrofuran (p. a.)	F, Xi	11-19-36/37	16-29-33
Wasserstoffperoxid, 30 % (stabilisiert, zur Synthese)	Xn	22-41	26-39
Zinn(II)-chlorid-Dihydrat (p.a.)	C	22-36/37/38	26
Zink(II)-nitrat-Hexahydrat (p. a.)	O, Xn, N	8-22-36/37/38-50/53	26-61

Lebenslauf von Thomas Waitz

PERSÖNLICHE DATEN

- Geburtstag: 07.08.1979
- Geburtsort: Temeschburg
- Familienstand: ledig
- Staatsangehörigkeit: deutsch

AUSBILDUNG

- 1986 - 1989 Grundschule Gießen-West
- 1989 - 1990 Grundschule Launsbach
- 1990 - 1992 Ludwig-Uhland-Schule Gießen
- 1992 - 1999 Liebigschule-Gießen; Abschluss: Abitur
- 10/2000 - 05/2005 Lehramtsstudium an der Justus-Liebig-Universität Gießen mit den Fächern Sport und Chemie; Titel der Examensarbeit: *Effekte elektrischer Muskelstimulation auf Parameter der Reaktivkraft*; Abschluss: Erstes Staatsexamen für das Lehramt an Gymnasien
- seit 6/2005 Promotionsstudium an der Justus-Liebig-Universität Gießen am Institut für Anorganische und Analytische Chemie; Titel des Dissertation: *Ordered Mesoporous Metal Oxides by Structure Replication: Synthesis, Characterization and Gas Sensing*
- 08/2005 - 8/2007 Referendariat am Studienseminar Gießen, Ausbildungsschule: Landgraf-Ludwigs-Gymnasium; Titel der Examensarbeit: *Eigendiagnostische Fähigkeiten im Kontext differenzierten Übens am Beispiel einer Unterrichtseinheit Säuren-Laugen-Salze*; Abschluss: Zweites Staatsexamen für das Lehramt an Gymnasien

BERUFLICHER WERDEGANG

- seit 08/2007 Beamter zur Anstellung, Schulamt Gießen; Dienststelle:
Landgraf-Ludwigs-Gymnasium
- seit 02/2009 Beamter auf Lebenszeit, Schulamt Gießen; Dienststelle:
Landgraf-Ludwigs-Gymnasium
- seit 08/2009 Abordnung an das Institut für Didaktik der Chemie Justus-
Liebig-Universität Gießen

WEHRERSATZDIENST

- 07/1999 - 06/2000 Frauenklinik der Justus-Liebig-Universität Gießen

Publikationen

FACHWISSENSCHAFTLICHE JOURNALS

- Mesoporous In_2O_3 with Regular Morphology by Nanocasting: A Simple Relation between Particle Shape and Growth Mechanism
S. Haffer, T. Waitz, M. Tiemann
submitted
- Aliphatic C–H Bond Oxidation of Toluene Using Copper Peroxo Complexes That Are Stable at Room Temperature
C. Würtele, O. Sander, V. Lutz, T. Waitz, F. Tuczek, S. Schindler
J. Am. Chem. Soc. 131 (2009) 7544–7545
- Ordered Mesoporous In_2O_3 : Synthesis by Structure Replication and Application as a Methane Gas Sensor
T. Waitz, T. Wagner, T. Sauerwald, C.-D. Kohl, M. Tiemann
Adv. Funct. Mater. 19 (2009) 653–661
- Gas Sensor Based on Ordered Mesoporous In_2O_3
T. Wagner, T. Sauerwald, C.-D. Kohl, T. Waitz, M. Tiemann
Thin Solid Films 517 (2009) 6170 – 6175
- Time-Resolved Photoluminescence Study of Surface Recombination in ZnO Nanostructures
M. Schwalm, S. Horst, A. Chernikov, W. W. Rühle, S. Lautenschläger, P. J. Klar, B. Meyer, T. Waitz, M. Tiemann, S. Chatterjee
Phys. Status Solidi C 6 (2009) 542 – 545
- New Mesoporous Metal Oxides as Gas Sensors
T. Waitz, T. Wagner, C.-D. Kohl, M. Tiemann
in: A. Gedeon, P. Massiani, F. Babonneau (Eds.), *Zeolites and Related Materials: Trends Targets and Challenges* (ISBN 978-0-444-53296-1), Elsevier, Amsterdam (2008) 401–404 (Series: *Stud. Surf. Sci. Catal.*, Vol 174)
- Synthesis of Mesoporous Metal Oxides by Structure Replication: Strategies of Impregnating Porous Matrices with Metal Salts
J. Roggenbuck, T. Waitz, M. Tiemann
Microporous Mesoporous Mater. 113 (2008) 575–582

- Crystalline ZnO with an Enhanced Surface Area Obtained by Nanocasting
T. Waitz, M. Tiemann, P. J. Klar, J. Sann, J. Stehr, B. K. Meyer
Appl. Phys. Lett. 90 (2007) 123108
- Ordered Mesoporous ZnO for Gas Sensing
T. Wagner, T. Waitz, J. Roggenbuck, M. Fröba, C.-D. Kohl, M. Tiemann
Thin Solid Films 515 (2007) 8360-8363

CHEMIEDIDAKTISCHE JOURNALS

- „Ich rieche was, was du nicht riechst“ - Halbleitende Metalloxide als Gassensoren im Chemieunterricht
T. Waitz, M. Tiemann
Chemie Konkret 16 (2009) 183-186

BERICHTE UND KURZFASSUNGEN

- M. REISER, T. WAITZ
Electrical Muscle Stimulation Of Leg Extensors Does Not Enhance Drop Jump Performance:
Medicine & Science in Sports & Exercise. (2005), 37, 262
- M. TIEMANN, J. ROGGENBUCK, T. WAGNER, T. WAITZ
Geordnete poröse Metalloxide durch Replikation rigider Strukturmatrizes
Z. Anorg. Allg. Chem. (2006), 632, 2079
- J. ROGGENBUCK, T. WAITZ, T. WAGNER, A. LOTZ, M. FRÖBA, M. TIEMANN
Ce LIII-XANES Investigation of Nanoporous CeO₂
HASYLAB-Jahresbericht (2006), HASYLAB/DESY, Hamburg 2007, 461 – 462

POSTERPRÄSENTATIONEN

- J. ROGGENBUCK, T. WAITZ, T. WAGNER, M. TIEMANN
Nanoporöse "Gussformen": Schablonen für neue Materialien
Science Day Universität Gießen, Gießen (Deutschland), 03. Februar 2006
- J. ROGGENBUCK, T. WAITZ, M. TIEMANN
Synthesis Details of Ordered Mesoporous Metal Oxides by the Nanocasting Strategy
18. Deutsche Zeolith-Tagung, Hannover (Deutschland), 01. – 03. März 2006
- J. ROGGENBUCK, T. WAITZ, T. WAGNER, M. TIEMANN
Ordered Mesoporous Metal Oxides by the Nanocasting Strategy
2. Materialforschungstag Mittelhessen, Rauschholzhausen (Deutschland), 30. Juni 2006

- T. WAITZ, M. TIEMANN
Synthesis and Characterisation of Ordered Mesoporous Zinc Oxide
19. Deutsche Zeolith-Tagung, Leipzig (Deutschland), 07. – 09. März 2007

- <http://traisa.he.lo-net2.de/info/webQuestFleder/projekt.html>T. WAITZ, T. Wagner, M. TIEMANN
Mesoporous In_2O_3 : Synthesis by Nanocasting and Application as Gas Sensor
20. Deutsche Zeolith-Tagung, Halle (Deutschland), 05. – 07. März 2008

- T. WAITZ, T. WAGNER, M. TIEMANN
Nanoporous In_2O_3 : Synthesis by Nanocasting and Application as Gas Sensor
4. Materialforschungstag Mittelhessen, Marburg (Deutschland), 20. Juni 2008

- T. WAITZ, T. WAGNER, M. TIEMANN
Nanoporous In_2O_3 : Synthesis by Nanocasting and Application as Gas Sensor
NanoSurface 2008, Gießen (Deutschland), 15. August 2008

- B. BECKER, T. WAGNER, T. WAITZ, M. TIEMANN
Synthesis and Characterisation of Nanoporous SnO_2
NanoSurface 2008, Gießen (Deutschland), 15. August 2008

- M. SCHWALM, S. HORST, A. CHERNIKOV, W. W. RÜHLE, S. CHATTERJEE, S. LAUTENSCHLÄGER, P. J. KLAR, B. K. MEYER, T. WAITZ, M. TIEMANN
Surface-Related Photoluminescence Properties of Mesoporous ZnO
21. Deutsche Zeolith-Tagung, Kiel (Deutschland), 04. – 06. März 2009

- T. WAITZ, T. WAGNER, M. TIEMANN
Ordered Mesoporous In_2O_3 : Synthesis by Structure Replication, Characterization, and Gas-Sensing Properties
21. Deutsche Zeolith-Tagung, Kiel (Deutschland), 04. – 06. März 2009

- B. BECKER, T. WAITZ, T. WAGNER, T. SAUERWALD, C.-D. KOHL, M. TIEMANN
Ordered Mesoporous SnO_2 for Gas Sensor Application: A Study on Thermal Stability
21. Deutsche Zeolith-Tagung, Kiel (Deutschland), 04. – 06. März 2009

- T. WAITZ, T. WAGNER, M. TIEMANN
Synthesis of Ordered Mesoporous In_2O_3 by Structure Replication
NanoSurface 2009, Gießen (Deutschland), 10. Juli 2009

Danksagung

An dieser Stelle möchte ich mich ganz herzlich bei all jenen Menschen bedanken, die mich bei der Anfertigung dieser Arbeit in vielfältiger Weise unterstützt haben.

Mein größter Dank gilt Prof. Dr. Michael Tiemann für die Überlassung des Themas, die Freiheiten bei der Bearbeitung, die stete Diskussionsbereitschaft und Offenheit, sowie die exzellente Atmosphäre in der kleinen aber feinen Arbeitsgruppe (in der Weihnachten auch mal im Mai stattfinden kann).

Bei Herrn Prof. Dr. Fröba möchte ich mich ganz herzlich für die Aufnahme in seinen Gießener Arbeitskreis bedanken.

Thorsten Wagner danke ich für sein hohes Engagement, mir die Physik näher zu bringen, für das sorgfältige Korrekturlesen meiner Arbeit und seine außergewöhnliche Diskussionsbereitschaft. (Das ist ganz lustig weil,...!?! *Aha*. Wir haben da einen ganz lustigen Effekt gefunden...!)

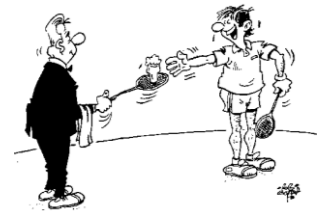
Bei Jan Roggenbuck möchte ich mich ganz herzlich für ein spitzen Arbeitsklima im Bühhroooo und im Labor bedanken. Vielen Dank auch für die Geduld und dein Verständnis, dass du meinem zweijährigen Referendariatsstress entgegengebracht hast.

Bei Günther Koch und Christoph Weidmann möchte ich mich für ihre Mühen und ihre Geduld bei den elektronenmikroskopischen Aufnahmen meiner Proben bedanken. (Ich bin mir jetzt ganz sicher, dass ich keine Proben mehr zum Messen habe!)

Stefanie Haffer möchte ich ganz herzlich für ihre Unterstützung beim Partikelzählen bedanken. (Ohne deine Hilfe würde die Arbeit sicher ganz anders aussehen ☺)

Des Weiteren bedanke ich mich bei:

Dem Badminton-Team für die sportlichen Mittwochabende.



Dem ehemaligen Gießener Arbeitskreis für die freundliche Aufnahme: Dr. Felix Brieler, Dr. Maximilian Cornelius, Petra Grundmann, Dr. Frank Hoffmann, Michaela Jakubowski, Dr. Jürgen Morell, Dr. Vivian Rebbin, Dr. Michael Serafin, Katharina Sukkau, Stephanie Wenzel, Hubert Wörner, Marie-Luise Wolff, Dr. Wolfgang Herrendorf und Sven Kroker.

Till von Graberg, Rainer Ostermann, Simone Mascotto, Silke Rahn, Claas Wessel, Laem, Takeshi, Dödel, Jochen Reinacher, Christian Reitz für kurzweilige Grillabende und spontane Küchenmeetings.

Der Schulleitung des Landgraf-Ludwigs-Gymnasiums für die Möglichkeit und Unterstützung, diese Arbeit neben meinem Referendariat anfertigen zu können. (Liebe Antje, lieber Klaus: Vielen Dank!).

Dem Trainerteam der LG-Wettenberg für die Vertretungsstunden.

Stefanie Haffer, Dr. Christian Würtele, Andreas Lotz, Benjamin Becker und Christoph Weidmann für die Teilnahme an der Kalibrierung der Kryostaten.

Steffie für ihre Geduld mit mir während dieser Arbeit und der nicht immer einfachen Zeit des Referendariats. Vielen Dank für deine aufbauenden Worte, deine moralische Unterstützung und vielem mehr.